The Astronomical Journal, 159:268 (39pp), 2020 June https://doi.org/10.3847/1538-3881/ab8adf
© 2020. The American Astronomical Society. All rights reserved.

Bayesian Approach for Determining Microlens System Properties with High-angular-resolution Follow-up Imaging

Naoki Koshimoto[1,2,3], David P. Bennett[2,3], and Daisuke Suzuki[4]
[1] Department of Astronomy, Graduate School of Science, The University of Tokyo, 7-3-1 Hongo, Bunkyo-ku, Tokyo 113-0033, Japan
[2] Laboratory for Exoplanets and Stellar Astrophysics, NASA/Goddard Space Flight Center, Greenbelt, MD 20771, USA
[3] Department of Astronomy, University of Maryland, College Park, MD 20742, USA
[4] Institute of Space and Astronautical Science, Japan Aerospace Exploration Agency, 3-1-1 Yoshinodai, Chuo, Sagamihara, Kanagawa, 252-5210, Japan
Received 2019 October 24; revised 2020 April 14; accepted 2020 April 16; published 2020 May 21

Abstract

We present the details of the Bayesian analysis of the planetary microlensing event MOA-2016-BLG-227, whose excess flux is likely due to a source/lens companion or an unrelated ambient star, as well as of the assumed prior distributions. Furthermore, we apply this method to four reported planetary events, MOA-2008-BLG-310, MOA-2011-BLG-293, OGLE-2012-BLG-0527, and OGLE-2012-BLG-0950, where adaptive optics observations have detected excess flux at the source star positions. For events with small angular Einstein radii, our lens mass estimates are more uncertain than those of previous analyses, which assumed that the excess was due to the lens. Our predictions for MOA-2008-BLG-310 and OGLE-2012-BLG-0950 are consistent with recent results on these events obtained via Keck and Hubble Space Telescope observations when the source star is resolvable from the lens star. For events with small angular Einstein radii, we find that it is generally difficult to conclude whether the excess flux comes from the host star. Therefore, it is necessary to identify the lens star by measuring its proper motion relative to the source star to determine whether the excess flux comes from the lens star. Even without such measurements, our method can be used to statistically test the dependence of the planet-hosting probability on the stellar mass.

Unified Astronomy Thesaurus concepts: Gravitational microlensing exoplanet detection (2147); Exoplanet detection methods (489); Gravitational microlensing (672); High-resolution microlensing event imaging (2138)

1. Introduction

Gravitational microlensing, which has gained a unique niche in the study of extrasolar planetary systems, enables us to statistically investigate planetary systems down to sub-Earth masses (Bennett & Rhie 1996) beyond the snow line (Suzuki et al. 2016) as a function of the galactocentric distance. It is also sensitive to unbound planets that have been ejected from the systems of their formation (Bennett et al. 1997; Sumi et al. 2011; Mróz et al. 2017). A major challenge for the microlensing method is the determination of the lens and planetary host star mass, M_L. One microlensing light-curve parameter that is directly related to the host star mass is the Einstein-radius-crossing time $t_{\rm E} = \theta_{\rm E}/\mu_{\rm rel}$, where $\theta_{\rm E}$ is the angular Einstein radius and $\mu_{\rm rel}$ is the relative lens–source proper motion. The angular Einstein radius is given by $\theta_{\rm E} = \sqrt{(4GM_L/c^2)(D_S - D_L)/(D_S D_L)}$, where D_L and D_S are the distances to the lens and source, respectively. The quantities $t_{\rm E}$ and $\mu_{\rm rel}$ are commonly measured in an inertial reference frame that moves with Earth near the time of peak magnification of the event. Because $t_{\rm E}$ depends on the lens mass and distance, as well as on the lens–source relative proper motion $\mu_{\rm rel}$, the measurement of $t_{\rm E}$ does not yield the lens mass measurement. However, the planet-to-star mass ratio is usually well determined from the microlensing light curve (Gaudi 2012); hence, the planet masses are generally known when the host star mass can be measured.

There are three methods for relating the lens mass M_L and distance D_L. When the microlensing light curve has sharp features, as is the case for most planetary events and many stellar binary events, the source-radius-crossing time, t_*, can be measured. Because the angular source star radius, θ_*, can generally be determined from the dereddened magnitude and color of the source (Kervella et al. 2004; Boyajian et al. 2014; Adams et al. 2018), the measurement of t_* generally allows the determination of the angular Einstein radius, $\theta_{\rm E} = \theta_* t_{\rm E}/t_*$, and the lens–source relative proper motion, $\mu_{\rm rel} = \theta_*/t_*$. Alternatively, the lens–source relative proper motion can also be measured directly from high-angular-resolution follow-up observations (Bennett et al. 2006, 2015; Batista et al. 2015). These follow-up observations can also be used to determine $\theta_{\rm E} = \mu_{\rm rel} t_{\rm E}$, although it is important to ensure that $\mu_{\rm rel}$ and $t_{\rm E}$ are measured in the same coordinate system. Direct measurements of the relative proper motion, $\mu_{\rm rel}$, are generally performed in a nearly heliocentric coordinate system, while $t_{\rm E}$ is usually measured in an inertial "geocentric" coordinate system that moves with Earth near the time of peak magnification. In any case, once $\theta_{\rm E}$ is measured, we have the following mass–distance relation:

$$M_L = \frac{c^2}{4G}\theta_{\rm E}^2 \frac{D_S D_L}{D_S - D_L}. \quad (1)$$

Another light-curve parameter that can provide the mass–distance relation is the microlensing parallax (Gould 1992; Alcock et al. 1995), which can be parameterized by the Einstein radius projected from the source to the position of the observer, $\tilde{r}_{\rm E}$. However, it is usually parameterized by the microlensing parallax parameter, $\pi_{\rm E} = {\rm au}/\tilde{r}_{\rm E}$. Actually, $\pi_{\rm E}$ is a two-dimensional vector, $\boldsymbol{\pi}_{\rm E}$, in the same direction as the lens–source relative motion; however, only the length of this vector

appears in the mass–distance relation:

$$M_L = \frac{c^2}{4G}\left(\frac{\mathrm{au}}{\pi_\mathrm{E}}\right)^2 \frac{D_S - D_L}{D_S D_L}. \quad (2)$$

When θ_E and π_E are both measured, we can directly determine the lens mass (An et al. 2002; Gould et al. 2004; Muraki et al. 2011) by multiplying Equation (1) by Equation (2) and taking the square root to obtain

$$M_L = \frac{\theta_\mathrm{E} c^2 \mathrm{au}}{4G\pi_\mathrm{E}} = \frac{\theta_\mathrm{E}\, M_\odot}{(8.1439\ \mathrm{mas})\pi_\mathrm{E}}. \quad (3)$$

The third method for relating the mass and distance is to detect and measure the lens star flux, F_L. This requires the use of a mass–luminosity relation, $\mathcal{M}(M_L)$, where $\mathcal{M}$ is the absolute magnitude in the passband in which the lens star flux is measured (Delfosse et al. 2000). The measured lens flux corrected for extinction is $\propto 10^{-0.4\mathcal{M}(M_L)}/D_L^2$. Owing to the extreme crowding in the galactic bulge fields where microlensing events are observed, the detection of the lens flux requires high-angular-resolution imaging that can be realized with adaptive optics (AO) systems or the Hubble Space Telescope (HST). Measurement of the lens flux provides two additional methods for determining the lens mass and distance. The first method is by measurement of the lens flux and θ_E (Bennett et al. 2006, 2015; Batista et al. 2015). The second method is by measurement of the microlensing parallax and lens flux (Kubas et al. 2012; Koshimoto et al. 2017b; Beaulieu et al. 2018). The lens flux plus θ_E method is expected to be the primary exoplanet system mass measurement method for the WFIRST mission (Bennett & Rhie 2002; Bennett et al. 2007; Spergel et al. 2015).

There are two approaches for measuring the lens flux. Both require high-angular-resolution follow-up observations by large ground-based telescopes with AO systems or by the HST. First, even before the lens and source have a sufficiently large separation to be measured separately, it is possible to obtain the excess flux at the position of the event because the source flux is readily determined through light-curve modeling. If we can confirm that the excess flux comes from the lens, then we can use the excess flux as the lens flux, which yields a mass–distance relation. However, stars other than the lens star, such as an unrelated star or a companion to the source or lens, may contribute to or even dominate this excess flux. This possibility has been considered in some previous analyses (Janczak et al. 2010; Batista et al. 2014; Fukui et al. 2015; Koshimoto et al. 2017b) of planetary microlensing events; however, these studies have not always included a consistent treatment of prior and posterior constraints. In this paper, we present a new systematic Bayesian approach for determining lens star masses and distances from measurements of the excess flux at the location of the source stars. This new method was used and briefly explained in the analysis of the MOA-2016-BLG-227 microlensing event (Koshimoto et al. 2017a). Here, we present the details of this method and apply it to some previously reported events in which excess flux was detected at the position of the source: MOA-2008-BLG-310 (M08310, Janczak et al. 2010), MOA-2011-BLG-293 (M11293, Yee et al. 2012; Batista et al. 2014), OGLE-2012-BLG-0563 (O120563, Fukui et al. 2015), OGLE-2012-BLG-0950 (O120950, Koshimoto et al. 2017b), and MOA-2016-BLG-227 (M16227, Koshimoto et al. 2017a). Although the calculation results for M16227 have already been presented previously by Koshimoto et al. (2017a), we provide further details in this paper.

Second, if sufficient time has elapsed since the microlensing event such that the lens and source have a sufficiently large separation to be resolved, then it is possible to directly measure the lens flux unless the lens is too faint. In this case, the observable quantity is not only the flux, but also the separation between the source and a lens candidate; hence, we can confirm our prediction of the possible origin of the excess by comparing the measured separation and the lens–source relative proper motion obtained through light-curve fitting. If the two values are consistent with each other, then the candidate is probably the lens or a lens companion; otherwise, the candidate is a source companion or an unrelated ambient star. With this approach, the lens star is shown to be too faint to produce excess flux at the source position (Bhattacharya et al. 2017), or the lens–source separation can be measured by resolving the lens and source (Batista et al. 2015; Vandorou et al. 2019), measuring the elongation of the blended lens–source image (Bennett et al. 2007, 2015, 2020; Bhattacharya et al. 2018), or measuring the color-dependent centroid shift of the blended image (Bennett et al. 2006). In fact, our predictions of the possible origins of the excess fluxes for M08310 and O120950 provided in this paper are consistent with those revealed by recent follow-up observations after sufficient time had elapsed for those events (Bhattacharya et al. 2017, 2018).

The main aim of this paper is to provide a Bayesian approach for determining microlensing system properties that consistently treat the prior and posterior probabilities, which were not properly treated in previous studies, when excess flux at the position of a microlensing event is measured (the first approach above). Although we explain the details of our prior choices, they are shown as an example, and some are optimized for the events to which we apply the method; hence, one can apply their own choices depending on the character of the event, purpose, preferences, or knowledge.

The remainder of this paper is organized as follows. Section 2 discusses some problems in previous analyses of the potential "contamination" of the flux attributed to the lens star by other stars. Section 3 presents the concept of our new Bayesian approach and outline of calculations, while Section 4 presents our detailed assumptions and models used to calculate the prior probability density functions (PDFs). Section 5 describes the application of this method to previously reported events and presents the results. Section 6 discusses the interpretation of the results. Section 7 shows how the detectability of the lens flux can be predicted when planning high-angular-resolution follow-up observations. Section 8 describes the dependence of our results on the unknown planet-hosting probability, while Section 9 describes the dependence on other priors. Section 10 tests the binary distribution used in this study by comparing the number of detectable companions predicted by the model and the actual number of detected companions. Section 11 discusses the overall findings of this study. Finally, Section 12 gives a summary.

2. Previous Prior Probability Calculations

Several previous studies have considered the probability of the observations of excess flux being "contaminated" by excess flux due to a star or stars other than the lens star

(Janczak et al. 2010; Batista et al. 2014; Fukui et al. 2015; Koshimoto et al. 2017b). These studies considered four possible origins of the excess flux: the lens star, unrelated ambient stars, and companions to the source and lens stars. They calculated the "prior" probability that each of the three alternatives other than the lens has a brightness in a certain range including the observed excess flux. This range was taken to be the range of the measurement uncertainty in some cases, while it was larger in other cases. Then, the sum of these three excess flux "contamination" probabilities was subtracted from 1, and the resulting value was treated as the probability that all of the observed excess flux originates from the lens. In most of these cases, the resulting value was relatively large, and it was claimed that the excess flux likely originated from the lens star.

The justification often given for this type of calculation is that we know that the lens star exists, while stellar companions to the source and lens or ambient stars unresolved from the source may not exist. However, there is no reason to assume that the lens star is likely to be sufficiently bright to be detected, and for some events, such as those with small $\theta_{\rm E}$ values, it is reasonable to expect that the lens star is too faint to be detected. This is because $\theta_{\rm E} \propto \sqrt{M_L \pi_{\rm rel}}$, where $\pi_{\rm rel} \equiv {\rm au}\,(1/D_L - 1/D_S)$, and a small $\theta_{\rm E}$ indicate a small mass and/or distant star, such as an M dwarf in the Galactic bulge, which is the most common in our Galaxy and too faint to be detected at the position of a much brighter source star. Moreover, the choice of a particular flux range that is selected to include the measured excess flux value is not a prior choice, as it depends on the measured excess flux. The contamination probability determined in this manner also depends on the somewhat arbitrary flux range that is considered. If this range is taken to be the measurement uncertainty, then the difficulty becomes clearer. If the measurement uncertainty is small, then the contamination probability tends to zero. However, this is just a reflection of the fact that the probability of any particular value included in the small uncertainty of a precise measurement is small. With consistent comparison of a priori and a posteriori probabilities, the improbability of a particular precise measurement would affect the probabilities of the different excess flux sources in a similar manner. A correct Bayesian analysis needs to include the a priori probabilities for the detectable flux from the lens star, an unrelated blended star, and companions to the lens and source stars, and then apply the excess flux measurement constraint to the combined probability distribution. The previous analyses were flawed because they applied a version of the measurement constraints to only the "contamination" priors while ignoring the possibly small prior probability that the lens star is detectable.

3. Method

We must consider all possible contributions to the excess flux in our analysis. Accordingly, we consider four different contributions, F_i, to the excess flux: flux from the lens star, F_L; flux from blended ambient star(s), $F_{\rm amb}$; flux from a companion to the source, $F_{\rm SC}$; and flux from a companion to the lens, $F_{\rm LC}$. Thus, the index i takes four values: L, amb, SC, and LC. With this notation, the joint posterior PDF for the excess flux is given by

$$\begin{aligned} &f_{\rm post}\,(F_L, F_{\rm amb}, F_{\rm SC}, F_{\rm LC}|F_{\rm excess} = F_{\rm ex,obs}) \\ &\propto \mathcal{L}(F_{\rm excess} = F_{\rm ex,obs}|F_L, F_{\rm amb}, F_{\rm SC}, F_{\rm LC}) \\ &\quad \times f_{\rm pri}\,(F_L, F_{\rm amb}, F_{\rm SC}, F_{\rm LC}), \end{aligned} \tag{4}$$

where $f_{\rm pri}\,(F_L, F_{\rm amb}, F_{\rm SC}, F_{\rm LC})$ is the joint prior PDF of F_L, $F_{\rm amb}$, $F_{\rm SC}$, and $F_{\rm LC}$, and

$$F_{\rm excess} \equiv F_L + F_{\rm amb} + F_{\rm SC} + F_{\rm LC}. \tag{5}$$

$\mathcal{L}(F_{\rm excess} = F_{\rm ex,obs}|F_L, F_{\rm amb}, F_{\rm SC}, F_{\rm LC})$ is the likelihood of the observed excess flux $F_{\rm ex,obs}$. We use the Gaussian distribution with the measured $F_{\rm ex,obs}$ value and its error in flux units. The observed excess flux is obtained through subtraction,

$$F_{\rm ex,obs} = F_{\rm tar,obs} - F_{S,\rm obs}, \tag{6}$$

where $F_{\rm tar,obs}$ is the target flux measured in AO or HST imaging, and $F_{S,\rm obs}$ is the source flux in the same bandpass as the one that conducted the imaging. $F_{S,\rm obs}$ is measured from light-curve fitting if there is light-curve data in the corresponding bandpass; otherwise, it is converted from the source flux in a different bandpass using a color–color relation. In this study, we apply our method to five events with H-band AO imaging observations conducted in previous studies; hence, all the fluxes above are defined as the brightness in the H band. We use $H_{\rm amb}$, H_L, $H_{\rm SC}$, $H_{\rm LC}$, $H_{\rm excess}$, and $H_{\rm ex,obs}$ to denote the H-band magnitudes corresponding to fluxes $F_{\rm amb}$, F_L, $F_{\rm SC}$, $F_{\rm LC}$, $F_{\rm excess}$, and $F_{\rm ex,obs}$, respectively.

We note that excess flux can also be measured in any optical band with which the survey observations are conducted, usually in the I band or V band, and we call this blending flux to distinguish it from the excess flux obtained through high-angular-resolution imaging. We do not use blending flux in our calculation because of the following two reasons. First, blending flux usually gives information that is irrelevant to the excess in the AO image because the angular resolution of the survey observations is 5–10 times worse than that of AO imaging. This makes the expected number of ambient stars contained in blending flux 25–100 times larger than that in excess flux. Given the extreme crowding of the included bulge field, blending flux is very likely to be contaminated by ambient stars that are not included in the excess flux. A more serious problem with blending flux is that it could be underestimated. Sky brightness in the bulge field is usually overestimated in a seeing-limited image because a lot of unresolved stars contribute to it, which leads to underestimation of the blending flux. In fact, Vandorou et al. (2019) found that the lens flux measured by AO imaging for MOA-2013-BLG-220 was brighter than the upper limit based on the blending flux constrained by Yee et al. (2014).

3.1. Outline of Calculations

We use a Monte Carlo method to calculate the joint prior and joint posterior PDFs. Figure 1 shows a flowchart of our procedure to calculate the two joint PDFs. Table 1 shows the PDFs and parameters that are modeled in the Monte Carlo simulation, while Tables 2 and 3 summarize all the models and inputs that are needed to calculate those parameters, respectively. In this section, we outline our calculation process to give perspective, where all input parameters in Table 3 are

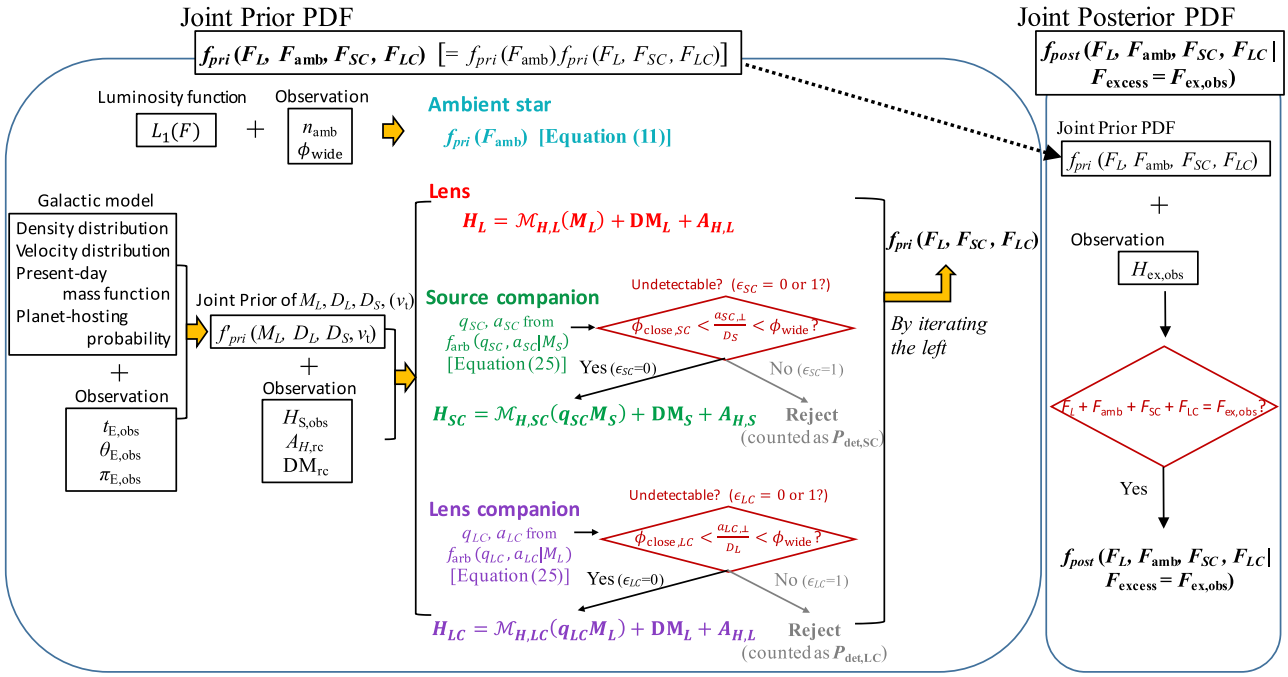

Figure 1. Flowchart of our calculation method. We determine the joint prior PDF through a Monte Carlo method using the calculations outlined in the left panel, which determine $f_{pri}(F_L, F_{amb}, F_{SC}, F_{LC})$. Source and lens companions that are not compatible with the prior separation constraints are rejected and excluded from consideration. Then, the calculation of the joint posterior PDF, $f_{post}(F_L, F_{amb}, F_{SC}, F_{LC}|F_{excess} = F_{ex,obs})$, is performed as shown in the right panel, rejecting all combinations that do not match the measured brightness.

introduced. Section 4 describes the details of the assumptions and parameters in the calculation explained here.

3.1.1. Calculation of the Prior PDF

In our analysis, we define prior probabilities as those that do not depend on the measurement of the target flux in the AO image to be the observed value $F_{tar,obs}$. Thus, we use any other available information about the target we are analyzing to calculate the prior probability, such as the microlensing light-curve parameters and the FWHM value of the AO image for measuring the target flux.

In every trial of the Monte Carlo simulation, we simulate each of the four objects using the models given in Table 2 under the constraints from the input parameters given in Table 3. The left box in Figure 1 shows this procedure. We calculate the joint prior PDF $f_{pri}(F_L, F_{amb}, F_{SC}, F_{LC})$ by repeating the trials many times. Below we briefly summarize the calculation of each of the four brightnesses in each trial.

Ambient star flux—We simulate the ambient star flux by combining the luminosity function (LF) for a field star and the distribution of the number of field stars within the resolution element of the AO image where each excess flux was measured. For the LF of a field star $L_1(F)$, we use the H-band LF from the HST observations of the Galactic bulge by Zoccali et al. (2003).

The number of field stars within the size of the resolution element of the AO image follows the Poisson distribution with the mean of λ_{amb}. We need the number density of ambient stars in the target field n_{amb}, and we characterize the resolution element by the radius of a circle where a star within it cannot be resolved from the target ϕ_{wide} to calculate the mean $\lambda_{amb} = n_{amb}\pi\phi_{wide}^2$. We derive n_{amb} for each field by counting the field stars in the AO images or counting the red clump stars in the OGLE-III catalog (Szymański et al. 2011) in Section 4.1.1, and we use the radius ϕ_{wide} used by the previous studies. Section 4.1 describes the details of the ambient star flux prior.

Lens flux—The prior lens flux distribution depends on three microlensing parameters observed: the Einstein-radius-crossing time, $t_{E,obs}$; the angular Einstein radius, $\theta_{E,obs}$; and the microlens parallax, $\pi_{E,obs}$. Combining the Galactic model with those constraints, we derive the joint prior PDF of the lens mass M_L, lens distance D_L, source distance D_S, and transverse velocity v_t, $f_{pri}(M_L, D_L, D_S, v_t|t_E = t_{E,obs}, \theta_E = \theta_{E,obs}, \pi_E = \pi_{E,obs})$, with which we can simulate M_L, D_L, and D_S in every trial of the Monte Carlo simulation. Section 4.2 describes the details.

Given the lens mass and distance from $f_{pri}(M_L, D_L, D_S, v_t|t_E = t_{E,obs}, \theta_E = \theta_{E,obs}, \pi_E = \pi_{E,obs})$, we can calculate the lens magnitude H_L using both the mass–luminosity relation that is described in Section 4.3 and the extinction for the lens system $A_{H,L}$ that is described in Section 4.5. The calculation of $A_{H,L}$ requires two input parameters for each target field: the mean extinction value for the red clump in the vicinity of the target, $A_{H,rc}$, and the mean distance modulus to these bulge red clump stars in this field, DM_{rc}. $A_{H,rc}$ is taken from the previous published paper for each event while DM_{rc} is from the value at the nearest grid point to each event from Table 3 of Nataf et al. (2013).

Table 1
Probability Density Functions and Parameters that are Modeled in Our Calculation

	Notation	Note
Modeled PDFs		
Joint posterior PDF of F_L, $F_{\rm amb}$, $F_{\rm SC}$, $F_{\rm LC}$	$f_{\rm post}(F_L, F_{\rm amb}, F_{\rm SC}, F_{\rm LC}\vert F_{\rm excess} = F_{\rm ex,obs})$	Equation (4), modeled by iteration of the right box in Figure 1
Joint prior PDF of F_L, $F_{\rm amb}$, $F_{\rm SC}$, $F_{\rm LC}$	$f_{\rm pri}(F_L, F_{\rm amb}, F_{\rm SC}, F_{\rm LC})$	$=f_{\rm pri}(F_L, F_{\rm SC}, F_{\rm LC})f_{\rm pri}(F_{\rm amb})$
Prior PDF of $F_{\rm amb}$	$f_{\rm pri}(F_{\rm amb})$	Equation (11)
Joint prior PDF of F_L, $F_{\rm SC}$, $F_{\rm LC}$	$f_{\rm pri}(F_L, F_{\rm SC}, F_{\rm LC})$	Modeled by iteration of the left box in Figure 1
Modeled parameters		
Brightness		
Flux (mag) of the lens in the H band	F_L, H_L	$H_L = \mathcal{M}_{H,L}(M_L) + 5\log\frac{D_L}{10\ {\rm pc}} + A_{H,L}$
Flux (mag) of ambient stars in the H band	$F_{\rm amb}$, $H_{\rm amb}$	Follows Equation (11)
Flux (mag) of a source companion in the H band	$F_{\rm SC}$, $H_{\rm SC}$	$H_{\rm SC} = \mathcal{M}_{H,{\rm SC}}(q_{\rm SC}M_S) + 5\log\frac{D_S}{10\ {\rm pc}} + A_{H,S}$
Flux (mag) of a lens companion in the H band	$F_{\rm LC}$, $H_{\rm LC}$	$H_{\rm LC} = \mathcal{M}_{H,{\rm LC}}(q_{\rm LC}M_L) + 5\log\frac{D_L}{10\ {\rm pc}} + A_{H,L}$
Excess flux (mag) in the H band	$F_{\rm excess}$, $H_{\rm excess}$	$F_{\rm excess} \equiv F_L + F_{\rm amb} + F_{\rm SC} + F_{\rm LC}$
Fraction of each flux to the excess	$f_L, f_{\rm amb}, f_{\rm SC}, f_{\rm LC}$	$f_i \equiv F_i/F_{\rm excess}$ $(i = L, {\rm amb}, {\rm SC}, {\rm LC})$
For $F_{\rm L}$, $F_{\rm LC}$		
Lens mass	M_L	Follows $f'_{\rm pri}(M_L, D_L, D_S, v_{\rm t})$[a] in the prior
Lens distance	D_L	Follows $f'_{\rm pri}(M_L, D_L, D_S, v_{\rm t})$[a] in the prior
Mass ratio of a lens companion	$q_{\rm LC}$	Follows $f_{\rm arb}(q_{\rm LC}, a_{\rm LC}\vert M_L)$ combined with $\epsilon_{\rm LC}$[b] in the prior
Semimajor axis of a lens companion	$a_{\rm LC}$	Follows $f_{\rm arb}(q_{\rm LC}, a_{\rm LC}\vert M_L)$ combined with $\epsilon_{\rm LC}$[b] in the prior
Extinction for the lens system	$A_{H,L}$	$A_{H,L} = A_{H,{\rm rc}}\frac{1-\exp[-D_L/(0.1\ {\rm kpc}/\sin\vert b\vert)]}{1-\exp[-D_{\rm rc}/(0.1\ {\rm kpc}/\sin\vert b\vert)]}$
For $F_{\rm SC}$		
Source mass	M_S	$M_S = M_S(\mathcal{M}_{H,S})$, where $\mathcal{M}_{H,S} = H_{S,{\rm obs}} - A_{H,S} - 5\log\frac{D_S}{10\ {\rm pc}}$
Source distance	D_S	Follows $f'_{\rm pri}(M_L, D_L, D_S, v_{\rm t})$[a] in the prior
Mass ratio of a source companion	$q_{\rm SC}$	Follows $f_{\rm arb}(q_{\rm SC}, a_{\rm SC}\vert M_S)$ combined with $\epsilon_{\rm SC}$[b] in the prior
Semimajor axis of a source companion	$a_{\rm SC}$	Follows $f_{\rm arb}(q_{\rm SC}, a_{\rm SC}\vert M_S)$ combined with $\epsilon_{\rm SC}$[b] in the prior
Extinction for the source system	$A_{H,S}$	$A_{H,S} = A_{H,{\rm rc}}\frac{1-\exp[-D_S/(0.1\ {\rm kpc}/\sin\vert b\vert)]}{1-\exp[-D_{\rm rc}/(0.1\ {\rm kpc}/\sin\vert b\vert)]}$
To be compared in Section 10		
Fraction of detectable source companions	$P_{{\rm det},SC}$	Fraction of SC that gives $\epsilon_{\rm SC} = 1$ (Figure 1)
Fraction of detectable close source companions	$P_{{\rm det},{\rm SC}_{\rm close}}$	Fraction of SC that gives $\epsilon_{\rm SC} = 1$ because $\frac{a_{{\rm SC},\perp}}{D_S} < \phi_{\rm close,SC}$
Fraction of detectable wide source companions	$P_{{\rm det},{\rm SC}_{\rm wide}}$	Fraction of SC that gives $\epsilon_{\rm SC} = 1$ because $\frac{a_{{\rm SC},\perp}}{D_S} > \phi_{\rm wide}$
Fraction of detectable lens companions	$P_{\rm det,LC}$	Fraction of LC that gives $\epsilon_{\rm LC} = 1$ (Figure 1)
Fraction of detectable close lens companions	$P_{{\rm det},{\rm LC}_{\rm close}}$	Fraction of LC that gives $\epsilon_{\rm LC} = 1$ because $\frac{a_{{\rm LC},\perp}}{D_L} < \phi_{\rm close,LC}$[c]
Fraction of detectable wide lens companions	$P_{{\rm det},{\rm LC}_{\rm wide}}$	Fraction of LC that gives $\epsilon_{\rm LC} = 1$ because $\frac{a_{{\rm LC},\perp}}{D_L} > \phi_{\rm wide}$

Notes.
[a] Abbreviation of $f_{\rm pri}(M_L, D_L, D_S, v_t\vert t_{\rm E} = t_{\rm E,obs}, \theta_{\rm E} = \theta_{\rm E,obs}, \pi_{\rm E} = \pi_{\rm E,obs})$.
[b] Binary distribution combined with the detection efficiency is referred to as the undetected binary distribution.
[c] This is reassessed in Section 10.3.1.

Table 2
The Models Needed to Calculate the Prior PDF and Our Choices for Them

Model	Notation	To Model	Our Choice	Section
For $F_{\rm amb}$				
Luminosity function (LF)	$L_{\rm l}(F)$	$f_{\rm pri}(F_{\rm amb})$	LF by Zoccali et al. (2003)	Section 4.1.2
Detection efficiency for ambient stars	$\epsilon_{\rm amb}$	$f_{\rm pri}(F_{\rm amb})$	$\Theta(\phi - \phi_{\rm wide})$ [a]	Section 4.1.2
For F_L, $F_{\rm SC}$, $F_{\rm LC}$				
Prior PDF of M_L, D_L, D_S and $v_{\rm t}$	$f'_{\rm pri}(M_L, D_L, D_S, v_{\rm t})$ [b]	M_L, D_L, D_S	Galactic model [c] $\times$ $\mathcal{L}(t_{\rm E,obs}, \theta_{\rm E,obs}, \pi_{\rm E,obs})$ [d]	Sections 4.2, 4.2.1
Density distribution	ρ_B, ρ_D	$f'_{\rm pri}(M_L, D_L, D_S, v_{\rm t})$ [b]	Equations (12)–(13)	Section 4.2.1
Velocity distribution	⋯	$f'_{\rm pri}(M_L, D_L, D_S, v_{\rm t})$ [b]	S11 model in Koshimoto & Bennett (2019)	Section 4.2.1
Present-day mass function	$\Phi_{\rm PD}(M)$	$f'_{\rm pri}(M_L, D_L, D_S, v_{\rm t})$ [b]	IMF + age and metallicity distributions	Section 4.2.1
Initial mass function (IMF)	$\Phi_{\rm IMF}(M)$	$\Phi_{\rm PD}(M)$	Equation (14)	Section 4.2.1
Age distribution	⋯	$\Phi_{\rm PD}(M)$, $\mathcal{M}_H(M)$, $M(\mathcal{M}_H)$	Bulge: $\mathcal{N}$(9 Gyr, 1 Gyr) [e], disk: $\mathcal{N}$(5 Gyr, 2 Gyr) [e]	Section 4.2.1
Metallicity distribution	⋯	$\Phi_{\rm PD}(M)$, $\mathcal{M}_H(M)$, $M(\mathcal{M}_H)$	Solar metallicity	Section 4.2.1
Planet -hosting probability	$P_{\rm host}$	$f'_{\rm pri}(M_L, D_L, D_S, v_{\rm t})$ [b]	$P_{\rm host} \propto M_h^{\alpha}$ $w/\alpha = 0, \pm 1$, $P_{\rm host} = 0$ for remnant	Sections 4.2, 8
Mass–luminosity relation	$\mathcal{M}_H(M)$, $M(\mathcal{M}_H)$	H_L, $H_{\rm LC}$, $H_{\rm SC}$, M_S	Empirical (0.1–0.8 $M_\odot$), isochrones (otherwise)	Section 4.3
Extinction distribution along the line of sight	⋯	$A_{H,S}$, $A_{H,L}$	$A_H \propto 1 - \exp\left[-\frac{D}{0.1\ \mathrm{kpc}\ /\ \sin\lvert b\rvert}\right]$	Section 4.5
For $F_{\rm SC}$, $F_{\rm LC}$				
Binary distribution for an arbitrary star	$f_{\rm arb}(q, a\lvert M)$	$q_{\rm SC}$, $a_{\rm SC}$, $q_{\rm LC}$, $a_{\rm LC}$	Equation (25)	Section 4.4.1
Binary distribution for a non-secondary star	$\mathcal{F}_{\rm mult}(M)$, $f_{\rm prim}(q, a\lvert M)$	$f_{\rm arb}(q, a\lvert M)$	$f_{\rm prim}(q, a\lvert M) \propto q^{\gamma}\ \Lambda(a; \eta_{\log a}, \sigma^2_{\log a})$ [f]	Section 4.4.2
Multiplicity fraction	$\mathcal{F}_{\rm mult}(M)$	$f_{\rm arb}(q, a\lvert M)$	$\mathcal{F}_{\rm mult} = 0.196 + 0.255\ M$	Section 4.4.2
Slope of mass-ratio function	γ	$f_{\rm prim}(q, a\lvert M)$	γ_c ($\log[a/\mathrm{au}] < \eta_{\log a}$), γ_w ($\log[a/\mathrm{au}] > \eta_{\log a}$)	Section 4.4.2
γ for close binary	γ_c	$f_{\rm prim}(q, a\lvert M)$	$\gamma_c = 1.2$–$2.8\ \log M$	Section 4.4.2
γ for wide binary	γ_w	$f_{\rm prim}(q, a\lvert M)$	$\gamma_w = 0$ ($M \geqslant 0.34$), $\gamma_w = -3.1$–$6.7\ \log M$ ($M < 0.34$)	Section 4.4.2
Mean of $\log[a/\mathrm{au}]$ distribution	$\eta_{\log a}$	$f_{\rm prim}(q, a\lvert M)$	$\eta_{\log a} = 0.57 + 1.02\ M$	Section 4.4.2
Standard deviation of $\log[a/\mathrm{au}]$ distribution	$\sigma_{\log a}$	$f_{\rm prim}(q, a\lvert M)$	$\sigma_{\log a} = 1.6 + 1.2\ M$	Section 4.4.2
Detection efficiency for a source companion	$\epsilon_{\rm SC}$	$q_{\rm SC}$, $a_{\rm SC}$	$\Theta[(\phi - \phi_{\rm wide})(\phi - \phi_{\rm close,SC})]$ [a]	Section 4.4.4
Close limit of undetectable source companion	$\phi_{\rm close,SC}$	$\epsilon_{\rm SC}$	$\theta_{\rm E}/4$	Section 4.4.4
Detection efficiency for a lens companion	$\epsilon_{\rm LC}$	$q_{\rm LC}$, $a_{\rm LC}$	$\Theta[(\phi - \phi_{\rm wide})(\phi - \phi_{\rm close,LC})]$ [a]	Section 4.4.4
Close limit of undetectable lens companion	$\phi_{\rm close,LC}$	$\epsilon_{\rm LC}$	$\theta_{\rm E}(\sqrt{q_{\rm LC}/u_0 + 1} + \sqrt{q_{\rm LC}/u_0})$	Section 4.4.4

Notes.
[a] Θ is the Heaviside step function.
[b] Abbreviation of $f_{\rm pri}(M_L, D_L, D_S, v_{\rm t}\lvert t_{\rm E} = t_{\rm E,obs}, \theta_{\rm E} = \theta_{\rm E,obs}, \pi_{\rm E} = \pi_{\rm E,obs})$.
[c] Galactic model consists of the density distribution, the velocity distribution, the present-day mass function, and the planet-hosting probability for stellar objects in our galaxy.
[d] Likelihood of $(t_{\rm E,obs}, \theta_{\rm E,obs}, \pi_{\rm E,obs})$, where a 3D normal distribution with reported values and errors (listed in Table 3) is applied. No correlation among the three is assumed.
[e] $\mathcal{N}(\overline{T}, \sigma_T)$ is the normal distribution with the mean $\overline{T}$ and the standard deviation σ_T.
[f] $\Lambda(a; \eta_{\log a}, \sigma^2_{\log a})$ is the log-normal distribution.

Table 3
Input Parameters Needed to Calculate the Prior/Posterior PDFs and Our Choices for Them

Input Parameter	Notation	To Model	M16227 (1)	M08310 (2)	M11293 (3, 4)	O120563 (5)	O120950 (6)
For prior PDF							
Einstein-radius-crossing time	$t_{\rm E,obs}$ (days)	$f'_{\rm pri}(M_L, D_L, D_S, v_t)$[a]	17.0 ± 0.2	11.1 ± 0.5	21.7 ± 0.1	78 ± 2	68 ± 2
Angular Einstein radius	$\theta_{\rm E,obs}$ (mas)	$f'_{\rm pri}(M_L, D_L, D_S, v_t)$[a]	0.23 ± 0.01	0.16 ± 0.01	0.26 ± 0.02	1.4 ± 0.1	⋯
Microlensing parallax	$\pi_{\rm E,obs}$	$f'_{\rm pri}(M_L, D_L, D_S, v_t)$[a]	⋯	⋯	⋯	⋯	0.26 ± 0.06
Impact parameter	$u_{0,\rm obs}$	$\epsilon_{\rm LC}$	0.08	0.003	0.0035	0.001	0.10
Source flux	$H_{S,\rm obs}$ (mag)	M_S	17.81 ± 0.02	17.73 ± 0.05	19.20 ± 0.06	18.57 ± 0.03	17.78 ± 0.12
Mean extinction for red clump in the field	$A_{H,\rm rc}$ (mag)	$A_{H,S}$, $A_{H,L}$	0.19 ± 0.02	0.33 ± 0.10	0.47 ± 0.10[b]	0.26 ± 0.02	0.25 ± 0.03
Mean distance modulus to the red clump stars	$\rm DM_{rc}$	$A_{H,S}$, $A_{H,L}$	14.48 ± 0.24	14.70 ± 0.28	14.52 ± 0.19	14.48 ± 0.24	14.50 ± 0.26
Number density of ambient stars in the field	$n_{\rm amb}$ ($\rm as^{-2}$)	$f_{\rm pri}(F_{\rm amb})$	7.3	5.5	7.3	7.3	4.0
Wide limit of undetectable stars in AO image	$\phi_{\rm wide}$ (mas)	$\epsilon_{\rm amb}$, $\epsilon_{\rm LC}$, $\epsilon_{\rm SC}$	148	132	60	160	90
For posterior PDF							
Excess flux measured by AO imaging	$H_{\rm ex,obs}$ (mag)	$f_{\rm post}{}'(F_L, F_{\rm amb}, F_{\rm SC}, F_{\rm LC})$[c]	19.7 ± 0.4	19.6 ± 0.4	19.16 ± 0.13	17.80 ± 0.07	17.52 ± 0.10

Notes. All values of parameters other than $\rm DM_{rc}$ and $n_{\rm amb}$ are from the indicated references. $\rm DM_{rc}$ is from Nataf et al. (2013) while we derive $n_{\rm amb}$ in Section 4.1.1. A normal distribution is assumed for each parameter, but in flux units for $H_{S,\rm obs}$ and $H_{\rm ex,obs}$. A blank (⋯) for $\theta_{\rm E,obs}$ or $\pi_{\rm E,obs}$ indicates no constraint on the parameter, i.e., an infinite uncertainty.
[a] Abbreviation of $f_{\rm pri}(M_L, D_L, D_S, v_t|t_{\rm E} = t_{\rm E,obs}, \theta_{\rm E} = \theta_{\rm E,obs}, \pi_{\rm E} = \pi_{\rm E,obs})$.
[b] A value given by Batista et al. (2014) using the extinction law of Nishiyama et al. (2009). They also used $A_H = 0.65 \pm 0.12$ estimated with the extinction law of Cardelli et al. (1989), which is not used in our analysis.
[c] Abbreviation of $f_{\rm post}(F_L, F_{\rm amb}, F_{\rm SC}, F_{\rm LC}|F_{\rm excess} = F_{\rm ex,obs})$.
References. (1) Koshimoto et al. (2017a), (2) Janczak et al. (2010), (3) Yee et al. (2012), (4) Batista et al. (2014), (5) Fukui et al. (2015), (6) Koshimoto et al. (2017b).

Source companion flux—In this paper, we analyze events where no stellar companion is detected through the light curve or AO imaging; thus, we simulate the source companion using the undetected binary distribution, which combines the full binary distribution and detection efficiency for a companion.

Because the source star can be either a single star or the primary or secondary star in a binary system, we use the binary distribution for such an arbitrary star, $f_{\rm arb}(q, a|M)$, introduced in Section 4.4, as the full binary distribution. In each trial of the Monte Carlo simulation, this function gives the mass ratio of either $q_{\rm SC} = 0$, $0 < q_{\rm SC} \leqslant 1$, or $q_{\rm SC} > 1$, meaning that the arbitrary star (i.e., the source star here) is a single, primary, or secondary star, respectively, in addition to the semimajor axis $a_{\rm SC}$. Because $f_{\rm arb}(q, a|M)$ depends on the arbitrary star mass M, we need to input the source mass M_S obtained by applying the mass–luminosity relation to the source's absolute magnitude $\mathcal{M}_{H,S} = H_{S,\rm obs} - A_{H,S} - \rm DM_S$. We have the source distance D_S from $f_{\rm pri}(M_L, D_L, D_S, v_t|t_{\rm E} = t_{\rm E,obs}, \theta_{\rm E} = \theta_{\rm E,obs}, \pi_{\rm E} = \pi_{\rm E,obs})$ and use it to calculate the extinction $A_{H,\ S}$ and distance modulus $\rm DM_S$. The source magnitude $H_{S,\rm obs}$ is another input parameter needed, and we take the value from the previous paper for each event.

For the detection efficiency, we use $\epsilon_{\rm SC} = \Theta[(\phi - \phi_{\rm wide})(\phi - \phi_{\rm close,SC})]$, where Θ is the Heaviside step function. That is, we assume that a source companion whose projected angular separation ϕ is smaller than $\phi_{\rm close,SC} = \theta_{\rm E}/4$ or larger than the resolution element size of the AO image $\phi_{\rm wide}$ is detectable through the light curve or AO imaging, respectively. By accepting a combination of $q_{\rm SC}$ and $a_{\rm SC}$ that gives $\epsilon_{\rm SC} = 0$ in the simulation, we have the undetected binary distribution and can calculate the magnitude $H_{\rm SC}$ for the accepted companion using the mass–luminosity relation.

Lens companion flux—The lens companion flux is simulated by a similar process to that of the source companion. Given the lens mass M_L from $f_{\rm pri}(M_L, D_L, D_S, v_t|t_{\rm E} = t_{\rm E,obs}, \theta_{\rm E} = \theta_{\rm E,obs}, \pi_{\rm E} = \pi_{\rm E,obs})$ as input to $f_{\rm arb}(q, a|M)$, we have $q_{\rm LC}$ and $a_{\rm LC}$ in each trial of the Monte Carlo simulation. If the projected angular separation ϕ satisfies $\phi_{\rm close,LC} < \phi < \phi_{\rm wide}$, we accept the trial and calculate the magnitude $H_{\rm LC}$. This means that we use the detection efficiency $\epsilon_{\rm LC} = \Theta[(\phi - \phi_{\rm wide})(\phi - \phi_{\rm close,LC})]$ for the lens companion and the closer limit $\phi_{\rm close,LC} = \theta_{\rm E}(\sqrt{q_{\rm LC}/u_0 + 1} + \sqrt{q_{\rm LC}/u_0})$, where u_0 is the microlensing impact parameter, and we use $u_{0,\rm obs}$ taken from the previous paper for each event in Table 3. This limit comes from the comparison between the central caustic size created by the lens companion and impact parameter, which are described in Section 4.4.4.

3.1.2. Calculation of the Posterior PDF

Once we have the joint prior PDF $f_{\rm pri}(F_L, F_{\rm amb}, F_{\rm SC}, F_{\rm LC})$, it is straightforward to derive the joint posterior PDF of Equation (4) numerically by randomly selecting combinations of the four flux values following the prior PDF and accepting only the combinations that satisfy the condition $F_{\rm excess} = F_{\rm ex,obs}$ within the measurement uncertainty (see the right box in Figure 1). Here we use the Gaussian distribution in flux units to judge whether $F_{\rm excess}$ is consistent with $F_{\rm ex,obs}$. This requires the last input parameter, the excess flux measured by AO imaging (in magnitude), $H_{\rm ex,obs}$, and the value taken from the previous paper for each event listed in the last line in Table 3.

This procedure automatically determines the posterior PDFs of all the parameters that are required to calculate these four fluxes listed in Table 1 including the lens mass M_L and distance D_L.

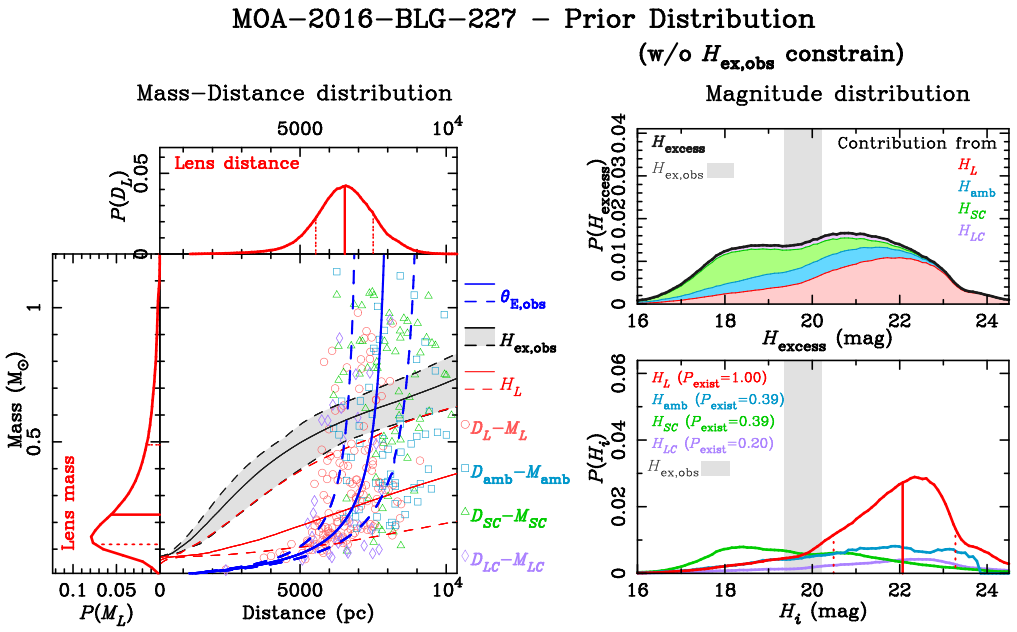

Figure 2. (a) Prior and (b) posterior probability distributions for M16227. On the left plane, some accepted combinations of mass and distance of the four contributors are shown in different symbols and colors, in addition to the mass–distance relation curves for each parameter indicated on the right. The left and top histogram curves along the plane represent the M_L and D_L probability distributions, respectively. The H_{excess} probability distribution is shown in the top-right panel, and the H_L, H_{amb}, H_{SC} and H_{LC} distributions are shown in the bottom-right panel. The probability of existence of each object is shown by P_{exist} in the bottom-right panel. Each colored area of the top-right panel indicates a contribution from each possible origin when the excess flux is the value at the horizontal axis. See Section 5.1 for details. The black point with the error bar in the left panel in (b) indicates the lens mass and distance when $H_L = H_{ex,obs}$.

4. Prior PDF

In this section, we describe the details of the calculation of the joint prior PDF $f_{pri}(F_L, F_{amb}, F_{SC}, F_{LC})$, which is summarized in Section 3.1.1. Because F_{amb} is independent of the other variables, we can split the prior joint PDF into two different functions: $f_{pri}(F_L, F_{amb}, F_{SC}, F_{LC}) = f_{pri}(F_L, F_{SC}, F_{LC}) f_{pri}(F_{amb})$. We discuss these two prior distributions in two different subsections. In Section 4.1, we discuss the prior PDF for the ambient star flux, F_{amb}. The joint prior PDF for the three parameters describing the flux of the lens and companion stars, namely F_L, F_{SC}, and F_{LC}, is discussed in Section 4.5.

As described in Section 3.1.1, the calculation of $f_{pri}(F_L, F_{SC}, F_{LC})$ requires the joint prior PDF of the lens mass M_L, distance D_L, source distance D_S, a mass–luminosity relation, and the undetected binary distribution. We describe the joint prior PDF of M_L, D_L, and D_S and the Galactic model,

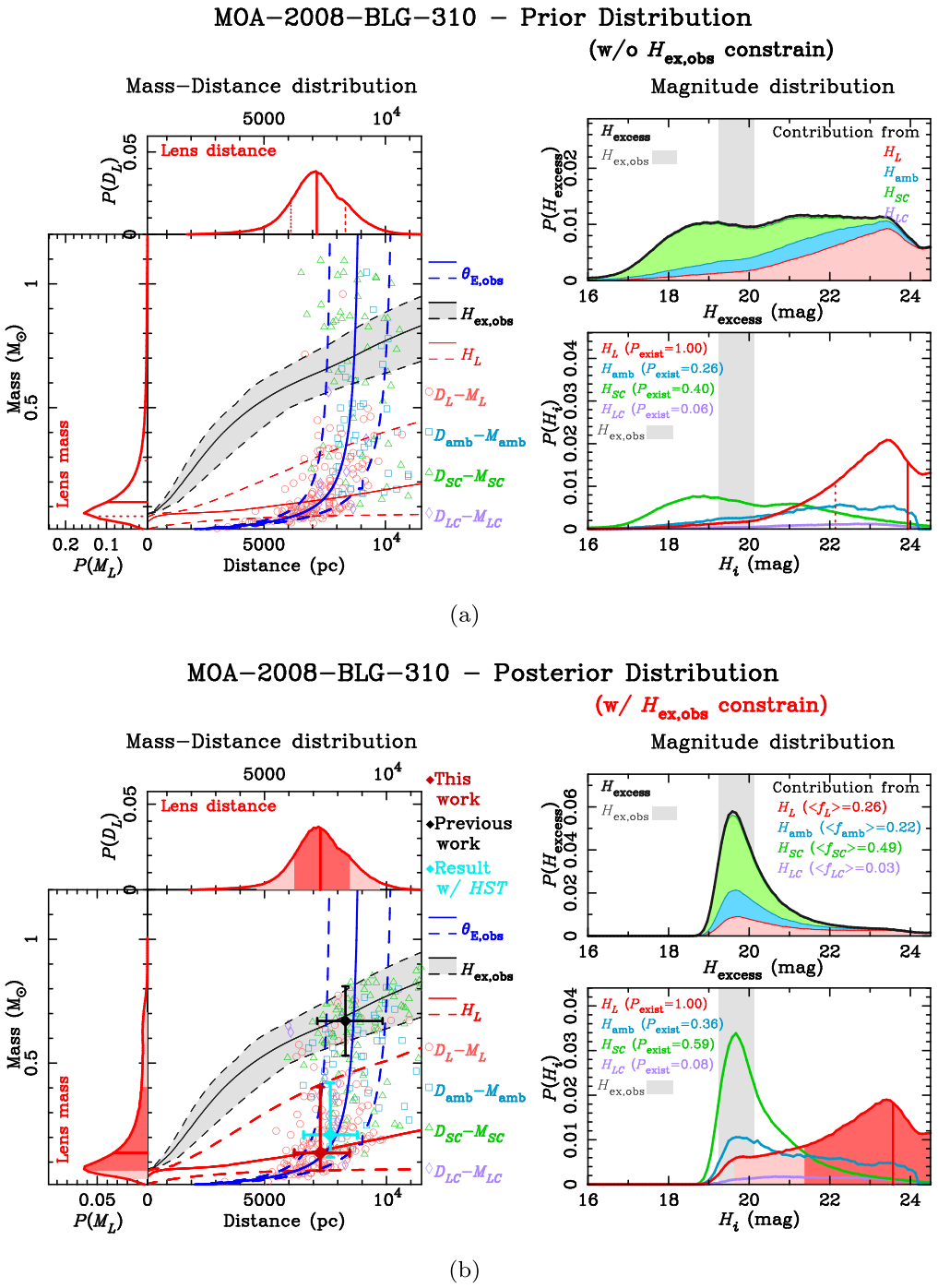

Figure 3. Same as Figure 2, but for M08310. (a) Prior and (b) posterior probability distributions. The lens mass and distance estimated by Janczak et al. (2010) and Bhattacharya et al. (2017) are indicated as "Previous work" and "Result w/HST," respectively, on the mass–distance plane in the posterior distribution.

which is needed to calculate the PDF in Section 4.2. Then, we describe the mass–luminosity relation used in this paper in Section 4.3. Section 4.4 describes the undetected binary distribution, which is needed to simulate F_{SC} and F_{LC}.

Again, Tables 2 and 3 summarize all models and input parameters that are needed to conduct the Bayesian analysis. These tables also show that the calculation of the said parameters or models requires those models or input parameters to be in the row denoted as "To model." The (a) components of Figures 2–6 show the results of the prior distributions calculated by the Monte Carlo simulation for each of the five events.

4.1. Ambient Star Flux Prior

4.1.1. Number Density of Ambient Stars

We can derive the number density of ambient stars n_{amb} by counting the stars in a region in the vicinity of the target in a high-angular-resolution image; however, such a count can be contaminated by incompleteness. We can correct for incompleteness with artificial star tests (Fukui et al. 2015) or comparison with an LF with high completeness (Koshimoto et al. 2017a). We use the latter method in this paper, i.e., we adopt the LF of Zoccali et al. (2003). Thus, our number density,

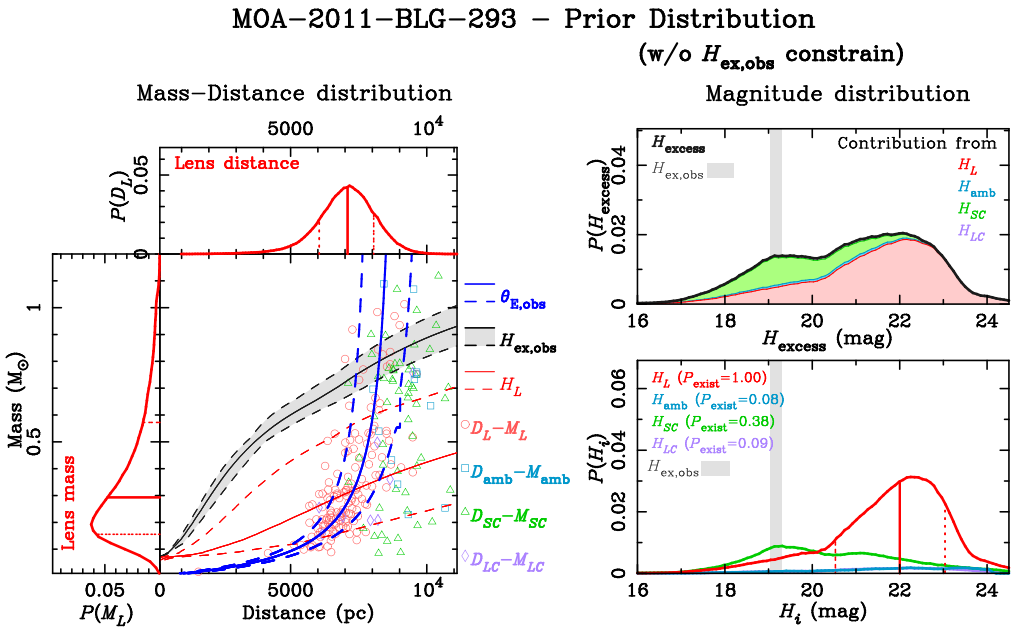

(a)

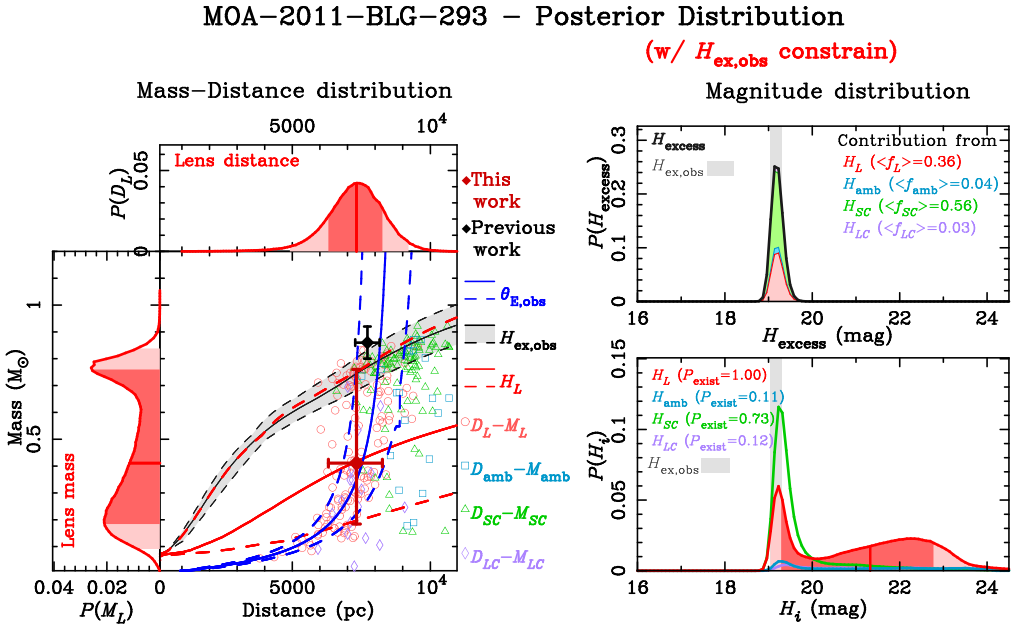

(b)

Figure 4. Same as Figure 2, but for M11293. (a) Prior and (b) posterior probability distributions. The lens mass and distance estimated by Batista et al. (2014) is indicated as "Previous work" on the mass–distance plane in the posterior distribution.

n_{amb}, includes only stars in the magnitude range covered by Zoccali et al. (2003), $H_0 = 7.7$–23.5 mag, where H_0 is the extinction-free magnitude. Fainter stars will make no significant contribution to the high-angular-resolution follow-up observations that we consider. A star with $H_0 > 23.5$ would have a contribution of only 2.5% for $H_{ex,obs} = 19.7$ mag for M16227 and a smaller fraction for the other targets. Even if three $H_0 > 23.5$ stars were to exist, this would be only up to a 7.5% contribution, much smaller than the magnitude excess ($H_{ex,obs}$) uncertainty of 0.4 mag for M16227. Our method includes a correction of the input LF to match the extinction, $A_{H,rc}$, and mean distance modulus, DM_{rc}, for the field of each event. That is, we add both the extinction $A_{H,rc}$ and the difference of DM_{rc} from the value for Zoccali's field, 14.51 (Nataf et al. 2013), to the extinction-free magnitude of the Zoccali et al. (2003) LF, where we use $A_{H,rc}$ and DM_{rc} in Table 3 for each event and ignore their uncertainty.

We derive the n_{amb} values for M16227 and O120950 following Koshimoto et al. (2017a), using the number density of stars in high-angular-resolution Keck AO images around each

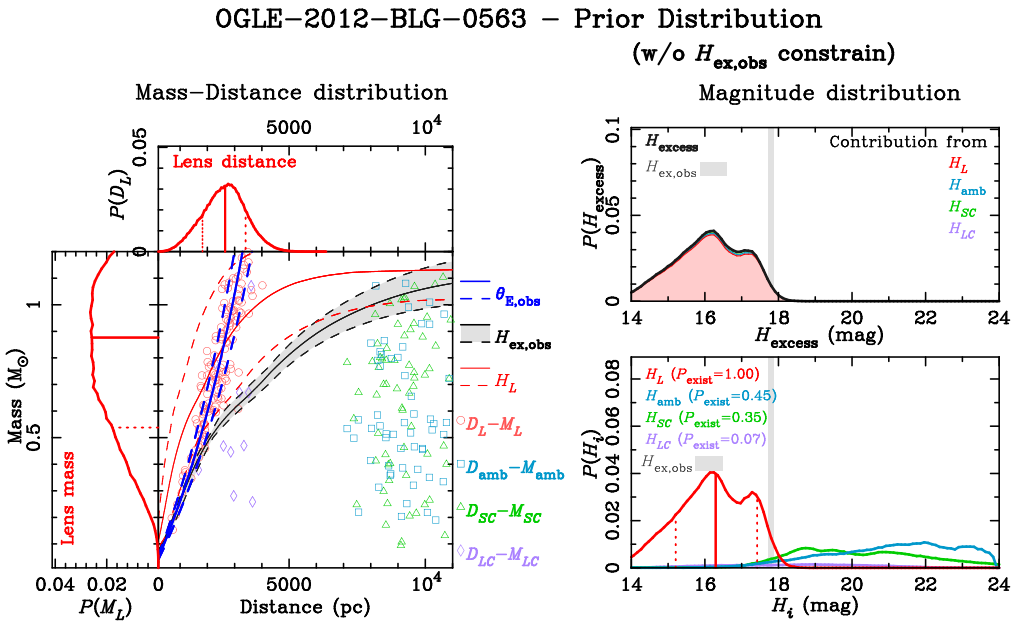

(a)

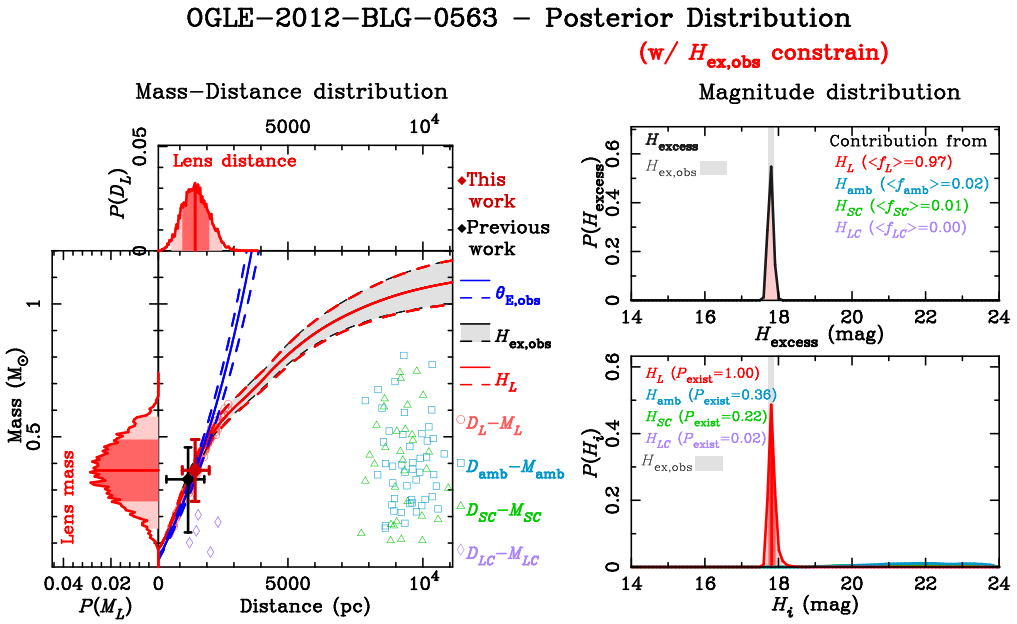

(b)

Figure 5. Same as Figure 2, but for O120563. (a) Prior and (b) posterior probability distributions. The lens mass and the distance estimated by Fukui et al. (2015) is indicated as "Previous work" on the mass–distance plane in the posterior distribution.

target. This can be done because we have access to the data of the Keck images for these two events unlike the other three events. First, we plot the observed H-band LFs for the Keck AO images for these two targets (see the solid histogram curves in Figure 7), and we see that the LFs decrease at $H \gtrsim 19.5$ mag in both cases, indicating severe incompleteness. We count the stars with $H < 17.91$ in the AO image for M16227 and those with $H < 17.99$ in the AO image for O120950, and we assume that the detection completeness is 100% for these stars. Then, we use these numbers for the normalization of the Zoccali et al. (2003) LF for each image (see the dashed curves in Figure 7). For the Subaru AO image of O120563, Fukui et al. (2015) measured the detection completeness of stars with $18.55 < H < 19.11$ as 72%. The depth of the Keck AO images is similar to that of the Subaru images. The field of O120563 has a star density similar to that of M16227, and it is denser than that of O120950. Hence, we believe that our completeness assumption is reasonable. Figure 7 compares the observed H-band LFs for the Keck AO images for these two targets (solid histogram curves) with the scaled LFs of Zoccali et al. (2003; dashed curves) for

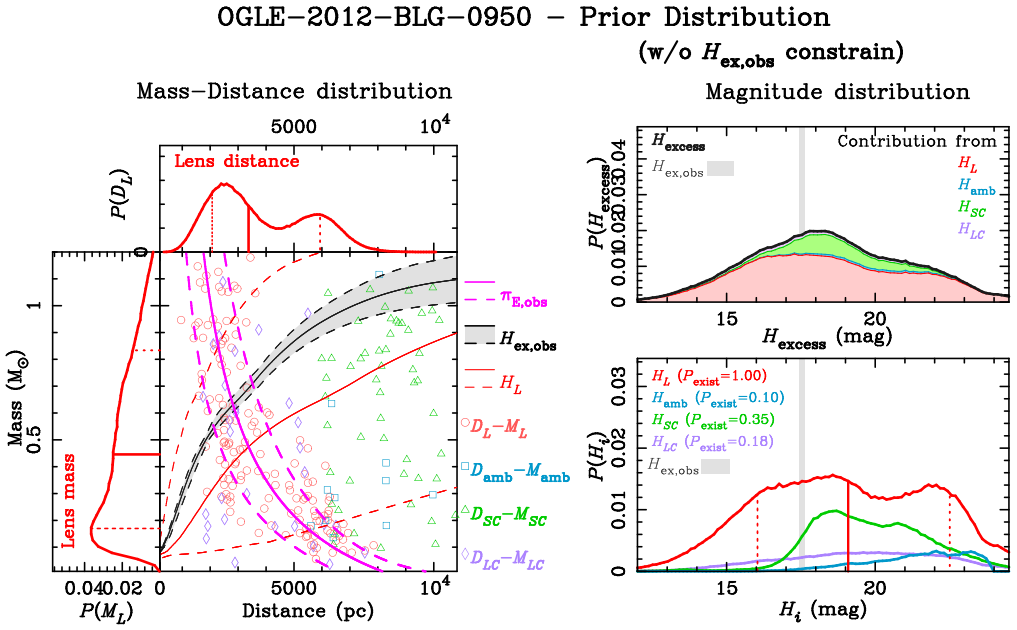

(a)

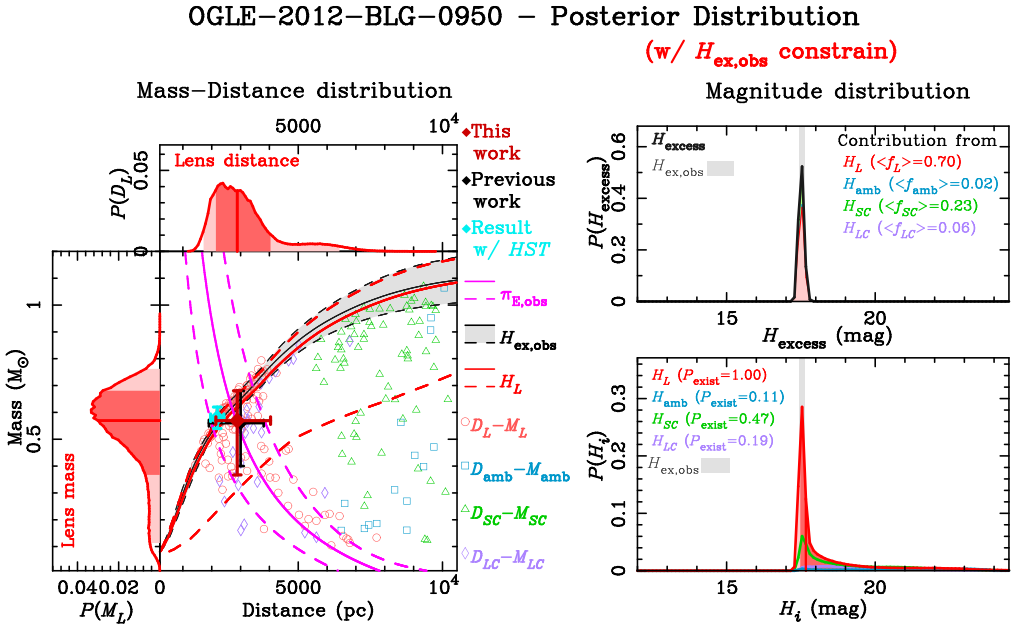

(b)

Figure 6. Same as Figure 2, but for O120950. (a) Prior and (b) posterior probability distributions. The lens mass and distance estimated by Koshimoto et al. (2017b) and Bhattacharya et al. (2018) are indicated as "Previous work" and "Result w/HST," respectively, on the mass–distance plane in the posterior distribution.

each field. By integrating the scaled LF and dividing it by the area of each field, we find that $n_{amb} = 7.3 \pm 1.0$ as^{-2} for M16227 and $n_{amb} = 4.0 \pm 0.6$ as^{-2} for O120950, where the unit as^{-2} indicates arcsec^{-2}.

We also compared the number of red clump stars in the M08310 field with that in the field observed by Zoccali et al. (2003) using the OGLE-III catalog (Szymański et al. 2011) to obtain an ambient star density of $n_{amb} = 5.5 \pm 1.7$ as^{-2}. We use the same n_{amb} value as that of M16227 for M11293 and O120563 because M11293 is not located in the OGLE-III survey field and the O120563 coordinate is very close to the M16227 coordinate, with a separation of 53″. Note that a large uncertainty in the n_{amb} value for M11293 does not affect the result because of the very small ϕ_{wide} value of the AO observation for this event, which leads to a negligible contribution from ambient stars to the excess flux.[5]

[5] This statement could be false if the assumed n_{amb} value for M11293 is significantly underestimated. However, it is likely overestimated. Batista et al. (2014) reported the number density of 0.106 as^{-2} for stars of $18.66 < H < 19.66$ in the AO image for M11293, which is more than three times smaller than the number density of 0.358 as^{-2} for stars in the same brightness range in the AO image for M16227. Although neither of these values are corrected for detection completeness, the completeness of the M11293 image is likely to be higher than that for the M16227 image considering its ∼2.5 times smaller ϕ_{wide} value than that for M16227.

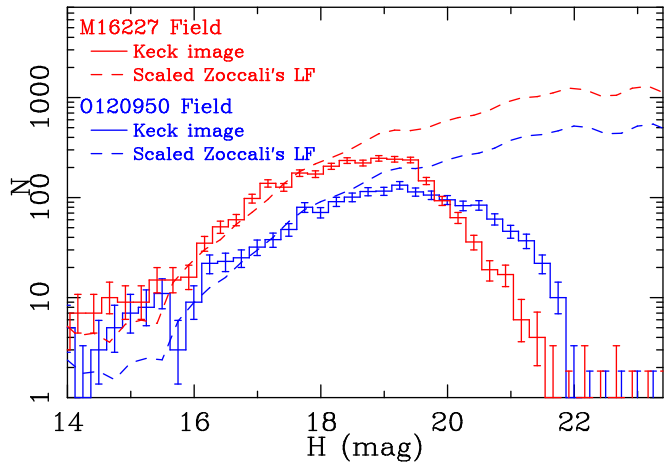

Figure 7. Luminosity function in Keck AO images (histogram curves) and that of Zoccali et al. (2003) scaled to the field's area and number density (dashed curves) for the fields of M16227 (red) and O120950 (blue). The dashed curves are scaled so that the number of stars equals the histogram curves in the magnitude range of $H < 17.91$ for M16227 and $H < 17.99$ for O120950. See Section 4.1 for details.

4.1.2. Ambient Star Flux Distribution

If an ambient star is sufficiently close to the source star in our high-resolution images, we will not be able to resolve it from the source. We denote the separation angle that is the boundary between resolved and unresolved stars by $\phi_{\rm wide}$. All the papers that measured the excess fluxes analyzed in this paper set this limit as a constant. We use the value from the previous paper as the $\phi_{\rm wide}$ for each event, as listed in Table 3. For example, Koshimoto et al. (2017a) used $\phi_{\rm wide} = 0.8$ FWHM, where the FWHM of 186 mas is the FWHM of the objects in the Keck AO image for M16227. These limits were conservatively set by each study in which the authors were able to resolve an object with excess brightness. However, objects much fainter than the excess brightness can be missed even at $>\phi_{\rm wide}$, because most of those previous studies have considered only the possibility of contamination by a star with excess brightness.

Nevertheless, we assume that this limit does not depend on the brightness of the source and the hypothetical blended star. This is for simplicity, to fairly compare our results with previous studies that used this limit as constant, and above all because our results are little affected by the ambient stars as shown in Section 9.1. This is equivalent to setting the detection efficiency of ambient stars located at an angular separation ϕ from the source star centroid as

$$\epsilon_{\rm amb} = \Theta(\phi - \phi_{\rm wide}), \tag{7}$$

where Θ is the Heaviside step function.

Under the assumption that stars are uniformly randomly distributed in the image with a constant number density $n_{\rm amb}$, the number of unrelated ambient stars $N_{\rm amb}$ within a circle of radius $\phi_{\rm wide}$ will follow the Poisson distribution

$$\mathrm{Po}(N_{\rm amb};\, \lambda_{\rm amb}) = \frac{\lambda_{\rm amb}^{N_{\rm amb}}\, e^{-\lambda_{\rm amb}}}{N_{\rm amb}!}, \tag{8}$$

where $\lambda_{\rm amb}$ is the mean value of $N_{\rm amb}$ and

$$\lambda_{\rm amb} = n_{\rm amb}\, \pi\, \phi_{\rm wide}^2. \tag{9}$$

Next, we consider the distribution of the total flux from N stars that are blended together, $L_N(F_{\rm total})$, where $F_{\rm total} = \sum_{i=1}^{N} F_i$ and N is fixed. Because we derived $n_{\rm amb}$ using the LF of Zoccali et al. (2003), the flux distribution of a single ambient star, $L_1(F)$, follows this LF. Because the flux from each component of the stellar blend, F_i, also follows the LF $L_1(F_i)$, the LF for the total flux $F_{\rm total} = \sum_{i=1}^{N} F_i$ can be calculated using the recurrence formula

$$L_N(F_{\rm total}) = \int_0^{F_{\rm total}} L_{N-1}(F)\, L_1(F_{\rm total} - F)\, dF. \tag{10}$$

By combining Equations (8) and (10), we can derive the prior PDF of the ambient star flux $F_{\rm amb}$:

$$f_{\rm pri}(F_{\rm amb}) = \mathrm{Po}(0;\, \lambda_{\rm amb})\, \delta(F_{\rm amb}) + \sum_{N_{\rm amb}=1}^{\infty} \mathrm{Po}(N_{\rm amb};\, \lambda_{\rm amb})\, L_{N_{\rm amb}}(F_{\rm amb}), \tag{11}$$

where $\delta(F_{\rm amb})$ is the Dirac delta function, and we define $L_{N_{\rm amb}}(F = 0) = 0$. Although this distribution seems to depend only on $\lambda_{\rm amb}$, we note that it also depends on the average distance modulus $\mathrm{DM}_{\rm rc}$ and the extinction of the stars in the selected field.

The cyan solid line in the bottom-right panel of each (a) component of Figures 2–6 represents the prior probability distribution for the H-band ambient star flux, $f_{\rm pri}(F_{\rm amb})$. This requires the use of the $n_{\rm amb}$, $\phi_{\rm wide}$, $A_{H,\rm rc}$, and $\mathrm{DM}_{\rm rc}$ values for each event, where we do not include the uncertainties of those parameters for $F_{\rm amb}$. We do not include a bin for $F_{\rm amb} = 0$ because this corresponds to $H_{\rm amb} = \infty$. Instead, we denote the probability of $N_{\rm amb} > 0$ as $P_{\rm exist}$ in the cyan label in each figure, where $P_{\rm exist} = 1 - \mathrm{Po}(0, \lambda_{\rm amb})$ for ambient stars.

4.2. Priors for the Lens Mass and Distance and the Source Distance

Many previous studies have estimated event properties via Bayesian analysis based on a standard Galactic model and the observed Einstein-radius-crossing time, $t_{\rm E,obs}$; angular Einstein radius, $\theta_{\rm E,obs}$; and microlensing parallax, $\pi_{\rm E,obs}$ (Alcock et al. 1995; Beaulieu et al. 2006; Bennett et al. 2014; Koshimoto et al. 2014). These studies produced PDFs for the lens system properties that are referred to as "posterior" distributions; however, in this study, we consider these distributions to be "prior" distributions, because we are considering the effect of high-angular-resolution follow-up observations on the inferred properties of the lens systems.

We employ the input Galactic model, described below in Section 4.2.1, to provide our prior PDF for the lens mass M_L, the distances to the lens and source stars, D_L and D_S, respectively, and the relative transverse velocity between the lens and the line of sight to the source, $v_{\rm t}$, i.e., $f_{\rm pri}(M_L, D_L, D_S, v_{\rm t} | t_{\rm E} = t_{\rm E,obs}, \theta_{\rm E} = \theta_{\rm E,obs}, \pi_{\rm E} = \pi_{\rm E,obs})$, using the same method as that used in the above-mentioned studies, where a 3D normal distribution with no correlation among the three is assumed for the likelihood of $t_{\rm E,obs}$, $\theta_{\rm E,obs}$, and $\pi_{\rm E,obs}$. When light-curve fitting is conducted, there is often a correlation especially among $t_{\rm E}$, $\pi_{\rm E}$, the source flux $F_{\rm S}$, and the blending flux. Although we do not use the blending flux in our calculation as explained in Section 3, we do use $t_{\rm E}$, $\pi_{\rm E}$, and also $F_{\rm S}$, which is used to calculate $F_{\rm ex,obs}$. Therefore, one should ideally apply the joint probability distribution of the fitting parameters, which is an output of the Markov Chain Monte Carlo fitting to the event light-curve data, instead of the normal distribution. Including the correlation might lead to a different result when the uncertainty of each parameter is very large. However, it is not the case for the five events analyzed in this paper, and we do not expect much difference in our results due

to the correlation. Hereafter, we use the notation $f'_{\rm pri}(M_L, D_L, D_S, v_{\rm t})$ instead of $f_{\rm pri}(M_L, D_L, D_S, v_{\rm t}|t_{\rm E} = t_{\rm E,obs}, \theta_{\rm E} = \theta_{\rm E,obs}, \pi_{\rm E} = \pi_{\rm E,obs})$ because this expression is less cumbersome.

Note that we do not consider remnants, assuming that their probability of hosting planets detectable by microlensing is low. We discuss this assumption in Section 9.6.

4.2.1. Galactic Model

We use the S11 model from Koshimoto & Bennett (2019) as our fiducial Galactic model while we apply different models in Section 9.4. The S11 model is a slightly modified version of the Sumi et al. (2011) model, who constructed the model based on Han & Gould (1995). The density model consists of the boxy-shaped bulge model (Dwek et al. 1995)

$$\rho_B = \rho_{0,B} \exp(-0.5 r_s^2), \tag{12}$$

where $r_s = \{[(x'/x_0)^2 + (y'/y_0)^2]^2 + (z'/z_0)^4\}^{1/4}$ and the origin of the (x', y', z') coordinate is the galactic center. The x'-axis is along the long axis of the bar, which is inclined at 20° to the Sun's direction, the y'-axis is perpendicular to the x'-axis on the galactic plane, and the z'-axis is toward the galactic north pole. Moreover, $R = (x^2 + y^2)^{1/2}$ and the (x, y, z) coordinate rotates the (x', y', z') coordinate such that the x-axis is toward the Sun's direction. The S11 model uses the galactic bar parameters of $\rho_{0,B} = 2.07\ M_\odot\ \ {\rm pc}^{-3}$, $x_0 = 1580$ pc, $y_0 = 620$ pc, and $z_0 = 430$ pc for the parameters in ρ_B (Han & Gould 1995; Alcock et al. 1997).

For the galactic disk, we use the model of Bahcall (1986), i.e.,

$$\rho_D = \rho_{0,D} \exp\left[-\left(\frac{R - R_{\rm GC}}{R_0} + \frac{z}{z_{0,D}}\right)\right], \tag{13}$$

with $\rho_{0,D} = 0.06\ M_\odot\ \ {\rm pc}^{-3}$, $R_{\rm GC} = 8000$ pc, $R_0 = 3500$ pc, and $z_{0,D} = 325$ pc for the parameters in ρ_D.

For the velocity distribution of disk stars, we use the disk rotation speed of 220 km s^{-1} and velocity dispersions of 30 and 30 km s^{-1} along the azimuthal axis and z-axis, respectively. A streaming velocity of 50 km s^{-1} along the x'-axis is included, and velocity dispersions of (113.6, 77.4, 66.3) km s^{-1} are used along the x'-, y'-, and z'-axes for bar stars.

We consider the present-day mass function $\Phi_{\rm PD}(M)$ as follows. First, we take the initial mass function (IMF) to be

$$\Phi_{\rm IMF}(M)\, dM \propto \begin{cases} M^{-2.0}\, dM & \text{when } M > 0.7\ M_\odot \\ M^{-1.3}\, dM & \text{when } 0.08\ M_\odot < M \leqslant 0.7\ M_\odot \\ M^{-0.5}\, dM & \text{when } 0.01\ M_\odot < M \leqslant 0.08\ M_\odot, \end{cases} \tag{14}$$

where the slopes and breaks are taken from model 4 presented in the Supplementary Information of Sumi et al. (2011), but the high-mass end at $M = 1\ M_\odot$ is taken away to make it an IMF. We set the minimum mass limit to $0.01\ M_\odot$ to avoid the controversial extension of this mass function into the planetary-mass regime (Mróz et al. 2017).

To construct a present-day mass function from the IMF, we need an age distribution. The original high-mass cutoff at $M = 1\ M_\odot$ in Sumi et al. (2011) corresponds to an assumption that all stars are at ∼10 Gyr because a star with initial mass of $M = 1\ M_\odot$ evolves into a white dwarf at ∼10 Gyr. In this paper, we assume a normal distribution for stellar age T instead of the original mono-age assumption. Let $\overline{T}$ and σ_T be, respectively, the mean age and the standard deviation. We use $\overline{T} = 5$ Gyr and $\sigma_T = 2$ Gyr for the disk component, and $\overline{T} = 9$ Gyr and $\sigma_T = 1$ Gyr for the bulge component. We also limit the disk stars to lie within the age range 1 Gyr $< T <$ 10 Gyr and the bulge stars to lie within the range 4 Gyr $< T <$ 11 Gyr. We assume solar metallicity for the stellar metallicity, which somewhat affects the lifetime of a star.

By combining the age and metallicity assumptions with the IMF, we construct the present-day mass function $\Phi_{\rm PD}(M)$, where we use the PARSEC isochrones (Bressan et al. 2012; Chen et al. 2014, 2015; Tang et al. 2014) model to determine whether or not the star with the picked initial mass and age has evolved into a remnant. If it is not a remnant yet, then we accept the star with the picked mass; otherwise, we reject it because we do not consider compact objects in this paper. This Monte Carlo procedure automatically provides a reasonable edge of the high-mass side of the mass function corresponding to the age distribution used.

Another assumption that we need to consider is the planet-hosting probability, which is previously unknown, because we select lens stars that host planets. First, we perform the Bayesian analysis assuming all stars host planets with the same probability in Section 5. In Section 8, we apply different priors to the planet-hosting probability and show the extent to which our results depend on the prior.

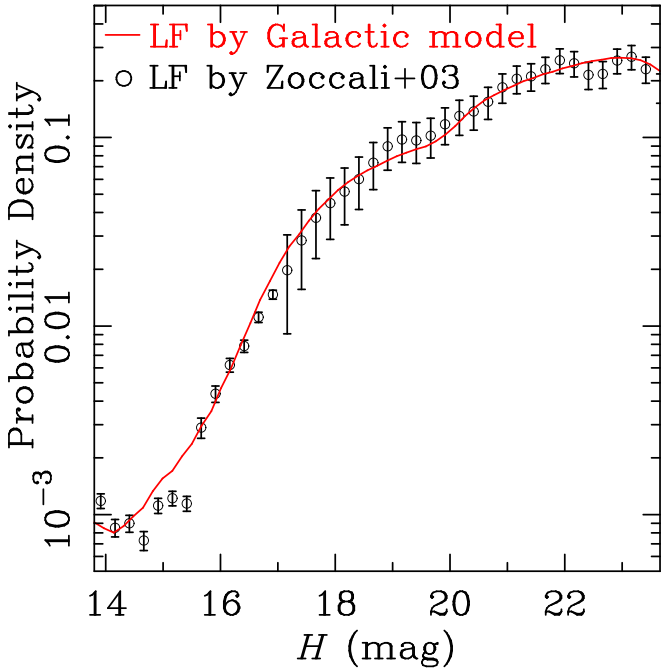

Figure 8. Comparison of the luminosity function calculated using the mass–luminosity relation and the Galactic model (the S11 model) with the luminosity function of Zoccali et al. (2003) in the H band, where the extinction, mean distance modulus, and galactic coordinate toward M16227 are used. The error bars of the Zoccali et al. (2003) LF are from the Poissonian errors they reported.

4.3. Mass–Luminosity Relation

The next component needed to calculate the prior PDF $f_{\rm pri}(F_L, F_{\rm SC}, F_{\rm LC})$ is the mass–luminosity relation. In this study, we use different mass–luminosity relations depending on the mass

of a star. For high-mass stars ($M \geqslant 0.80\,M_{\odot}$), where the stellar evolution has a large effect on the luminosity, we use PARSEC isochrones (Bressan et al. 2012; Chen et al. 2014, 2015; Tang et al. 2014), where we assume solar metallicity and select the age T from the age distribution described in Section 4.2.1. For the mass range $0.12\,M_{\odot} < M \leqslant 0.78\,M_{\odot}$, we use the empirical relation used by Bennett et al. (2015), which combines the relations of Henry & McCarthy (1993) and Delfosse et al. (2000); we use the Henry & McCarthy (1993) relation for $M > 0.66\,M_{\odot}$, and we use the Delfosse et al. (2000) relation for $0.12\,M_{\odot} < M < 0.54\,M_{\odot}$. For low-mass stars ($M < 0.1\,M_{\odot}$) near brown dwarf transition, we use isochrone models of Baraffe et al. (2003) for substellar objects at an age of 5 Gyr. We linearly interpolate between the two relations used in the boundaries between these mass ranges.

Our choice of using the empirical relation for the intermediate-mass range rather than isochrones is motivated by the suggestion of Bennett et al. (2018a), who compared PARSEC isochrones with the same empirical mass–luminosity relation as ours and found disagreement between them.

To test the validity of our choices for the mass–luminosity relation and also for the Galactic model briefly, we calculate the bulge LF in the H band using those distributions. Figure 8 compares the model LF with the observed LF of Zoccali et al. (2003), which is used as $L_1(F)$ in the ambient star flux prior.[6] The error bars of the Zoccali et al. (2003) LF are from the Poissonian errors they reported. Because they combined near-IR data from observations using different instruments with different fields of view to derive the LF, the relative error does not increase monotonically with the value of the vertical axis. This plot shows that these two observational and model LFs are consistent with each other in the entire range related to lens stars in this paper, $H \gtrsim 17.5$, because $H_{\mathrm{ex,obs}} = 17.52 \pm 0.10$ is the brightest observed excess flux value in this paper.

We denote the H-band absolute magnitude as a function of the mass by $\mathcal{M}_H(M)$ from the mass–luminosity relations described above, and we denote the mass derived from the mass–luminosity relation and absolute magnitude by $M(\mathcal{M}_H)$.

4.4. Binary Distribution

In this section, we discuss the stellar binary distribution used in our calculations, as this distribution is another crucial component of the calculation of the prior PDF for $f_{\mathrm{pri}}(F_L, F_{\mathrm{SC}}, F_{\mathrm{LC}})$. We use the term binary distribution to refer to the probability that a star has a bound companion as a function of its mass ratio and semimajor axis.

As described in Section 3.1.1, we use the undetected binary distribution, which is a combination of the full binary distribution and detection efficiency, to calculate the source companion flux F_{SC} and lens companion flux F_{LC} in the Monte Carlo simulation to determine the prior PDF $f_{\mathrm{pri}}(F_L, F_{\mathrm{SC}}, F_{\mathrm{LC}})$. We describe the binary distribution for an ambient star, $f_{\mathrm{arb}}(q, a|M)$, in Section 4.4.1 because we use it as our full binary distribution. The calculation of $f_{\mathrm{arb}}(q, a|M)$ requires the binary distribution for a non-secondary star, which is described in Section 4.4.2. We show examples of the full binary distributions by applying the binary distribution for an ambient star to the source and lens systems in M16227 and M11293 in Section 4.4.3. Finally, Section 4.4.4 describes the detection efficiencies for a source companion ϵ_{SC} and a lens companion ϵ_{LC}, and their combination with the full binary distribution to derive the undetected binary distribution.

We make the following simplifying assumptions:

(i) We consider only binary systems and ignore the possibility of third-order and higher-order systems.
(ii) We do not consider the case where lens systems consisting of close binary stars have a gravitational lensing effect that closely resembles that of a single star (Bennett et al. 2016). We treat such systems as a resolvable binary system, and they are "rejected" in our Monte Carlo simulation shown in Figure 1.
(iii) We assume that the existence of the detected planet or planets does not affect the binary distribution.
(iv) We assume that the location of the star in our galaxy (i.e., differences in the surrounding stellar number density, metallicity, age, etc.) does not affect the binary distribution.

4.4.1. Binary Distribution for an Arbitrary Star

For each of the events that we consider, there is a source star, a lens star, and a planet orbiting the lens star. The properties of the source star are clearly independent of the planet orbiting the lens star, and we assume that the properties of the lens star do not depend on the properties or existence of the detected planet or planets. This allows us to use the same distributions to describe the lens and source systems.

In microlensing, the source and lens stars are selected randomly owing to the alignment with the other star (the lens or source star, respectively). Hence, the source or lens star could be a secondary star with a more massive companion. We consider the following cases for the target star, which can be either the source star or the lens star:

1. The target star is a single star with no stellar companion.
2. The target star is the primary star in a stellar binary system.
3. The target star is the secondary star in a stellar binary system.

Prior information about the target star is different from that in existing observational studies of binary star systems with nearby stars (Duquennoy & Mayor 1991; Allen 2007; Raghavan et al. 2010; Ward-Duong et al. 2015). The systems in these studies are selected on the basis of their brightness; hence, it is common to classify these systems on the basis of the properties of the brightest star in the system, which would be either the primary star or a single star. Hence, these are non-secondary stars. For microlensing events, we must include the possibility that the source and lens stars are secondary stars; hence, we cannot simply apply the observational results for non-secondary stars. In this paper, we refer to a star that could be in any of the three above-mentioned categories, such as the source star or the lens star, as an "arbitrary star" to distinguish it from a non-secondary star.

We represent the number density of systems that consist of a star of mass M and a second star of mass qM, separated by a semimajor axis a, by $\nu_{\mathrm{arb}}(M, q, a)dMdqda$, where $0 < M < \infty$, $0 \leqslant q < \infty$ and $0 \leqslant a < \infty$. We use $(q, a) = (0, 0)$ to indicate the frequency of single stars with mass M. Of course, binary systems with $0 < M < \infty$ and $0 < q \leqslant 1$ can also be represented by $0 < M < \infty$ and $1 < q < \infty$. Thus, $\nu_{\mathrm{arb}}(M, q, a)$ counts each binary system twice when it is

[6] The LF calculated by the Galactic model is another choice for $L_1(F)$ instead of the Zoccali et al. (2003) LF. However, we believe that using an observed LF as $L_1(F)$ is a more direct and less model-dependent way because some parameters in the Galactic model, such as the slopes of the mass function, were originally determined by the observation of the LF.

integrated over $0 < M < \infty$, $0 \leqslant q < \infty$ and $0 \leqslant a < \infty$. However, this double counting does not exist in what we pursue below, $f_{\rm arb}(q, a|M)$, the binary distribution for a given arbitrary star mass M. With this number density, the binary distribution for an arbitrary star (that is known to exist) with mass M is given by a conditional probability:

$$f_{\rm arb}(q, a|M) = \frac{\nu_{\rm arb}(M, q, a)}{\nu_{\rm arb}(M)}, \tag{15}$$

where

$$\nu_{\rm arb}(M) \equiv \int_0^\infty \int_0^\infty \nu_{\rm arb}(M, q, a)\, dqda.$$

We consider target stars that are either source or lens stars such that $M = M_S$ or $M = M_L$. We can calculate the probability that the source or the lens has a companion as well as the probability distribution of the mass ratio q and the semimajor axis a of such companions with $f_{\rm arb}(q, a|M)$. We consider the number density of arbitrary systems, $\nu_{\rm arb}(M, q, a)$, in the following.

The function $\nu_{\rm arb}(M, q, a)$ represents the number density in each of the three categories depending on the mass ratio q:

$$\nu_{\rm arb}(M, q, a) = \begin{cases} \nu_{\rm single}(M)\delta(q)\delta(a), & q = 0, a = 0 \\ \nu_{\rm prim}(M, q, a), & 0 < q \leqslant 1 \\ \nu_{\rm second}(M, q, a), & 1 < q < \infty. \end{cases} \tag{16}$$

The number density of binary systems consisting of a primary star whose mass is in the range of M–$M + dM$ and a secondary star whose mass is in the range of qM–$(q + dq)M$, separated by a semimajor axis in the range of a–$a + da$, is given by $\nu_{\rm prim}(M, q, a)\, dM\, dq\, da$. With changes in the variables $q' = 1/q$ and $M' = qM$, this function also indicates the frequency of binary systems with a secondary star whose mass is in the range of M'–$M' + dM'$ and a primary star whose mass is in the range of $q'M'$–$(q' + dq')M'$, separated by a semimajor axis in the range of a–$a + da$. This is the same as $\nu_{\rm second}(M', q', a)dM'dq'da$. This implies a relationship between $\nu_{\rm second}(M, q, a)$ and $\nu_{\rm prim}(M, q, a)$ given by

$$\begin{aligned} \nu_{\rm second}(M, q, a) &= \nu_{\rm prim}(qM, q^{-1}, a) \left| \frac{\partial(qM, q^{-1})}{\partial(M, q)} \right| \\ &= \nu_{\rm prim}(qM, q^{-1}, a)\, q^{-1}. \end{aligned} \tag{17}$$

This allows us to combine the three expressions in Equation (16) into a single expression,

$$\begin{aligned} \nu_{\rm arb}(M, q, a) &= \nu_{\rm single}(M)\, \delta(q)\, \delta(a) \\ &\quad + \nu_{\rm prim}(M, q, a) + \nu_{\rm second}(M, q, a) \\ &= \nu_{\rm single}(M)\, \delta(q)\, \delta(a) \\ &\quad + \nu_{\rm prim}(M, q, a) + \nu_{\rm prim}(qM, q^{-1}, a)\, q^{-1}, \end{aligned} \tag{18}$$

where we define the $\nu_{\rm prim}$, $\nu_{\rm second}$, and $\nu_{\rm single}$ functions to be zero outside the ranges specified in Equation (16).[7]

As mentioned above, existing studies on the binary distribution of nearby stars (Duquennoy & Mayor 1991; Allen 2007; Raghavan et al. 2010; Ward-Duong et al. 2015) presented the binary distribution for non-secondary stars as a function of their mass M. In particular, we refer to two functions given in these studies, namely the multiplicity fraction $\mathcal{F}_{\rm mult}(M)$ and the joint PDF for a secondary star with mass ratio q and semimajor axis a orbiting a primary star of mass M, $f_{\rm prim}(q, a|M)$. This is the binary distribution for a non-secondary star. The multiplicity fraction $\mathcal{F}_{\rm mult}(M)$ is the probability that a non-secondary star with mass M is a primary star, i.e.,

$$\mathcal{F}_{\rm mult}(M) = \frac{\nu_{\rm prim}(M)}{\nu_{\rm single}(M) + \nu_{\rm prim}(M)}, \tag{19}$$

where

$$\nu_{\rm prim}(M) \equiv \int_0^1 \left(\int_0^\infty \nu_{\rm prim}(M, q, a)\, da \right) dq.$$

The function $f_{\rm prim}(q, a|M)$ is the conditional probability for a secondary star with mass ratio $q < 1$ and semimajor axis a, given a primary star of mass M, and it is given by

$$f_{\rm prim}(q, a|M) = \frac{\nu_{\rm prim}(M, q, a)}{\nu_{\rm prim}(M)}. \tag{20}$$

We will present the form of the functions $\mathcal{F}_{\rm mult}(M)$ and $f_{\rm prim}(q, a|M)$ in Section 4.4.2.

To express $\nu_{\rm arb}(M, q, a)$ in terms of $\mathcal{F}_{\rm mult}(M)$ and $f_{\rm prim}(q, a|M)$, we insert two relations from Equations (19)–(20), i.e.,

$$\nu_{\rm prim}(M, q, a) = [\nu_{\rm single}(M) + \nu_{\rm prim}(M)]\, \mathcal{F}_{\rm mult}(M)\, f_{\rm prim}(q, a|M)$$

and

$$\nu_{\rm single}(M) = [\nu_{\rm single}(M) + \nu_{\rm prim}(M)]\, [1 - \mathcal{F}_{\rm mult}(M)],$$

into Equation (18), and we find that

$$\begin{aligned} \nu_{\rm arb}(M, q, a) &= [\nu_{\rm single}(M) + \nu_{\rm prim}(M)] \\ &\quad \times [1 - \mathcal{F}_{\rm mult}(M)]\, \delta(q)\, \delta(a) \\ &\quad + [\nu_{\rm single}(M) + \nu_{\rm prim}(M)] \\ &\quad \times \mathcal{F}_{\rm mult}(M)\, f_{\rm prim}(q, a|M) \\ &\quad + [\nu_{\rm single}(qM) + \nu_{\rm prim}(qM)] \\ &\quad \times \mathcal{F}_{\rm mult}(qM)\, f_{\rm prim}(q^{-1}, a|qM)\, q^{-1}. \end{aligned} \tag{21}$$

Now, we need an expression for $[\nu_{\rm single}(M) + \nu_{\rm prim}(M)]$. We use the stellar present-day mass function $\Phi_{\rm PD}(M)$ defined in Section 4.2.1 for it. In this paper, we assume that

$$[\nu_{\rm single}(M) + \nu_{\rm prim}(M)] = \nu_0\, \Phi_{\rm PD}(M), \tag{22}$$

where ν_0 is the number density of stellar systems at the location in question, which is canceled between the denominator and the numerator of $f_{\rm arb}(q, a|M)$. With this assumption, we have

$$\begin{aligned} \nu_{\rm arb}(M, q, a)/\nu_0 &= \Phi_{\rm PD}(M)\, [1 - \mathcal{F}_{\rm mult}(M)]\, \delta(q)\, \delta(a) \\ &\quad + \Phi_{\rm PD}(M)\, \mathcal{F}_{\rm mult}(M)\, f_{\rm prim}(q, a|M) \\ &\quad + \Phi_{\rm PD}(qM)\, \mathcal{F}_{\rm mult}(qM)\, f_{\rm prim}(q^{-1}, a|qM)\, q^{-1}, \end{aligned} \tag{23}$$

[7] We might consider an additional term $\nu_{\rm single}(qM)\, \delta(1/q)\, \delta(a)\, q^{-1}$ to include the frequency of a single star system with mass qM in $\nu_{\rm arb}(M, q, a)$. This would allow $\nu_{\rm arb}(M, q, a)$ to be invariant after the changes in the variables used in Equation (17), i.e., $q' = 1/q$ and $M' = qM$. However, this term has a nonzero value only when $M = 0$ and $q \to \infty$, and we will never consider these values. Hence, we do not include this term in $\nu_{\rm arb}(M, q, a)$ in this paper.

and thus

$$\nu_{\rm arb}(M)/\nu_0 = \Phi_{\rm PD}(M) + \int_1^\infty \left(\int_0^\infty \Phi_{\rm PD}(qM)\, \mathcal{F}_{\rm mult}(qM) \times f_{\rm prim}(q^{-1}, a|qM)\, q^{-1} da \right) dq \tag{24}$$

by integrating $\nu_{\rm arb}(M, q, a)$ over q and a.

Inserting these into Equation (15), we find the binary distribution for an arbitrary star with mass M:

$$f_{\rm arb}(q, a|M) = P_{\rm single}(M)\, \delta(q)\, \delta(a) + P_{\rm prim}(M)\, f_{\rm prim}(q, a|M) + P_{\rm second}(M)\, \frac{\Phi_{\rm PD}(qM)\, \mathcal{F}_{\rm mult}(qM)\, f_{\rm prim}(q^{-1}, a|qM)\, q^{-1}}{\int_1^\infty \left[\int_0^\infty \Phi_{\rm PD}(q'M)\, \mathcal{F}_{\rm mult}(q'M)\, f_{\rm prim}(q'^{-1}, a'|q'M)\, q'^{-1} da' \right] dq'}, \tag{25}$$

where $P_{\rm single}(M)$, $P_{\rm prim}(M)$, and $P_{\rm second}(M)$ are the probabilities that an arbitrary star with mass M is a single, primary, and secondary star, respectively. These are given by

$$P_{\rm single}(M) = \frac{\Phi_{\rm PD}(M)\, [1 - \mathcal{F}_{\rm mult}(M)]}{\nu_{\rm arb}(M)/\nu_0}, \tag{26}$$

$$P_{\rm prim}(M) = \frac{\Phi_{\rm PD}(M)\, \mathcal{F}_{\rm mult}(M)}{\nu_{\rm arb}(M)/\nu_0}, \tag{27}$$

$$P_{\rm second}(M) = \frac{\int_1^\infty \left[\int_0^\infty \Phi_{\rm PD}(qM)\, \mathcal{F}_{\rm mult}(qM)\, f_{\rm prim}(q^{-1}, a|qM)\, q^{-1} da \right] dq}{\nu_{\rm arb}(M)/\nu_0}, \tag{28}$$

where $P_{\rm single}(M) + P_{\rm prim}(M) + P_{\rm second}(M) = 1$ and the denominators are given by Equation (24). Equation (25) gives the complete probability distribution of an arbitrary star of mass M having a binary companion of any mass ratio and separation, including the case of $q = 0$ and $a = 0$, which represents single stars.

4.4.2. Binary Distribution for a Non-secondary Star

To calculate the binary distribution for an arbitrary star $f_{\rm arb}(q, a|M)$ given by Equation (25), we need to determine the forms of the binary distribution for a non-secondary star with mass M. This is the multiplicity fraction $\mathcal{F}_{\rm mult}(M)$, which is the fraction of primary stars with respect to non-secondary stars defined by Equation (19), times the joint PDF at mass ratio q and semimajor axis a for a primary star of mass M, $f_{\rm prim}(q, a|M)$, which is defined by Equation (20).

Following Duchêne & Kraus (2013), we assume that the mass ratio obeys a power-law distribution and the semimajor axis obeys a log-normal distribution. Hence, we use

$$f_{\rm prim}(q, a|M) \propto q^\gamma\, \Lambda(a; \eta_{\log a}, \sigma^2_{\log a}), \tag{29}$$

where $\Lambda(a; \eta_{\log a}, \sigma^2_{\log a})$ is the log-normal distribution, and $\eta_{\log a}$ and $\sigma_{\log a}$ are the mean and standard deviation of the associated normal distribution, respectively. Thus, there are four parameters that characterize the binary distribution for a non-secondary star of mass M, namely the multiplicity fraction $\mathcal{F}_{\rm mult}(M)$, the slope of the mass-ratio distribution, $\gamma = \gamma(a, M)$, and the mean $\eta_{\log a} = \eta_{\log a}(M)$ and standard deviation $\sigma_{\log a} = \sigma_{\log a}(M)$ of the logarithm of the semimajor axis. All these parameters are considered to be functions of M. The slope of the mass-ratio distribution $\gamma(a, M)$ depends on the primary mass M and its value depends on whether the logarithm of the semimajor axis is larger or smaller than its mean value:

$$\gamma(a, M) = \begin{cases} \gamma_c(M) & \text{when } \log[a/\text{au}] < \eta_{\log a}(M) \\ \gamma_w(M) & \text{when } \log[a/\text{au}] \geqslant \eta_{\log a}(M) \end{cases}. \tag{30}$$

We set $f_{\rm prim}(q, a|M) = 0$ with $q < 0.1$ because binaries with $q < 0.1$ are thought to be rare (Duchêne & Kraus 2013) and because such systems are rarely important for our calculations. Duchêne & Kraus (2013) derived the slope of the mass-ratio distribution, γ, using binary systems with $0.1 < q \leqslant 1$.

The mass dependence of these four parameters that characterize our $f_{\rm prim}(q, a|M)$ function is not well understood thus far. For our analysis, we fit each of these parameters to the data summarized by Duchêne & Kraus (2013) with two models that are linear in M and $\log M$, and we use the one that gives the better fit to the data for each parameter. In addition to the data summarized by Duchêne & Kraus (2013), we add the data at $M = 0.4 \pm 0.2\, M_\odot$ given by Ward-Duong et al. (2015) to determine the M dependence of $\mathcal{F}_{\rm mult}(M)$, $\eta_{\log a}(M)$, and $\sigma_{\log a}(M)$.

We plot the values of these parameters as a function of M and show each of the best-fit models for each parameter in Figure 9. Further, we summarize the best-fit models in Table 2. We conduct the fitting of the slopes of the mass-ratio distribution, $\gamma_c(M)$ and $\gamma_w(M)$, as follows. Duchêne & Kraus (2013) derived the slope of the mass-ratio distribution for companions of primary stars by fitting the mass-ratio distributions to a power law in the region of $0.1 < q < 1$. They derived the slope γ using their full sample within $0.1 < q < 1$, and they also determined the power-law exponents for close (γ_c) and wide (γ_w) binaries with semimajor axis logarithms that are smaller and larger than the mean value $\eta_{\log a}$, respectively. We show the values of γ, γ_c, and γ_w, based on the work of Duchêne & Kraus (2013), as a function of M as the black, red, and blue dots in the top-right panel in Figure 9, respectively. We do not plot γ_c and γ_w values for $M \leqslant 0.2\, M_\odot$, because Duchêne & Kraus (2013) reported only γ and not γ_c or γ_w in this mass range. Consequently, we use the γ values represented by the black dots at low masses when fitting $\gamma_c(M)$ (the red dashed line) and $\gamma_w(M)$ (the blue dashed line). We use $\gamma = 0.42$ at $0.08\, M_\odot$ in our fit to determine $\gamma_c(M)$. To determine $\gamma_w(M)$, we assume that $\gamma_w = \gamma$ for $M < 0.3\, M_\odot$ because this condition is true when $M > 0.3\, M_\odot$. Then, we conduct a linear fitting of $\gamma(M)$ in the region $M < 0.3\, M_\odot$, and we use the result for $\gamma_w(M)$ at $M < 0.34\, M_\odot$ (the sloping part of the blue dashed line). For $M \geqslant 0.34\, M_\odot$, γ_w seems to be

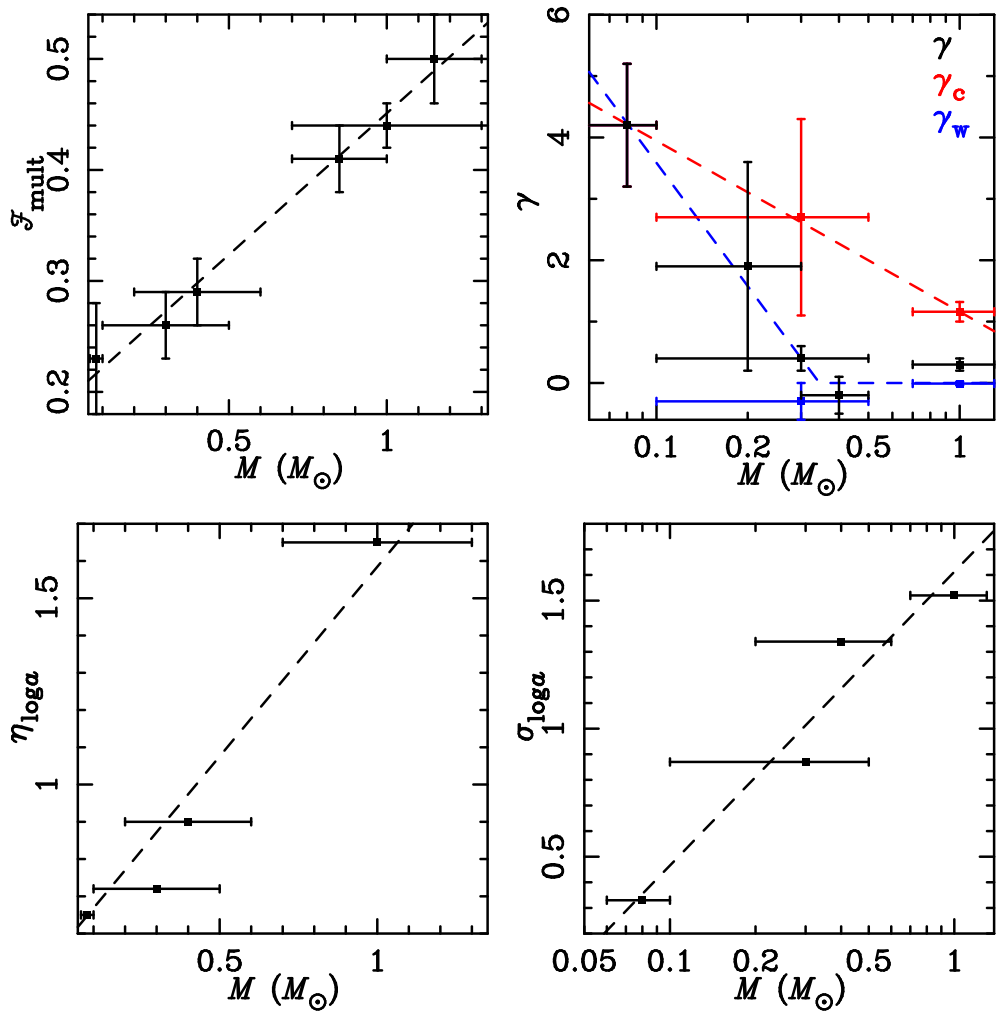

Figure 9. Parameters for the description of the binary distribution for a non-secondary star as functions of the star mass M. The multiplicity fraction $\mathcal{F}_{\rm mult}$, the slope of the mass-ratio distribution γ, and the mean and standard deviation of the log semimajor axis distribution, $\eta_{\log a}$ and $\sigma_{\log a}$, respectively, are plotted. The data are from Duchêne & Kraus (2013), but the values of Ward-Duong et al. (2015) are added at $M = 0.4 \pm 0.2\,M_\odot$ for the three parameters $\mathcal{F}_{\rm mult}$, $\eta_{\log a}$, and $\sigma_{\log a}$. In the top-right panel, the red (γ_c), blue (γ_w), and black (γ) points with error bars indicate the slopes of the mass-ratio distribution for close ($\log a < \eta_{\log a}$), wide ($\log a \geqslant \eta_{\log a}$), and all binary systems, respectively. The dashed lines indicate our best linear fit models.

approximately constant; hence, we use $\gamma_w = 0$ for this mass range (indicated by the flat part of the blue dashed line).

We note that these models simply attempt to provide a convenient description of the empirical data; they do not have any theoretical basis. We extrapolate these relations to mass M out of the region plotted in Figure 9, but such very high- or low-mass stars are too bright or too faint to contribute to the excess flux analyzed in this paper, respectively. Figure 10 shows examples of the binary distribution for a non-secondary star using these models.

4.4.3. Full Binary Distribution

Figure 11 shows the probabilities that an arbitrary star is a single ($P_{\rm single}(M)$), primary ($P_{\rm prim}(M)$), and secondary ($P_{\rm second}(M)$) star, given by Equations (26)–(28), where the binary distributions for a non-secondary star described in Section 4.4.2 are applied. For $\Phi_{\rm PD}(M)$ for the plot, we just apply a cutoff at $1.5\,M_\odot$ to the IMF given by Equation (14). This simplified cutoff is used only for this plot, and we apply the cutoff with the age distribution described in Section 4.2.1 to our Bayesian analysis. Because $\mathcal{F}_{\rm mult}(M)$ increases with M, $P_{\rm prim}(M) \propto \mathcal{F}_{\rm mult}(M)$ also increases. Meanwhile, $P_{\rm second}(M)$ decreases as the mass M approaches the upper cutoff mass ($1.5\,M_\odot$ in this plot) in the stellar mass function.

We show the binary distribution for arbitrary stars, $f_{\rm arb}(q, a|M)$, in Equation (25), projected to the mass ratio and semimajor axes in Figure 12 as dotted lines. Recall that $f_{\rm arb}(q, a|M)$ depends on the arbitrary star mass M that is usually given by a probability distribution. The two panels to the far left in Figure 12(a) show the prior probability distributions of the source mass M_S and the lens mass M_L for event M16227, where M_S is calculated by applying the mass–luminosity relation to the observed source mag $H_{S,\rm obs}$ (see details in Section 4.5), and M_L is given by the prior PDF $f'_{\rm pri}(M_L, D_L, D_S, v_{\rm t})$ described in Section 4.2. We combine the mass and binary distributions through a Monte Carlo simulation that selects the $M_*(M_S$ or $M_L)$ value randomly from its probability distribution and then picks a combination of (q_i, a_i) (i = SC for $M_* = M_S$ or i = LC for $M_* = M_L$) randomly from the appropriate $f_{\rm arb}(q_i, a_i|M_*)$ distribution to obtain the dotted lines in the panels labeled q_i and $\log a_i$. Figure 12(b) shows these distributions for event M11293 in a similar manner. We

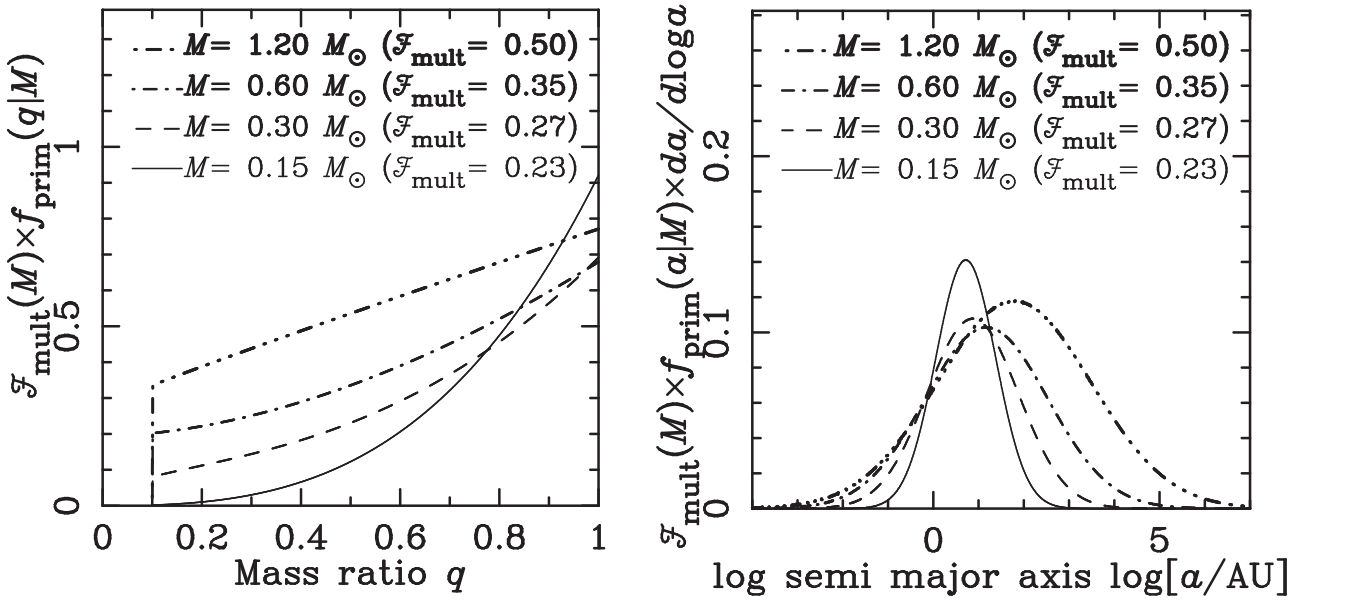

Figure 10. Binary distributions for non-secondary stars of mass $M = 0.15\,M_\odot$, $0.30\,M_\odot$, $0.60\,M_\odot$, and $1.20\,M_\odot$. Left: mass-ratio distributions $f_{\rm prim}(q|M) = \int_a f_{\rm prim}(q, a|M)\,da$. Right: logarithm of semimajor axis distributions $f_{\rm prim}(a|M) \times (da/d\log a) = \int_q f_{\rm prim}(q, a|M)\,dq \times (da/d\log a)$, where $(da/d\log a)$ is required for the change of variable from a to $\log a$. The total area of each distribution in both panels is normalized by the multiplicity fraction $\mathcal{F}_{\rm mult}(M)$.

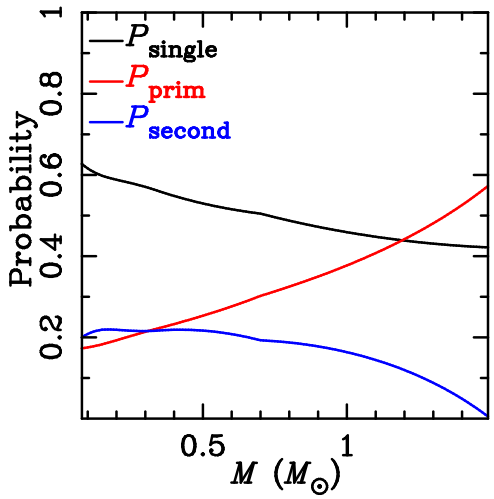

Figure 11. Probabilities of an arbitrary star with mass M being a single star, $P_{\rm single}(M)$; a primary star, $P_{\rm prim}(M)$; and a secondary star, $P_{\rm second}(M)$, where $P_{\rm single}(M) + P_{\rm prim}(M) + P_{\rm second}(M) = 1$. The black, red, and blue lines represent $P_{\rm single}(M)$, $P_{\rm prim}(M)$, and $P_{\rm second}(M)$, respectively. The mass function $\Phi_{\rm PD}(M)$ with a cutoff at $1.5\,M_\odot$ is used for the calculation.

refer to these distributions in the dotted lines as the full binary distribution to distinguish them from the undetected binary distribution in the solid lines in the same panels described in Section 4.4.4.

Equation (25) shows $f_{\rm arb}(q, a|M) = P_{\rm prim}(M) f_{\rm prim}(q, a|M)$ with q in the range $0 < q < 1$; hence, the shapes of the q_i and a_i distributions, shown in Figure 12, are similar to that of $f_{\rm prim}(q, a|M)$ given by Equation (29) and plotted in Figure 10. These would be power-law and log-normal distributions for q_i and a_i, respectively. However, these shapes are somewhat distorted by the contribution from $q > 1$ and by the M distributions that take various M values instead of a fixed M value. For $q > 1$, the $q_{\rm SC}$ and $q_{\rm LC}$ distributions follow the third term of Equation (25), where the $\Phi_{\rm PD}(qM)$ and q^{-1} factors decrease the probability rapidly as q increases because $\Phi_{\rm IMF}(qM) \propto q^{-2}$ for $qM > 0.7\,M_\odot$ as seen in Equation (14).

While we know that the lens and source star exist for each event, the existence of a source or lens companion is not certain. Therefore, we use $P_{\rm exist}$ to denote the probability that a lens or source companion exists, and for consistency in notation, we use $P_{\rm exist} = 1$ for the lens and source stars. For the full binary distributions in the dotted curves in Figure 12, the probability of $1 - P_{\rm exist}$ for the source and lens companions corresponds to $P_{\rm single}(M_*)$ with $M_* = M_S$ or $M_* = M_L$, respectively, as given in the first term in Equation (25).

4.4.4. Undetected Binary Distribution

As described in Section 3.1.1, we use the undetected binary distribution, which is the combination of the full binary distribution and the detection efficiency, to simulate the source and lens companions in the Monte Carlo simulation to derive the prior PDF $f_{\rm pri}(F_L, F_{\rm SC}, F_{\rm LC})$. Some companions are so close to the source or lens star that they would affect the light curve in ways that are inconsistent with observations. Hence, unlike the case of ambient stars, we must include a minimum allowable separation in addition to the maximum separation to consider the detection efficiencies for the source and lens companions. We denote the angular separations corresponding to the minimum (or close) separation limit by $\phi_{\rm close,SC}$ for the source companion and $\phi_{\rm close,LC}$ for the lens companion, while we use the same value of $\phi_{\rm wide}$ as that in Table 3 for the wide limits of the unresolvable region of these objects. This is equivalent to adopting a detection efficiency of

$$\epsilon_i = \Theta[(\phi - \phi_{\rm wide})(\phi - \phi_{{\rm close},i})] \quad (i = {\rm SC\ or\ LC}) \qquad (31)$$

for the companion to the source or lens located at angular separation ϕ from the centroid of the target.

Following Batista et al. (2014), we adopt $\theta_{\rm E}/4$ as $\phi_{\rm close,SC}$, and we derive $\phi_{\rm close,LC}$ using the inequality $w_{\rm LC} < u_0$ as the

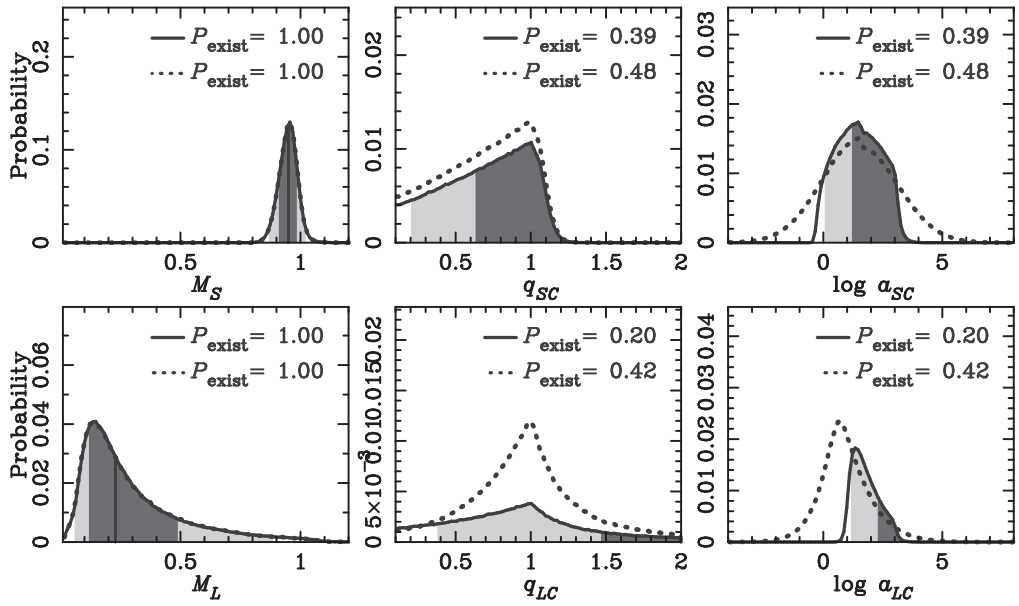

(a)

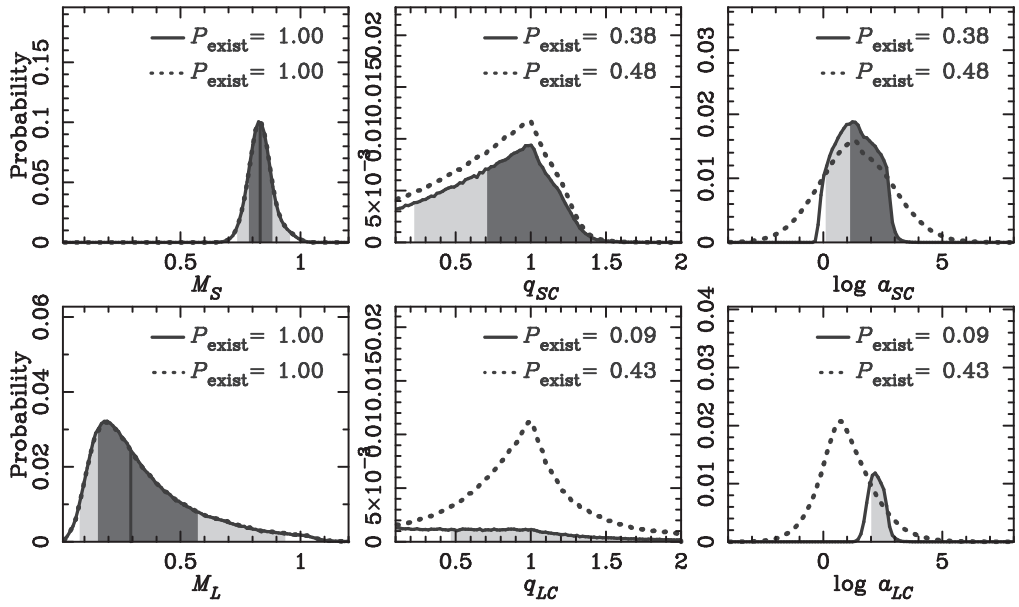

(b)

Figure 12. The undetected (solid) and full (dotted) binary distributions calculated using parameters of (a) M16227 ($\phi_{\rm wide} = 148$ mas, $\theta_{\rm E,obs} = 0.23$ mas, $u_{0,\rm obs} = 0.08$) and (b) M11293 ($\phi_{\rm wide} = 60$ mas, $\theta_{\rm E,obs} = 0.26$ mas, $u_{0,\rm obs} = 0.0035$). The undetected binary distribution is part of the full binary distribution $f_{\rm arb}\,(q_i,\, a_i|M_*)$ (i = SC for $M_* = M_S$ and i = LC for $M_* = M_L$) that gives the detection efficiency $\epsilon_i = 0$. See Section 4.4.4 for the details. The $P_{\rm exist}$ values denote the probability that the corresponding object exists. For the undetected distributions, the borders between different colors indicate the 2.3rd, 16th, 84th, and 97.7th percentiles from left to right. The thick vertical lines between the 16th and 84th percentiles indicate the median. Some percentiles are out of the plot in the case of $P_{\rm exist} < 1$.

condition for an unresolvable lens companion, where $w_{\rm LC}$ is the size of the central caustic created by the hypothetical companion to the lens. We use the analytic formula $w_{\rm LC} = 4q_{\rm LC}/(s_{\rm LC} - s_{\rm LC}^{-1})^2$, where $s_{\rm LC}$ is the projected separation between the lens and the companion in units of the angular Einstein radius (Chung et al. 2005). Although this formula is an approximate one that was derived for planetary mass ratios, $q_{\rm LC} \ll 1$, we find that it works moderately well even for stellar mass-ratio companions, as discussed in Section 10.3.1. With this analytic formula for $w_{\rm LC}$, the inequality $w_{\rm LC} < u_0$ has two different unresolvable regions of $s_{\rm LC}$ as its solutions:

$$s_{\rm LC} < \sqrt{\frac{q_{\rm LC}}{u_0} + 1} - \sqrt{\frac{q_{\rm LC}}{u_0}}, \tag{32}$$

$$s_{\rm LC} > \sqrt{\frac{q_{\rm LC}}{u_0} + 1} + \sqrt{\frac{q_{\rm LC}}{u_0}}. \tag{33}$$

A companion in the former unresolvable region corresponds to the case of a close-in binary system whose total mass is M_L, which we ignored in point (ii) at the beginning of Section 4.4 for simplicity. This means that when a companion that satisfies Equation (32) is selected in our Monte Carlo simulation shown in Figure 1, then we treat it as a resolvable companion, and such a scenario is rejected in our simulation. Considering this region carefully is important for studying possible circumbinary planetary systems such as OGLE-2007-BLG-349L(AB)c (Bennett et al. 2016); however, this is beyond the scope of this study and it negligibly changes the derived lens properties because the probability of the lens companion in this region is small. In summary, we decide to use

$$\phi_{\rm close,SC} = \theta_{\rm E}/4 \tag{34}$$

$$\phi_{\rm close,LC} = s_{\rm close,LC}\ \theta_{\rm E}, \tag{35}$$

where $s_{\rm close,LC} \equiv \sqrt{q_{\rm LC}/u_0 + 1} + \sqrt{q_{\rm LC}/u_0}$. These decisions are summarized in Table 2.

With the detection efficiencies $\epsilon_{\rm SC}$ and $\epsilon_{\rm LC}$, we calculate the undetected binary distribution as follows, which is also described in the left box in Figure 1. In each trial of the Monte Carlo simulation, we have a combination of ($q_{\rm SC}$, $a_{\rm SC}$) and ($q_{\rm LC}$, $a_{\rm LC}$), which are randomly selected from the full binary distributions of $f_{\rm arb}(q_{\rm SC}, a_{\rm SC}|M_S)$ and $f_{\rm arb}(q_{\rm LC}, a_{\rm LC}|M_L)$, respectively. Using a probability distribution $p(a_\perp) = a_\perp/a^2(1 - (a_\perp/a)^2)^{-1/2}$ (Gould & Loeb 1992) for the projection from a three-dimensional physical distance a to a projected distance in the sky, $a_\perp$, we randomly obtain the physical projected separations $a_{\rm SC,\perp}$ and $a_{\rm LC,\perp}$ from $a_{\rm SC}$ and $a_{\rm LC}$, respectively. We simulate the undetected binary distribution by accepting a combination of parameters that satisfies both $\epsilon_{\rm SC} = 0$ and $\epsilon_{\rm LC} = 0$, i.e., when both of the generated $a_{\rm SC,\perp}$ and $a_{\rm LC,\perp}$ are located in the corresponding unresolvable regions, $\phi_{\rm close,SC} < a_{\rm SC,\perp}/D_S < \phi_{\rm wide}$ and $\phi_{\rm close,LC} < a_{\rm LC,\perp}/D_L < \phi_{\rm wide}$, respectively.

The solid lines in Figures 12(a) and (b) represent the undetected binary distributions for M16227 and M11293, respectively. As shown in the log a_i distributions, the shape of the undetected distributions of the semimajor axis is the same as that of the full distribution but with the edges on both sides removed by considering them as detectable. The borders between the colors of the shaded areas represent the 2.3rd, 16th, 84th, and 97.7th percentiles from left to right, and the thick vertical line represents the median. The probability that each object exists is shown in the top-right panel as $P_{\rm exist}$. The bins corresponding to (q_i, a_i) = (0, 0), i.e., cases of a single star, are not shown, and the integrated areas of the plotted regions are thus the same as the $P_{\rm exist}$ values. Therefore, some percentiles are not shown in the panels with $P_{\rm exist} < 1$. For example, in the distributions of $q_{\rm SC}$ and $\log a_{\rm SC}$ in Figure 12(a) where the $P_{\rm exist}$ value is 39%, which is larger than 16% but smaller than 50%, the 2.3rd and 16th percentiles are shown, but the median and the 84th and 97.7th percentiles are not shown.

The relation between the $P_{\rm exist}$ values of the undetected and full distributions for the companion to the source or lens is

$$P_{\rm exist,undet,\it i} = \frac{P_{\rm exist,full,\it i} - P_{\rm det,\it i}}{1 - P_{\rm det,\it i}}, \tag{36}$$

where $P_{\rm exist,undet,\it i}$ and $P_{\rm exist,full,\it i}$ are the $P_{\rm exist}$ values for the source companion (i = SC) or lens companion (i = LC) in the undetected (solid line) and full (dotted line) binary distributions, respectively. Further, $P_{\rm det,\it i}$ is the fraction of detectable companions to the source or lens in the full binary distribution, where its projected separation $a_{i,\perp}$ does not satisfy the condition $\phi_{{\rm close},i} < a_{i,\perp}/D_* < \phi_{\rm wide}$ ($D_* = D_S$ for i = SC and $D_* = D_L$ for i = LC). This fraction of $P_{\rm det,\it i}$ is subtracted not only from the numerator but also from the denominator in Equation (36), which causes the value of $P_{\rm exist,undet,\it i}$ to be higher than just the subtracted value of $P_{\rm exist,full,\it i} - P_{\rm det,\it i}$. This is also why there is a part where the probability of the solid line is higher than the probability of the dotted line in the $\log a_i$ distribution. In Section 10, we compare these $P_{\rm det,\it i}$ values with the binary fractions around source or lens stars actually detected in planetary microlensing events.

4.5. Lens Flux and Source and Lens Companion Flux Priors

Now that we have the joint prior PDF of M_L, D_L, D_S, and v_t, $f'_{\rm pri}(M_L, D_L, D_S, v_{\rm t})$, the mass–luminosity relation, $\mathcal{M}_H(M)$, and the undetected binary distribution, we are equipped to calculate the joint prior PDF for the fluxes of the lens and companions to the source and lens stars, $f_{\rm pri}(F_L, F_{\rm SC}, F_{\rm LC})$, using the Monte Carlo method summarized in Section 3.1.1 and Figure 1.

Given the lens mass M_L, source companion mass $M_{\rm SC}$, and lens companion mass $M_{\rm LC}$, we can convert them into the apparent magnitudes in the H band through

$$H_L = \mathcal{M}_{H,L}(M_L) + {\rm DM}_L + A_{H,L}, \tag{37}$$

$$H_{\rm SC} = \mathcal{M}_{H,\rm SC}(M_{\rm SC}) + {\rm DM}_S + A_{H,S}, \tag{38}$$

$$H_{\rm LC} = \mathcal{M}_{H,\rm LC}(M_{\rm LC}) + {\rm DM}_L + A_{H,L}, \tag{39}$$

where ${\rm DM}_i$ ($i = L, S$) is the distance modulus corresponding to the distance of D_i, and $\mathcal{M}_{H,i}$ is the absolute H-band magnitude for star i. To evaluate the amount of extinction, we use the formula $A_{H,i} = (1 - e^{-D_i/h_{\rm dust}})/(1 - e^{-D_{\rm rc}/h_{\rm dust}})\ A_{H,\rm rc}$, following Bennett et al. (2015), where $h_{\rm dust} = (0.1\ {\rm kpc})/\sin|b|$ is the dust scale length toward the galactic bulge at galactic latitude b. The average distance to the red clump stars at the event position, $D_{\rm rc}$, also corresponds to the distance modulus ${\rm DM}_{\rm rc}$. Because we have a combination of M_L, D_L, and D_S, which are randomly extracted from $f'_{\rm pri}(M_L, D_L, D_S, v_{\rm t})$, we can immediately calculate H_L, ${\rm DM}_i$, and $A_{H,i}$ with these formulae in each trial of our Monte Carlo simulation.

The remaining uncertain values in Equations (37)–(39) are $M_{\rm SC}$ and $M_{\rm LC}$. We calculate these values using the undetected binary distribution described in Section 4.4.4. At this point, the lens star that we consider is characterized by its mass M_L whereas the source star is characterized by its H-band magnitude; hence, we must calculate the source mass $M_S = M_S(\mathcal{M}_{H,S})$ from $\mathcal{M}_{H,S} = H_{S,\rm obs} - A_{H,S} - {\rm DM}_S$ and the mass–luminosity relation. Then, we randomly select the source and lens companion parameters ($q_{\rm SC}$, $a_{\rm SC}$ and $q_{\rm LC}$, $a_{\rm LC}$) from the $f_{\rm arb}(q_{\rm SC}, a_{\rm SC}|M_S)$ and $f_{\rm arb}(q_{\rm LC}, a_{\rm LC}|M_L)$ distributions. Recall that the binary distribution $f_{\rm arb}(q, a|M)$ returns (q, a) = (0, 0) with the probability of $P_{\rm single}(M)$ in Equation (26), which implies that the star in question has no companion. By accepting the binary parameters that satisfy $\epsilon_{\rm SC} = 0$ and $\epsilon_{\rm LC} = 0$, we have the source companion mass $M_{\rm SC} = q_{\rm SC} M_S$ and the lens companion mass $M_{\rm LC} = q_{\rm LC} M_L$, as described in Section 4.4.4 and Figure 1.

We calculate and plot the joint prior PDF $f_{\rm pri}(F_L, F_{\rm SC}, F_{\rm LC})$ in magnitude for each event in the bottom-right panel of each (a) component of Figures 2–6. The solid lines in red, green, and purple correspond to the prior probability distributions of H_L, $H_{\rm SC}$, and $H_{\rm LC}$, respectively. We plot them along a one-dimensional axis for clarity; however, we note that they are from a joint probability distribution and are correlated with each other. The correlations between $H_{\rm SC}$ and the other two parameters are weak, whereas the correlation between H_L and $H_{\rm LC}$ is moderately strong because the mass of a lens companion is given by $M_{\rm LC} = q_{\rm LC} M_L \propto M_L$ and the $q_{\rm LC}$ distribution depends on the lens mass M_L. As in the case of Figure 12, we do not plot bins corresponding to $(q, a) = (0, 0)$, the case of no companion; instead, we show the probability that the companion exists (i.e., the total area of the shown distribution) as $P_{\rm exist}$ in the parentheses in each color.

5. Application and Results

We apply our method to M16227, M08310, M11293, O120563, and O120950. We calculate the prior PDF of the four possible origins of the flux, $f_{\rm pri}(F_L, F_{\rm amb}, F_{\rm SC}, F_{\rm LC})$, for each event by repeating the procedure in the left box in Figure 1 using the models listed in Table 2 and the parameters for each event listed in Table 3. Then, we calculate the posterior PDF $f_{\rm post}(F_L, F_{\rm amb}, F_{\rm SC}, F_{\rm LC}|F_{\rm excess} = F_{\rm ex,obs})$ for each event by extracting combinations of the parameters for which the excess flux value is consistent with the observed value for each event from the prior PDF. This corresponds to the procedure shown in the right box in Figure 1. The (a) and (b) components of Figures 2–6 show the prior and posterior probability distributions, respectively, for the lens mass and distance (left panels), the magnitude of each contributor (bottom-right panels), and the magnitude of excess flux (top-right panels). The horizontal axes are divided into 100 bins, and the probability values integrated within a bin are indicated along the vertical axes in each panel. We plot magnitude distributions up to ∼24 mag in the bottom-right and top-right panels because the H-band Zoccali et al. (2003) LF covers up to $H_0 = 23.5$ mag, where H_0 is an extinction-free magnitude. Note that our results of the posterior probabilities are negligibly affected by the unconsidered fainter ambient stars, as discussed in Section 4.1.1.

5.1. How to Find Possible Origins of the Observed Excess

Possible origins of the observed excess flux can be found in all three panels in Figures 2–6 as described below. In each of the left panels in Figures 2–6, we plot part of the accepted combinations of mass and distance of the four contributors on the mass–distance plane, where the number of dots in each color is proportional to the $P_{\rm exist}$ values of each contributor. We plot the distance to the ambient star, $D_{\rm amb}$, and its mass, $M_{\rm amb}$, by assuming that they are located at the source distance in each step of the Monte Carlo simulation. This is a crude assumption just for this plot and has no effect on our result. Parts where a specific color is densely plotted indicate a high probability that the corresponding object has the mass and distance of the part. In the same plane, we also show the mass–distance relations from $\theta_{E,\rm obs}$ or $\pi_{E,\rm obs}$, $H_{\rm ex,obs}$, and H_L. Note that the value of H_L is not the observed quantity; it is from the probability distribution obtained by our calculation. The mass–distance relation from $H_{\rm ex,obs}$ is plotted by assuming that $H_{\rm ex,obs}$ comes from only one star. This indicates that a contributor that has many dots on the $H_{\rm ex,obs}$ mass–distance relation curve is likely to be an origin of the observed excess flux. This consideration is basically applicable to both (a) and (b) panels. For example, we can see many green dots and fewer red dots on the $H_{\rm ex,obs}$ curve in the left panels of both Figures 3(a) and (b), which indicates that the most likely source of the excess flux is the source companion rather than the lens.

The origin of the excess flux can be discussed similarly with each of the magnitude distributions in the top-right panels and bottom-right panels in Figures 2–6. The bottom-right panel of each figure shows the prior or posterior probability distributions of H_i ($i = L$, amb, SC, LC), where we can find which contributor is likely to be the main origin of the observed excess flux by comparing the $P(H_i)$ values in the gray shaded region of $H_{\rm ex,obs}$. We note that the ratio among probabilities that a contributor has a brightness of $H_{\rm ex,obs}$, $P(H_i = H_{\rm ex,obs})/P(H_j = H_{\rm ex,obs})$ $(i \neq j)$, in the prior PDF does not equal the ratio in its posterior PDF. This is because the correlations among the parameters become stronger in the posterior PDF owing to the requirement of $F_{\rm excess}(\equiv F_L + F_{\rm amb} + F_{\rm SC} + F_{\rm LC}) = F_{\rm ex,obs}$ compared to the prior PDF, where the parameters are nearly independent of each other except for the combination of H_L and $H_{\rm LC}$.

The thick black line in the top-right panel in each of Figures 2–6 represents the $H_{\rm excess}$ probability distribution. In the same panel, we divide the $H_{\rm excess}$ probability distribution into four color areas to visually clarify the average contribution from each contributor to the excess flux. Let the fraction of each contributor's flux to the excess flux be $f_i \equiv F_i/F_{\rm excess}$ ($i = L$, amb, SC, LC). Then, the fraction of the vertical width of each color region to the height of $P(H_{\rm excess})$ at a given $H_{\rm excess}$ value equals the mean of f_i, where the mean is taken in scenarios in the Monte Carlo simulation whose excess flux corresponds to the magnitude bin of the given $H_{\rm excess}$. In the top-right panel of the (b) components, we show another mean value of f_i, which is taken in all the accepted scenarios in the posterior calculation, as $\langle f_i \rangle$. This value corresponds to the area of each color in the same panel. Each $\langle f_i \rangle$ value indicates the average contribution of each contributor to the observed excess flux in various scenarios that are consistent with the observation. Note that these are just average contributions; hence, it does not mean that a scenario with the brightness corresponding to these fractions (i.e., a scenario with $F_i = \langle f_i \rangle F_{\rm excess}$) is highly likely. We can determine which object is likely to contribute significantly to the excess flux from this panel, i.e., a contributor whose color occupies a large area in the gray shaded region of $H_{\rm ex,obs}$ in the prior distribution, or a contributor whose $\langle f_i \rangle$ value is high in the posterior distribution.

5.2. Lens Properties Constrained by Excess Fluxes

Table 4 summarizes the lens mass, M_L, and the distance to the lens, D_L, obtained from the posterior PDF, as well as the planet mass $M_{\rm p} = q\, M_L/(1 + q)$ and the projected separation between the host star and the planet, $a_\perp = s\, D_L \theta_{\rm E}$, for each event, where the host-planet mass ratio q and the separation s are given by the discovery paper of each event. Because the events in consideration are all planetary events, we note that all the lens parameters listed in Table 4 depend on the unknown prior of the planet-hosting probability, which is assumed to be the same here regardless of the host star's property, but is, in fact, probably different depending on the property. We further

Table 4
Lens Properties Calculated from the Posterior Probability Distributions Assuming $\alpha = 0$

Event	M16227	M08310	M11293	O120563	O120950
References	1	2, 7	3, 4	5	6, 8
This work ($\alpha = 0$)					
M_L ($M_\odot$)	$0.28^{+0.24}_{-0.15}$	$0.14^{+0.27}_{-0.07}$	$0.41^{+0.35}_{-0.23}$	0.37 ± 0.12	$0.57^{+0.11}_{-0.20}$
M_p	$2.7^{+2.4}_{-1.4}$ $M_{\rm Jup}$	14^{+28}_{-7} $M_\oplus$	$2.3^{+1.9}_{-1.3}$ $M_{\rm Jup}$	0.43 ± 0.13 $M_{\rm Jup}$	38^{+10}_{-14} $M_\oplus$
D_L (kpc)	$6.6^{+1.0}_{-0.9}$	$7.3^{+1.2}_{-1.1}$	$7.3^{+0.9}_{-1.0}$	1.6 ± 0.5	$2.9^{+1.2}_{-0.7}$
$a_\perp$ (au)	1.42 ± 0.21	$1.16^{+0.23}_{-0.20}$	...	...	$2.62^{+0.53}_{-0.56}$
$a_{\perp,\rm close}$ (au)[a]	...	...	1.04 ± 0.16	$0.82^{+0.23}_{-0.24}$	...
$a_{\perp,\rm wide}$ (au)[a]	...	...	$3.49^{+0.52}_{-0.54}$	$4.82^{+1.35}_{-1.39}$	...
$P(f_L > 0.1)$[b]	74.9%	41.9%	58.0%	99.99%	86.1%
$P(f_L > 0.5)$[b]	37.8%	25.2%	31.3%	99.94%	70.5%
$P(f_L > 0.9)$[b]	21.8%	19.3%	21.9%	89.7%	52.3%
$H_L - H_{\rm excess}$ (mag)[c]	$1.30^{+1.72}_{-1.30}$	$3.12^{+2.97}_{-3.12}$	$2.12^{+1.46}_{-2.11}$	$0.005^{+0.068}_{-0.004}$	$0.08^{+2.04}_{-0.08}$
Previous work					
M_L ($M_\odot$)	0.63 ± 0.08[d]	0.67 ± 0.14	0.86 ± 0.06	$0.34^{+0.12}_{-0.20}$	$0.56^{+0.12}_{-0.16}$
D_L (kpc)	7.4 ± 1.1[d]	$8.3^{+1.5}_{-1.2}$[e]	7.72 ± 0.44	$1.3^{+0.6}_{-0.8}$	$3.0^{+0.8}_{-1.1}$
Result w/HST					
M_L ($M_\odot$)	...	$0.21^{+0.21}_{-0.09}$	...	...	0.58 ± 0.04
D_L (kpc)	...	7.7 ± 1.1	...	...	2.19 ± 0.23

Notes. Values given in the form of the median with 1σ uncertainty.
[a] For events with degenerate models with largely different s values, we give the projected separation value separately as $a_{\perp,\rm close}$ and $a_{\perp,\rm wide}$.
[b] Probabilities that the fraction of the lens flux to the excess flux, $f_L \equiv F_L/F_{\rm excess}$, is larger than the indicated values.
[c] Difference in magnitude, $H_L - H_{\rm excess} = -2.5 \log f_L$.
[d] Assumed $H_L = H_{\rm ex,obs}$. The values do not come from Koshimoto et al. (2017a).
[e] Assumed $D_S = 8.6^{+1.5}_{-1.2}$ kpc, which is the same source distance that we used. Janczak et al. (2010) just provided the $D_S - D_L$ value as ~0.3 kpc.
References. (1) Koshimoto et al. (2017a), (2) Janczak et al. (2010), (3) Yee et al. (2012), (4) Batista et al. (2014), (5) Fukui et al. (2015), (6) Koshimoto et al. (2017b), (7) Bhattacharya et al. (2017), (8) Bhattacharya et al. (2018).

discuss this point in Section 8 and show that the change in the median value of M_L is within the 1σ uncertainty shown in Table 4 for all the events if we consider a different assumption for it.

5.2.1. Treatment for Degenerate Solutions

All the events to which we applied our method, except for M16227, have two solutions of the close and wide models.

We combined the probability distributions of the projected separation $a_\perp$ calculated from each solution for events where both close and wide models have similar s values, i.e., for M08310, which has $s = 1.085$ (wide model) and $s = 0.927$ (close model), and O120950, which has $s = 1.004$ (wide model) and $s = 0.895$ (close model). We combine the two probability distributions with no weight, although there are χ^2 differences between the close and wide models, i.e., $\Delta\chi^2 = 2.06$ for M08310 and $\Delta\chi^2 = 1.5$ for O120950. This is because the photometry data for the densest field, such as the galactic bulge, generally suffer from systematic errors; thus, we conservatively treated the two solutions equally with χ^2 differences less than ~2. Note that the relative difference of s between the two solutions are 15% for M08310 and 11% for O120950, and these are less than the width of the 1σ confidence interval of the Einstein radius $R_{\rm E} = D_L\theta_{\rm E}$ for the two events, i.e., 17% and 21%, respectively. Therefore, any treatment of the weight between the two solutions negligibly affects the probability distribution of $a_\perp = s\ R_{\rm E}$ because the uncertainty of $R_{\rm E}$ is dominant.

Meanwhile, we show the two values separately as $a_{\perp,\rm close}$ and $a_{\perp,\rm wide}$ for events where the two s values are largely separated, i.e., for M11293 and O120563.

5.2.2. Comparison with Previous Studies

For comparison, we show the values of the lens mass and the distance to the lens presented in the original paper for each event in the same table. We also plot them on the mass–distance plane of each posterior distribution in Figures 2(b)–6(b) using black dots with error bars,[8] and we plot our results using red dots with error bars. Note that lens properties calculated assuming $H_L = H_{\rm ex,obs}$, which is a common assumption in most of the previous studies, are shown for M16227 instead of the values in the original paper because we presented the results of this method for the event previously in Koshimoto et al. (2017a).

In Figures 3(b) and 6(b), we additionally plot recent results using HST and Keck follow-up observations by Bhattacharya et al. (2017, 2018) on M08310 and O120950 in light-blue dots, respectively. The two observations were conducted after the excess measurements used in this analysis, when the lens stars were sufficiently separated from the source stars so that the lens

[8] In Figure 4(b), the black dot is slightly above even the mass–distance relation of $H_{\rm ex,obs}$ because of the difference in the $A_{H,\rm rc}$ value used. Whereas we use $A_{H,\rm rc} = 0.47 \pm 0.10$ from the extinction law of Nishiyama et al. (2009), they used a combination of $A_{H,\rm rc} = 0.65 \pm 0.12$ from the extinction law of Cardelli et al. (1989) and the value from Nishiyama et al. (2009). We do not combine them because Nataf et al. (2016) reported that the extinction law toward the galactic bulge is clearly different from the law of Cardelli et al. (1989).

stars were resolved. Notably, our results of $M_L = 0.15^{+0.29}_{-0.08}\,M_\odot$ and $D_L = 7.2 \pm 1.1$ kpc for M08310 and $M_L = 0.57^{+0.11}_{-0.20}\,M_\odot$ and $D_L = 2.62^{+0.53}_{-0.56}$ kpc for O120950 are both consistent with $M_L = 0.21^{+0.21}_{-0.09}\,M_\odot$ and $D_L = 7.7 \pm 1.1$ kpc obtained by Bhattacharya et al. (2017) and $M_L = 0.58 \pm 0.04\,M_\odot$ and $D_L = 2.19 \pm 0.23$ kpc obtained by Bhattacharya et al. (2018), respectively, without their HST or Keck data.

Our lens mass estimates for M16227 ($M_L = 0.28^{+0.24}_{-0.15}\,M_\odot$), M08310 ($M_L = 0.14^{+0.27}_{-0.07}\,M_\odot$), and M11293 ($M_L = 0.41^{+0.35}_{-0.23}\,M_\odot$) are less massive and have larger uncertainties than the results reported in previous studies or the results with the assumption of $H_L = H_{\rm ex,obs}$, i.e., $M_L = 0.63 \pm 0.08\,M_\odot$, $M_L = 0.67 \pm 0.14\,M_\odot$, and $M_L = 0.86 \pm 0.06\,M_\odot$, respectively. Meanwhile, our results for O120563 ($M_L = 0.37 \pm 0.12\,M_\odot$) and O120950 ($M_L = 0.57^{+0.11}_{-0.20}\,M_\odot$) are similar to the results of the previous discovery papers, i.e., $M_L = 0.34^{+0.12}_{-0.20}\,M_\odot$ and $M_L = 0.56^{+0.12}_{-0.16}\,M_\odot$, respectively.

Because most of the previous studies derived the lens mass assuming $H_L = H_{\rm ex,obs}$, whether our value is similar to theirs depends on the probability of the lens being the main origin of the excess flux. If this probability is low, the probability of the lens flux being fainter than the excess flux increases, which makes the lens mass estimate less massive. In such a case, there is no inconsistency regardless of how much fainter the lens is than the excess flux. Therefore, the posterior distribution of H_L takes the shape of the prior distribution for the faint region, which results in a large uncertainty of the lens mass estimate.

5.2.3. Probability that Lens Flux Accounts for a Certain Fraction of Excess Flux

For M16227, M08310, and M11293, the probabilities of the lens being the main origin of the excess flux are smaller than or comparable to the probabilities of other contaminants, as seen in the bottom-right panels in Figures 2–4. This is also known from the values $P(f_L > 0.1)$, $P(f_L > 0.5)$, and $P(f_L > 0.9)$ shown in Table 4, which are the probabilities of the fraction of the lens flux to the excess flux, $f_L = F_L/F_{\rm excess}$, being larger than 0.1, 0.5, and 0.9, respectively. The fraction f_L is related to the difference of the magnitudes between the lens and the excess by $H_L - H_{\rm excess} = -2.5 \log f_L$, and these three probabilities are equivalent to the probabilities of $H_L - H_{\rm excess}$ being smaller than 2.5 mag, 0.75 mag, and 0.11 mag, respectively.

For example, the probabilities $P(f_L > 0.5)$ of M16227, M08310, and M11293 are 37.8%, 25.2%, and 31.3%, respectively. This indicates that the probabilities of $F_L \leqslant 0.5\,F_{\rm excess}$, or equivalently, the probabilities of $H_L - H_{\rm excess} \geqslant 0.75$ mag, are higher than 60% for these three events. Meanwhile, the probabilities of $P(f_L > 0.5)$ are 99.94% for O120563 and 70.5% for O120950, which indicates that large parts of the observed excess flux for these events are likely to come from the lens stars.

The median and 1σ confidence interval values of the difference of magnitudes $H_L - H_{\rm excess}$ are also shown in the same table. Because $H_L - H_{\rm excess}$ and f_L are in one-to-one correspondence, a median value of $H_L - H_{\rm excess}$ close to 0 mag together with its small 1σ range indicates a high probability that f_L is close to 1, i.e., a high probability of the lens being the origin of the excess flux, which results in a strong constraint on the lens properties. For M16227, M08310, and M11293, the 1σ ranges of $H_L - H_{\rm excess}$ are 3.02 mag, 6.09 mag, and 3.57 mag, respectively. By contrast, they are 0.07 mag and 2.12 mag for O120563 and O120950, respectively. The large 1σ ranges of $H_L - H_{\rm excess}$ for the former three events indicate much weaker constraints on their lens mass estimates compared to the estimates where $f_L = 1$ is assumed.

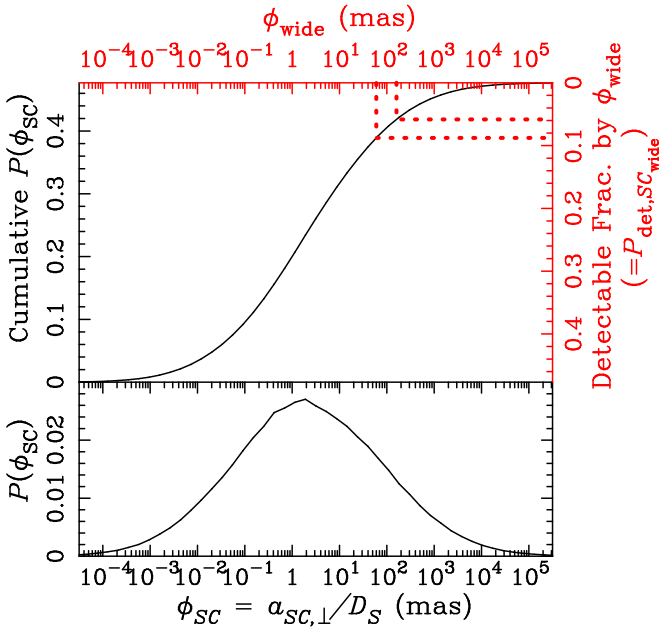

Figure 13. Probability distribution of the angular separation of a source companion, $\phi_{\rm SC} \equiv a_{\rm SC,\perp}/D_S$, in the full binary distribution of M16227 (bottom) and its cumulative distribution (top). The right axis of the top panel corresponds to the detectable fraction of a source companion located outside of the undetectable circle with the radius $\phi_{\rm wide}$. The two dotted red lines indicate the fraction of a source companion in $\phi_{\rm wide} = 60$ mas and $\phi_{\rm wide} = 160$ mas and their corresponding detectable fraction.

6. Interpretation of Results

We found that the probability of the lens being the main origin of the excess flux is not significant for M16227, M08310, and M11293, while it is significant for O120563 and O120950. In this section, we investigate the causes for the different probabilities among these five events. We find that when $\theta_{\rm E}$ is large or likely to be large, the lens is likely to be the main origin of the excess flux. Otherwise, the probability of a large contribution from other contaminants, especially from the source companion, cannot be ruled out.

6.1. Event with a Small Angular Einstein Radius $\theta_{\rm E}$

We find that the key parameter that determines whether we can impose a tight constraint on $H_L - H_{\rm excess}$ or on the lens properties is the angular Einstein radius $\theta_{\rm E}$ rather than the radius of the unresolvable circle, $\phi_{\rm wide}$, within which we have been considering all possible contamination scenarios. The bottom-right panels in Figures 2(b)–4(b) show high probabilities of ambient stars and the source companion being a possible origin of the observed excess for M16227 and M08310, and of the source companion being a possible origin of the observed excess for M11293, although they also show comparable probabilities for the lens star for all these events. Thus, the source companion is the main contaminant in all the events where we cannot impose a strong constraint on the lens property.

6.1.1. High Angular Resolution Negligibly Reduces the Probability of a Source Companion

To determine how these contaminants work, we compare the results of M16227 with $\phi_{\rm wide} = 148$ mas and the results of M11293 with $\phi_{\rm wide} = 60$ mas, which is $\sim$2.5 times smaller than the former value. A small $\phi_{\rm wide}$ value effectively reduces the probability of existence of ambient stars because the average number of ambient stars within a circle of radius $\phi_{\rm wide}$, $\lambda_{\rm amb}$, given by Equation (9), is proportional to $\phi^2_{\rm wide}$. The $P_{\rm exist}$ value for ambient stars in the prior distribution is 0.08 for M11293, while it is 0.39 for M16227, as shown in the bottom-right panels in Figures 4(a) and 2(a).

Meanwhile, the log-normal distribution is used as the semimajor axis distribution of the binary system as described in Section 4.4.2 and summarized in Table 2. Therefore, a $\phi_{\rm wide}$ value that is even $\sim$2.5 times smaller reduces the considered region of the semimajor axis by only $\sim$0.4 dex on the log scale and negligibly reduces the probability of existence of the source companion. This is seen in a comparison of the far-right value of the solid curves in the panel labeled $\log a_{\rm SC}$ in Figure 12(a) with that in Figure 12(b). Figure 13 shows this more clearly by plotting the distribution of $\phi_{\rm SC} \equiv a_{\rm SC,\perp}/D_S$, the angular separation of companions around the source star of M16227. The top panel shows the cumulative probability distribution of $\phi_{\rm SC}$ and, simultaneously, the detectable fraction of source companions with $\phi_{\rm wide}$ with the red axes. The two dotted red lines in the top panel indicate the detectable fractions by the maximum and minimum $\phi_{\rm wide}$ values in the five events, i.e., 160 and 60 mas. The difference between the two fractions of $\sim$3% is small relative to the remaining fraction. Figure 13 indicates that it is difficult to drastically reduce the probability of existence of the source companion with any realistic $\phi_{\rm wide}$ value achieved by the current high-angular-resolution imaging.

6.1.2. Source Companion Flux Prior Probability is Maximum at Source Flux

If the angular Einstein radius $\theta_{\rm E}$ is relatively small, as with M16227 ($\theta_{\rm E,obs} = 0.23 \pm 0.01$ mas), M08310 ($\theta_{\rm E,obs} = 0.16 \pm 0.01$ mas), and M11293 ($\theta_{\rm E,obs} = 0.26 \pm 0.02$ mas), the prior probability of H_L in a region brighter than $\sim$20 mag, where the observed excess flux is distributed, is smaller than or comparable to the prior probability of $H_{\rm SC}$, as shown in the bottom-right panels in Figures 2(a)–4(a).

The same is also determined from the distributions of mass and distance in the left panels in the same figures. As seen from the red dots of the D_L–M_L distributions in the left panels in Figures 2(a)–4(a), for events with small $\theta_{\rm E,obs}$, the peak of the joint prior probability distribution of D_L and M_L is at a late- or mid-M dwarf close to the source star along the shape of the $\theta_{\rm E}$ mass–distance relation. This is because in the Galactic model, there are many more stars in the bulge than in the disk, and there are many more low-mass stars than high-mass stars. Moreover, there is another factor, namely the microlensing event rate ($\propto D_L^2\, \theta_{\rm E}\, \mu_{\rm rel}$), which increases with D_L for a given $\theta_{\rm E}$ and $\mu_{\rm rel} = \theta_{\rm E}/t_{\rm E}$.

Meanwhile, the distribution of the source companion is different. The green dots in the same panels are distributed in a broad mass range at the source distance, and they outnumber the red dots of the lens in $M \gtrsim 0.6\, M_\odot$, where the intersection of the two mass–distance relations of $\theta_{\rm E}$ and $H_{\rm ex,obs}$ is located for these three events. The source companion mass distribution has a high probability at $M \gtrsim 0.6\, M_\odot$ because the peak of the $M_{\rm SC}$ distribution is at the source mass of each event, which is around 0.8–1.1 $M_\odot$ depending on the event, and the probability remains high at somewhat lower masses. This distribution of the mass $M_{\rm SC}$ is a reflection of the distribution of the mass ratio $q_{\rm SC}$ in Figure 12, which has a peak at $q_{\rm SC} = 1$ and a gentle slope toward $q_{\rm SC} < 1$. This property of the $q_{\rm SC}$ distribution also indicates that the peak of the probability distribution of the source companion magnitude $H_{\rm SC}$ is at the source magnitude $H_{S,\rm obs}$, and the probability remains high for somewhat fainter magnitudes.

Therefore, although the lens has an advantage of $P_{\rm exist} = 1$, in a case where an observed excess has the brightness of the source star or is slightly fainter, the probability of a source companion being the origin of the excess is comparable to or larger than the probability of the lens being the origin when $\theta_{\rm E}$ is small.

6.2. Event with a Large Angular Einstein Radius $\theta_{\rm E}$

The result for O120563, which has a very large angular Einstein radius $\theta_{\rm E,obs} = 1.4 \pm 0.1$ mas, shows a very small uncertainty of $H_L - H_{\rm excess} = 0.005^{+0.068}_{-0.004}$, which indicates that nearly the entire fraction of the excess flux is highly likely to originate from the lens flux. This is because the angular Einstein radius $\theta_{\rm E}$ is proportional to $\sqrt{M_L \pi_{\rm rel}}$ and a large angular Einstein radius indicates a massive and/or close lens, i.e., a bright lens star. In other words, a value of $\theta_{\rm E}$ can effectively impose a lower limit on the lens flux or an upper limit on the lens magnitude assuming that the lens is not a remnant.[9] Thus, there is a critical value of $\theta_{\rm E}$ above which the corresponding lower limit of the lens flux is brighter than most of the source companions that are the main contaminants.

As discussed in Section 6.1.2, the peak of the probability of the source companion magnitude is at the source magnitude. Furthermore, considering that the mass-ratio distribution in Figure 12 indicates a small probability of $q_{\rm SC} > 1$, which is also the same for other events, the critical $\theta_{\rm E}$ value is roughly a value that gives a lower limit of the lens flux that is equal to the source flux. We can constrain the lens mass by AO observations of the event with such a promising $\theta_{\rm E}$ value before the lens star is sufficiently separated from the source star. For O120563 with $\theta_{\rm E,obs} = 1.4 \pm 0.1$ mas, the source magnitude of $H_{S,\rm obs} = 18.57 \pm 0.03$ is fainter than even the faint end of the prior probability distribution of the lens magnitude, as shown in the bottom-right panel in Figure 5(a). This indicates that $\theta_{\rm E,obs}$ is higher than the critical value; thus, we can see that the probability of contamination from the source companion is very small without calculating contamination probability.

Moreover, in this specific case, there is another reason why we can nearly completely rule out contributions from contaminants. Although the left panel or the bottom-right panel in the prior distribution of Figure 5(a) shows a small probability of the source companion or ambient stars having the brightness of the observed excess flux, the posterior distribution of Figure 5(b) does not show any possibility for such a case where a source companion or ambient stars are the

[9] A mathematical lower limit of the lens flux for a given $\theta_{\rm E}$ is 0 when $M_L \to 0$ and $(D_L/D_S) \to 0$; however, the lensing probability for such an extremely close object is also 0. Hence, we can effectively impose a lower limit on the lens flux within a likely range of (D_L/D_S). We also note that this is true only when the lens is a single star. A remnant or binary lens could be fainter than the lower limit.

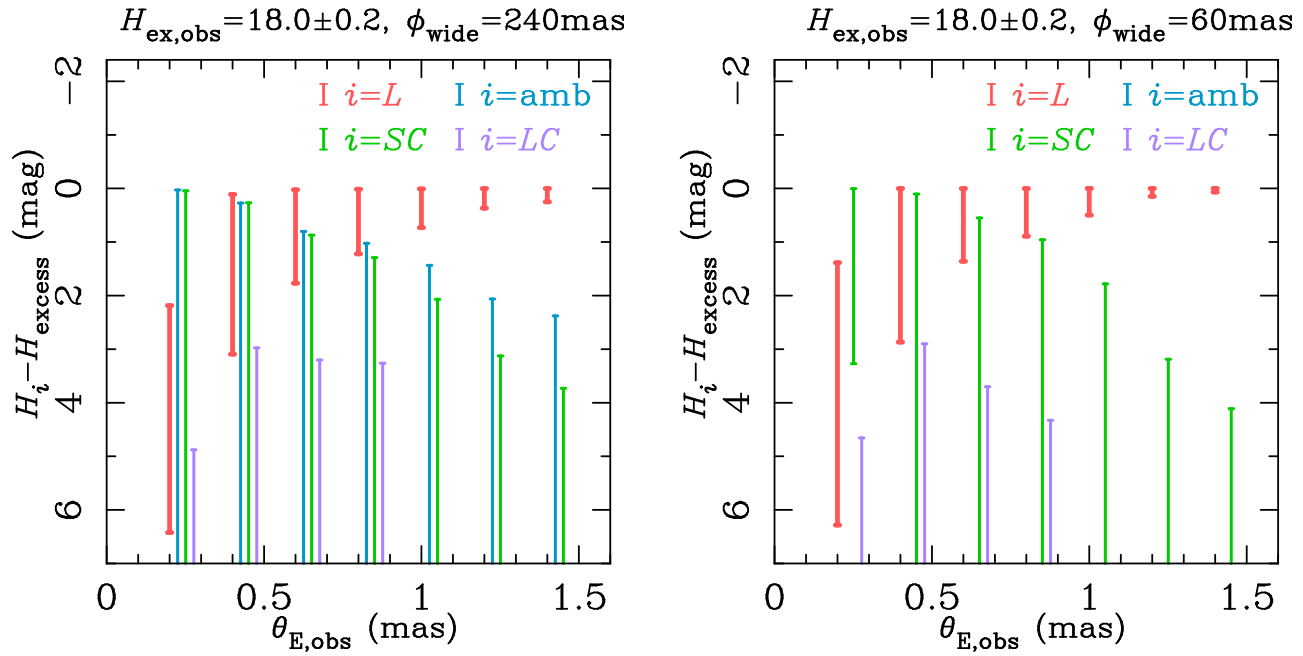

Figure 14. 1σ ranges of $H_i - H_{excess} = -2.5 \log f_i$ ($i = L$, amb, SC, LC) in the joint posterior PDF $f_{post}(F_L, F_{amb}, F_{SC}, F_{LC} | F_{excess} = F_{ex,obs})$ for hypothetical events with seven different $\theta_{E,obs}$ values, on which the excess brightness of $H_{ex,obs} = 18.0 \pm 0.2$ is measured with two different ϕ_{wide} values. $H_i - H_{excess} = 0$ is equivalent to $F_i = F_{excess}$. Plots for $i =$ amb, SC, LC are horizontally shifted so that each bar is recognizable. Note that most of the 1σ lower limits (i.e., 16th percentiles from the faintest) for $i =$ amb, SC, LC, or some of the 1σ upper limits (i.e., the 84th percentiles from the faintest) for $i =$ amb, LC are not plotted in this magnitude range because they are too faint or correspond to non-existing cases.

origin of the excess flux. This is because the observed excess flux is nearly the minimum limit of the lens flux expected from $\theta_{E,obs}$, as seen in the bottom-right panel in Figure 5(a). In this case, after subtracting the lens flux from the observed excess flux, the remainder always becomes much fainter than the excess flux; thus, no contaminant can have a brightness of $H_{ex,obs}$.

6.3. Event with a Long Einstein-radius-crossing Time t_E

For O120950, where a microlens parallax of $\pi_{E,obs} = 0.26 \pm 0.06$ was detected, the discussion is different. Because the microlens parallax π_E is proportional to $\sqrt{\pi_{rel}/M_L}$, the condition that π_E is constant requires a smaller π_{rel} for smaller M_L, which makes the lens fainter, while it requires a larger π_{rel} for larger M_L, which makes the lens brighter. As a result, both the bright lens and the faint lens are approved, and we cannot impose a lower limit on the lens flux from an observed π_E value in contrast to the constraint from θ_E. In this case, one might expect that the red dots in the left panel in Figure 6(a) should be distributed densely around the bottom-right part (i.e., low mass and distant lens) because such stars are the most common ones in our galaxy. However, the figure shows that they are actually distributed more broadly in the plane along the π_E mass–distance relation compared to the prior distribution of the three events with small θ_E in the left panels in Figures 2(a)–4(a).

To resolve the origin of this broad distribution, we need to recall another observed quantity, $t_{E,obs}$, which has the information on M_L but is not drawn explicitly on this plane. Because $t_E \propto \theta_E \propto \sqrt{M_L}$, the lens of O120950, where a long event timescale of $t_{E,obs} = 68$ days was observed, is likely to have a relatively large mass. Owing to the long $t_{E,obs}$, the prior probability that the lens is sufficiently bright to explain the observed, relatively bright excess flux increases; consequently, the estimated lens mass is similar to the value reported by the discovery paper of Koshimoto et al. (2017b), who derived the value by taking the mean of the solutions with $f_L = 1$ and $f_L = 0.5$. Note that Bhattacharya et al. (2018) confirmed that f_L is nearly 1 for this event by analyzing Keck and HST images taken in 2018, which indicates an elongation caused by a slightly separated source and lens. Their tightly constrained mass and distance are also plotted in light blue in Figure 6(b).

Because a long event timescale of $t_E \gtrsim 50$ days is typically required to detect the annual parallax effect, we note that it is not by chance that we have a long t_E value for this event where π_E is detected. It indicates that the probability of a lens being an origin of the excess flux is generally high when a bright excess flux is observed at the location of the event where the annual parallax effect is detected.

6.4. Dependence on the Angular Einstein Radius and the Angular Resolution

To investigate how the constraint on the lens properties varies depending on the angular Einstein radius, we conduct a Bayesian analysis of hypothetical events with seven different angular Einstein radius values, $\theta_{E,obs} = (0.2, 0.4, 0.6, 0.8, 1.0, 1.2, 1.4)$ mas, with 10% uncertainties for each. We consider the case where the excess brightness of $H_{ex,obs} = 18.0 \pm 0.2$ is measured on each event position. For the radius of the unresolvable circle, we consider two values, $\phi_{wide} = 60$ mas and $\phi_{wide} = 240$ mas, the minimum value and a value 1.5 times larger than the maximum value in the five events listed in Table 3, respectively. We use the values for M16227 for other input parameters, which means we use $n_{amb} = 7.3\,as^{-2}$, the densest number density in the five events' fields, for these calculations.

Figure 14 shows the resulting 1σ ranges (i.e., the 16th–84th percentiles) of $H_i - H_{excess}$ ($i = L$, amb, SC, LC) in the posterior distributions from those analysis. The left panel

shows those with $\phi_{\rm wide} = 240$ mas while the right panel shows those with $\phi_{\rm wide} = 60$ mas. These results confirm that the uncertainty of $H_L - H_{\rm excess}$ has a strong correlation with the size of $\theta_{\rm E,obs}$ and also that a source companion is the main source of contaminants regardless of the $\phi_{\rm wide}$ value.

Moreover, it is notable that the 1σ ranges of $H_L - H_{\rm excess}$ in the left panel are similar to those in the right panel even with the four times difference in $\phi_{\rm wide}$ values, or equivalently, 16 times difference of the mean number of ambient stars between the two panels. In the case with $\phi_{\rm wide} = 240$ mas, ambient stars do contribute as a contaminant, but it does not lead to very different $H_L - H_{\rm excess}$ estimates. This indicates that the ambient star flux basically does not affect our conclusion whether or not the lens is likely to be the origin of the excess, as long as $\phi_{\rm wide}$ is within a typical range ($\lesssim$200 mas) for the AO observations.

6.5. Lens Companion as a Contaminant

Finally, we discuss how a lens companion works as a contaminant. Our results show that the probabilities of a lens companion being the origin of the excess flux are small for all the events we analyzed. For example, the averaged contributions from the lens companions to the excess fluxes are $\langle f_{\rm LC} \rangle \leqslant 0.07$ for all five events. This is also seen in Figure 14, where the upper limits of $H_{\rm LC} - H_{\rm excess}$ never exceed 2.5 mag in any of the hypothetical event cases.

We find that there are two main reasons for this small contribution from the lens companion. First, the requirement for its location to be undetectable from the light curves, namely the requirement that $a_{\rm LC,\perp}/D_L > \phi_{\rm close,LC}$, effectively reduces the possibility of a lens companion, especially for high-magnification events with $u_{0,\rm obs} \lesssim 0.01$, as seen in the comparison of the full and the undetected binary distributions in the $q_{\rm LC}$ and $\log a_{\rm LC}$ panels in Figure 12. Second, to be the main origin of the excess flux instead of the lens star, a binary system that consists of a lens companion with the brightness of an observed excess flux and a fainter lens that negligibly contributes to the excess are required. This is equivalent to the requirement of $q_{\rm LC}$ being moderately larger than 1. However, the probability of the case where the lens is a secondary star (i.e., $q_{\rm LC} > 1$) is low, as seen from the undetected binary distribution (solid curves) in the panels labeled $q_{\rm LC}$ in Figure 12. In summary, the probability of the lens companion being the main contaminant is effectively reduced by both the requirement on its semimajor axis (the first reason above) and the requirement on its mass ratio (the second reason above). Consequently, a confined parameter space remains.

This consideration of the possibility of a lens companion provides an important insight even when a lens candidate is detected with separation from the source (Batista et al. 2015; Bennett et al. 2015, 2020; Bhattacharya et al. 2018; Vandorou et al. 2019). Because such a candidate can be either the lens or a companion to the lens, one needs to distinguish between these cases. When the event has a 1D microlens parallax measurement from the light curve, it is distinguishable because both $\pi_{\rm E}$ and $\theta_{\rm E}$ can be determined to be independent of the measured brightness of the candidate (Bhattacharya et al. 2018; Bennett et al. 2020). Meanwhile, when the event does not have any microlens parallax measurement, the possibility of a lens companion cannot be ruled out in the same way (Vandorou et al. 2019). However, our calculation indicates that it is not highly likely that an unresolvable companion that is significantly brighter than the lens exists. This is especially the case for a high-magnification event such as MOA-2013-BLG-220 (Vandorou et al. 2019) or MOA-2007-BLG-400 (A. Bhattacharya et al. 2020, in preparation) because of its high sensitivity to a companion, although the quantitative probability should be calculated in each case to show how unlikely it is.

7. Prediction of Lens Detectability

It is difficult to impose a strong constraint on the lens flux or the lens mass if the prior probability of the lens flux having the brightness of the observed excess flux is smaller than or similar to that of other possible contributors. Does this imply that we could have imposed a tight constraint on the lens mass if we had observed $H_{\rm ex,obs} \sim 22$ mag for M11293? This is true if we had observed an excess flux of $\sim$22 mag; however, it is impossible to detect such faint excess flux at the position of the much brighter source star. Because the source flux $F_{S,\rm obs}$ has an uncertainty, we can claim that we detect the excess flux at the position of the source star only when the target flux (i.e., the source flux plus the others' flux) is statistically significantly brighter than the source flux. With the 3σ confidence limit, a detectable excess flux should have a greater brightness than $F_{\rm ex,3\sigma} = 3\sigma_{F_S}$, where σ_{F_S} is the 1σ uncertainty of the source flux.

Figure 15 shows the prior probability distribution of the excess flux for each event. These distributions are repeated from the top-right panels in the (a) components of Figures 2–6, and additional information is plotted on the probability distributions. The gray hatched areas in Figure 15 are the undetectable region $H_{\rm excess} > H_{\rm ex,3\sigma}$, where $H_{\rm ex,3\sigma}$ is the magnitude corresponding to $F_{\rm ex,3\sigma}$. We consider unmagnified source stars to derive $F_{\rm ex,3\sigma}$. Because the region around $H_{\rm excess} \sim 22$ in the plot for M11293 is hatched, we cannot detect excess flux value around $\sim$22 mag, where the prior probability of H_L is the highest in our calculation. The red solid and dashed curves represent the median and 1σ values of the posterior distribution of the lens mass obtained when the excess flux is measured as $H_{\rm ex,obs} = H_{\rm excess} \pm 0.1$, where $H_{\rm excess}$ is the value of the horizontal axis. The black solid and dashed vertical lines represent the actual observed $H_{\rm ex,obs}$ values and the 1σ uncertainties. Thus, the mass value at the intersection of the red curves and the black lines corresponds to the estimated mass value in Table 4.

We emphasize that all components of Figure 15 except for the black vertical lines can be obtained once the parameters derived from the microlens light curve are determined with an assumed value of $\phi_{\rm wide}$. When one is planning high-angular-resolution follow-up observations, such a figure indicates the extent to which one can expect to constrain the lens properties. For example, it seems difficult to constrain the lens mass tightly for M16227 and M08310 because the width of the 68% confidence interval of the red curves is large in any detectable excess flux region in the unhatched area. The situation is better for M11293, where a relatively faint source ($H_{S,\rm obs} = 19.20$ mag) and a small $\phi_{\rm wide}$ value (60 mas) were observed; however, it still seems difficult to constrain the lens mass tightly unless one observes an excess flux with $\sim$21 mag. Meanwhile, for O120563 and O120950, it seems like we can expect to constrain the lens mass tightly once an excess flux is observed, because the red shaded areas are large in their detectable $H_{\rm excess}$ region, and the width of the 68% confidence interval of the red dashed curves is small.

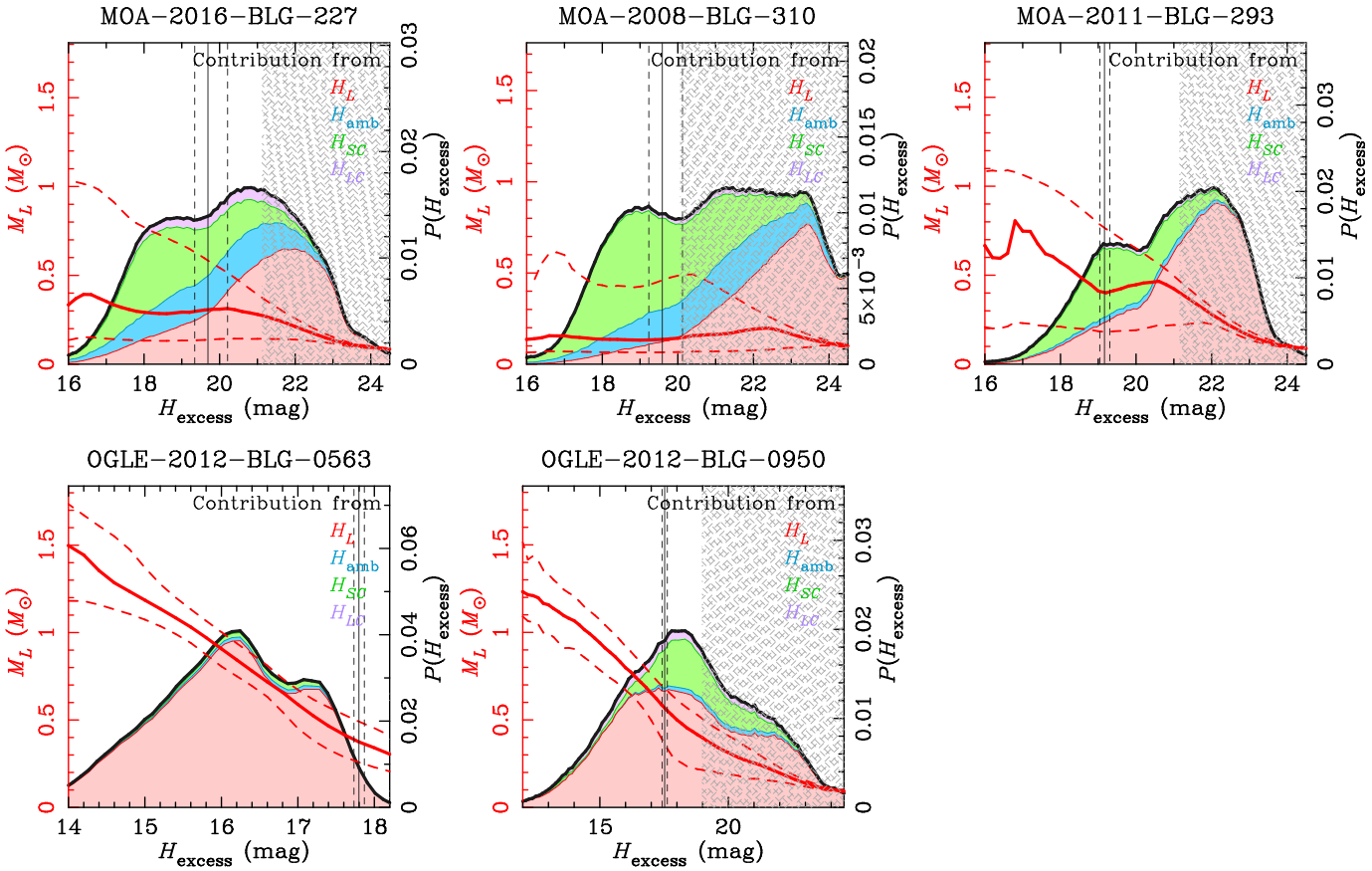

Figure 15. Predictions for lens detectability. Each panel shows the prior probability distribution of the excess flux for each event. They are repeated from the top-right panels in the (a) components of Figures 2–6, but with additional information. The red solid and dashed lines indicate the median value and 1σ confidence limits of the posterior probability distribution of the lens mass M_L, which would be obtained if we were to observe $H_{\rm ex,obs} = H_{\rm excess} \pm 0.1$ mag as a function of the magnitude of the excess flux $H_{\rm excess}$. The gray hatched regions indicate 3σ undetectable regions of the $H_{\rm excess}$ value owing to the noise of the source flux, where we assumed unmagnified sources. The vertical black solid and dashed lines indicate the representative value and 1σ uncertainty of the actual observed excess flux $H_{\rm ex,obs}$, respectively.

If one's goal is to measure the lens mass, such a prediction is informative for the selection of promising candidates for the planned follow-up observations. When an event seems unlikely to be given a good mass measurement by the excess flux observation, then one should wait to observe it until the lens is sufficiently separated from the source star. At this time, we no longer have the detection limit of $F_{\rm ex,3\sigma}$ due to the source star nor the high contamination probability from the source companion. There is still a possibility of contamination from the lens companion at this time; however, it is not highly likely as discussed in Section 6.5.

We recall that these predictions depend on the prior distributions that we used. Conversely, one can test the prior distribution by comparing the observed excess flux with the detection probability of the excess flux expected from the prediction. Hence, if our goal is to test the prior, we should not select targets for follow-up observations on the basis of the detectability of the lens flux because it causes a bias in the observed sample. In particular, a prior that is currently unknown but is of interest is the planet-hosting probability, which is assumed to be the same for all the stars in the above-mentioned calculations. As described in Section 8, a different assumption on this probability changes the posterior distributions moderately, which indicates that we can statistically study the planet-hosting probability using excess flux measurements for a large number of planetary events.

8. Dependence on Planet-hosting Probability

We have calculated the lens flux probability distributions under the assumption that all stars are equally likely to host a planet. However, several studies have shown the dependence of the planet occurrence on the host mass, metallicity, and so on (Johnson et al. 2010; Montet et al. 2014; Mulders et al. 2015). The dependence of the planet-hosting probability on the host mass is often assumed to follow a power law $P_{\rm host} \propto M_h^{\alpha}$, where M_h is the host mass. Johnson et al. (2010) used samples of the radial velocity (RV) method and found a linear relationship (i.e., $\alpha = 1$) between the host mass and the occurrence of giant planets within $\sim$2 au around host stars whose masses range from 0.5 $M_\odot$ to 2.0 $M_\odot$. This relationship is confirmed by a more recent study of Ghezzi et al. (2018). Meanwhile, the results of the transit method have shown the occurrence of more planets around the latter type of stars for low-mass planets close to their host, which indicates that $\alpha < 0$. For example, Mulders et al. (2015) found a higher occurrence rate of Earth- to Neptune-sized planets (1–4 $R_\oplus$) around later-type stars in all orbital periods probed by Kepler. They reported that the planets around M dwarfs occur twice as

Table 5
Lens Properties Calculated from the Posterior Probability Distributions Assuming $\alpha = +1/-1$

Event	M16227	M08310	M11293	O120563	O120950
References	1	2	3, 4	5	6
This work ($\alpha = 1$)					
M_L ($M_\odot$)	$0.42^{+0.18}_{-0.21}$	$0.34^{+0.30}_{-0.22}$	$0.67^{+0.12}_{-0.37}$	0.41 ± 0.11	$0.60^{+0.09}_{-0.13}$
M_p	$4.1^{+1.8}_{-2.0}$ M_{Jup}	36^{+33}_{-23} $M_\oplus$	$3.7^{+0.7}_{-2.0}$ M_{Jup}	$0.47^{+0.12}_{-0.13}$ M_{Jup}	41^{+9}_{-10} $M_\oplus$
D_L (kpc)	6.9 ± 0.9	$7.8^{+1.2}_{-1.0}$	7.6 ± 0.9	1.7 ± 0.5	$2.9^{+0.8}_{-0.7}$
$a_\perp$ (au)	$1.49^{+0.21}_{-0.19}$	$1.25^{+0.23}_{-0.20}$	...	...	$2.75^{+0.50}_{-0.48}$
$a_{\perp,close}$ (au)	...	...	$1.10^{+0.15}_{-0.14}$	$0.89^{+0.21}_{-0.22}$	...
$a_{\perp,wide}$ (au)	...	...	$3.66^{+0.49}_{-0.47}$	$5.25^{+1.22}_{-1.29}$	...
$P(f_L > 0.1)$	89.1%	69.1%	80.2%	100.00%	94.5%
$P(f_L > 0.5)$	55.0%	44.9%	52.1%	99.97%	80.9%
$P(f_L > 0.9)$	31.8%	31.2%	37.3%	90.7%	61.5%
$H_L - H_{excess}$ (mag)	$0.59^{+1.55}_{-0.59}$	$1.09^{+2.69}_{-1.08}$	$0.61^{+2.12}_{-0.61}$	$0.003^{+0.064}_{-0.002}$	$0.02^{+0.94}_{-0.02}$
This work ($\alpha = -1$)					
M_L ($M_\odot$)	$0.18^{+0.20}_{-0.08}$	$0.096^{+0.096}_{-0.040}$	$0.23^{+0.33}_{-0.11}$	$0.33^{+0.13}_{-0.12}$	$0.48^{+0.16}_{-0.33}$
M_p	$1.7^{+1.9}_{-0.8}$ M_{Jup}	10^{+10}_{-4} $M_\oplus$	$1.3^{+1.8}_{-0.6}$ M_{Jup}	$0.38^{+0.14}_{-0.13}$ M_{Jup}	32^{+13}_{-21} $M_\oplus$
D_L (kpc)	6.3 ± 1.0	$7.0^{+1.1}_{-1.0}$	$6.8^{+1.0}_{-1.2}$	1.4 ± 0.5	$3.2^{+2.6}_{-1.0}$
$a_\perp$ (au)	1.34 ± 0.22	$1.11^{+0.21}_{-0.19}$	...	...	$2.36^{+0.62}_{-0.93}$
$a_{\perp,close}$ (au)	...	...	$0.96^{+0.17}_{-0.18}$	$0.74^{+0.25}_{-0.24}$	...
$a_{\perp,wide}$ (au)	...	...	$3.20^{+0.57}_{-0.59}$	$4.33^{+1.46}_{-1.40}$	...
$P(f_L > 0.1)$	56.7%	26.6%	31.0%	99.99%	66.6%
$P(f_L > 0.5)$	23.2%	16.7%	12.7%	99.88%	51.1%
$P(f_L > 0.9)$	14.1%	14.6%	8.7%	88.5%	37.2%
$H_L - H_{excess}$ (mag)	$2.21^{+1.63}_{-1.97}$	$4.27^{+2.26}_{-3.75}$	$3.20^{+1.07}_{-1.85}$	$0.005^{+0.075}_{-0.004}$	$0.68^{+4.42}_{-0.68}$

Notes. Same as Table 4, but for $\alpha = 1$ and $\alpha = -1$, where α is the slope of the planet-hosting probability, $P_{host} = M_h^\alpha$. See Table 4 for the references or the other notes.

Table 6
Dependence of the Lens Mass Estimates on Various Prior Choices when $\alpha = 0$

Difference from Tables 2–3	M16227	M08310	M11293	O120563	O120950
None (fiducial)[a]	$0.28^{+0.24}_{-0.15}$	$0.14^{+0.27}_{-0.07}$	$0.41^{+0.35}_{-0.23}$	$0.37^{+0.12}_{-0.12}$	$0.57^{+0.11}_{-0.20}$
ϕ_{wide} doubled	$0.24^{+0.21}_{-0.11}$	$0.13^{+0.21}_{-0.06}$	$0.39^{+0.36}_{-0.21}$	$0.37^{+0.12}_{-0.11}$	$0.56^{+0.12}_{-0.23}$
Isochrones for all mass range[b]	$0.28^{+0.25}_{-0.14}$	$0.13^{+0.27}_{-0.07}$	$0.43^{+0.32}_{-0.24}$	$0.35^{+0.09}_{-0.10}$	$0.56^{+0.11}_{-0.20}$
Constant extinction ($A_{H,S} = A_{H,L} = A_{H,rc}$)	$0.28^{+0.24}_{-0.15}$	$0.14^{+0.26}_{-0.07}$	$0.41^{+0.35}_{-0.22}$	$0.38^{+0.12}_{-0.12}$	$0.57^{+0.11}_{-0.20}$
Zero extinction ($A_{H,S} = A_{H,L} = 0$)	$0.27^{+0.23}_{-0.14}$	$0.14^{+0.27}_{-0.08}$	$0.43^{+0.25}_{-0.24}$	$0.31^{+0.11}_{-0.10}$	$0.52^{+0.12}_{-0.24}$
B14 Galactic model	$0.29^{+0.25}_{-0.15}$	$0.15^{+0.28}_{-0.08}$	$0.43^{+0.34}_{-0.23}$	$0.38^{+0.12}_{-0.12}$	$0.58^{+0.11}_{-0.19}$
Z17 Galactic model	$0.39^{+0.18}_{-0.17}$	$0.23^{+0.29}_{-0.12}$	$0.55^{+0.22}_{-0.27}$	$0.36^{+0.12}_{-0.12}$	$0.56^{+0.11}_{-0.15}$
$\gamma = -0.1$ [c]	$0.29^{+0.25}_{-0.15}$	$0.14^{+0.28}_{-0.07}$	$0.52^{+0.26}_{-0.32}$	$0.37^{+0.12}_{-0.12}$	$0.58^{+0.10}_{-0.16}$
$\gamma = -0.5$ [c]	$0.30^{+0.24}_{-0.16}$	$0.15^{+0.30}_{-0.08}$	$0.63^{+0.16}_{-0.41}$	$0.38^{+0.12}_{-0.12}$	$0.59^{+0.10}_{-0.14}$
$\gamma = -0.9$ [c]	$0.31^{+0.24}_{-0.17}$	$0.15^{+0.32}_{-0.08}$	$0.70^{+0.09}_{-0.46}$	$0.38^{+0.12}_{-0.12}$	$0.60^{+0.09}_{-0.13}$
$\phi_{close,SC} = 5\,\theta_E$	$0.30^{+0.24}_{-0.16}$	$0.14^{+0.30}_{-0.08}$	$0.56^{+0.23}_{-0.35}$	$0.37^{+0.12}_{-0.12}$	$0.59^{+0.10}_{-0.16}$

Notes. All values are given in $M_\odot$.
[a] Values from Table 4.
[b] Age and metallicity distributions different from the fiducial ones are also applied. See Section 9.2.
[c] γ = const. is applied to the binary distribution for a non-secondary star $f_{prim}(q, a|M) \propto q^\gamma$. -0.1, -0.5, and -0.9 are approximately the 1σ, 2σ, and 3σ lower limits on γ from Shvartzvald et al. (2016).

frequently as those around G dwarfs and thrice as frequently as those around F dwarfs.

As for the sensitivity region for the microlensing method, no study has found a statistically significant dependence of the planet occurrence on the host mass. Vandorou et al. (2019) and A. Bhattacharya et al. (2020, in preparation) measured the separation between the lens and the source stars of MOA-2013-BLG-220 and MOA-2007-BLG-400, respectively, using the Keck telescope. They showed that the host masses are both located at the >90th percentiles of the probability distribution calculated by Bayesian analysis assuming that all stars are equally likely to host a planet. Because both planets are gas giants, this might indicate that such giant planets are more likely to be hosted by a more massive star, which is consistent with the RV results mentioned above. Furthermore, microlensing has greater sensitivity (sub-kiloparsec to ~10 kpc) to the distance of planetary systems from the Sun compared to other methods (less than kiloparsecs). It is also possible that the

planet occurrence changes as a function of the distance of the microlensing planets. In fact, Penny et al. (2016) suggested a possibility that planets in the bulge are less common than planets in the disk, which was not conclusive.

Because the planet-hosting probability for a microlensing planet is still unknown, here, we simply show the results with $\alpha = 1$ and $\alpha = -1$ in Table 5, where the planet-hosting probability $P_{\rm host} \propto M_h^{\alpha}$, as examples of variations of our results with different assumptions. Note that we use $\alpha = 0$ for $M_L < 0.1\,M_\odot$ in the model with $\alpha = -1$. The estimated lens mass becomes more massive with $\alpha = 1$ than with $\alpha = 0$ because the probability of a large contribution of the lens flux to the excess flux increases while the mass estimate with $\alpha = -1$ becomes less massive because of the lower probability of the large contribution from the lens.

9. Dependence on Other Priors

The results of this study depend on the choice of the prior distributions. Our fiducial choices are listed in Tables 2 and 3. The most influential uncertain prior is probably the planet-hosting probability discussed in Section 8. In this section, we review our choice of other priors and discuss how much their variation changes the estimates of the lens properties. Table 6 summarizes all the mass estimates with the different choices of priors applied in this section, where all results are consistent with our fiducial values within 1σ.

9.1. Dependence on Ambient Star Flux Prior

To calculate the $H_{\rm amb}$ prior distribution, we have used the number density of the target field $n_{\rm amb}$, the separation angle that is the boundary between resolved and unresolved stars, $\phi_{\rm wide}$, and the flux distribution of a single ambient star, $L_1(F)$, as described in Section 4.1. Although there were some assumptions we made regarding $n_{\rm amb}$ and $L_1(F)$, $\phi_{\rm wide}$ is the most influential parameter for ambient star flux because the mean number of ambient stars is $\lambda_{\rm amb} \propto \phi_{\rm wide}^2$.

We have assumed $\phi_{\rm wide}$ to be a constant regardless of the brightness of a star, and it is possible for a star fainter than the excess to be missed even outside of the circle of $\phi_{\rm wide}$, as mentioned in Section 4.1.2. However, we showed that the ambient star flux does not affect the $H_L - H_{\rm excess}$ estimates that much, at least with $\phi_{\rm wide} < 240$ mas and $H_{\rm ex,obs} = 18.0 \pm 0.2$ mag in Section 6.4 or Figure 14; hence, it is not likely that the assumption on $\phi_{\rm wide}$ changes our results significantly. Nevertheless, to confirm it for each event's parameters, we double each $\phi_{\rm wide}$ value listed in Table 3 and calculate the posterior PDF for each event with the doubled $\phi_{\rm wide}$ or quadrupled mean number of ambient stars $\lambda_{\rm amb}$ under the assumption of $P_{\rm host} = $ const. (i.e., $\alpha = 0$) for all stars. The line denoted "$\phi_{\rm wide}$ doubled" in Table 6 shows the obtained mass estimates for the five events. All of these are very similar to the fiducial values in Table 4.

9.2. Dependence on Mass–Luminosity Relation

We have used an empirical mass–luminosity relation for the wide mass range of $M = 0.1$–$0.8\,M_\odot$. To evaluate the possible uncertainty due to this assumption, we also apply the PARSEC isochrone model for this mass range and calculate the lens mass with it. In the calculation, we also allow the age and metallicity to be wider than we assumed in Section 4.2.1. We take the distributions from Bennett et al. (2018a), who used ages of 1 Gyr $< T <$ 10 Gyr and 2 Gyr $< T <$ 12.6 Gyr for disk and bulge stars, respectively. Metallicities between $-2.8 <$ log $Z < -1.3$ are used for both disk and bulge stars, but with different weights depending on the age for each component. See Bennett et al. (2018a) for the weights and more details. The line denoted "Isochrones for all mass range" in Table 6 shows the obtained mass estimates for the five events, which shows similar values to the fiducial values.

9.3. Dependence on Extinction Distribution

For the extinction distribution toward a line of sight, we have used a simple dust disk model with the scale height of 100 pc, $A_H \propto 1 - \exp\left[-\frac{D}{0.1\ \mathrm{kpc}\ /\ \sin|b|}\right]$, as described in Section 4.5. To evaluate the effect of this assumption, we conduct our analysis with two extreme cases for the 3D extinction distribution, i.e., constant extinction and zero extinction. In the calculation with constant extinction, we assume $A_{H,i} = A_{H,\rm rc}$ $(i = S,\ L)$ while we assume $A_{H,i} = 0$ for zero extinction, regardless of the distances.

The two lines denoted "Constant extinction" and "Zero extinction" in Table 6 show the resulting mass estimates for these two cases. Although both cases are consistent with the fiducial values within 1σ, the median masses for O120563 and O120950 are somewhat lighter than the fiducial values. This is because as shown in Table 4, the median of the $H_L - H_{\rm excess}$ values for these two events is 0.005 mag and 0.08 mag, which are smaller than the $A_{H,\rm rc}$ values for these events; hence the $H_L - H_{\rm excess}$ estimates are sensitive to the variation of $A_{H,\rm rc}$ for these two events. Meanwhile, the median of the $H_L - H_{\rm excess}$ values for the other three events are much larger than the $A_{H,\rm rc}$ values for them; hence, it is not sensitive to the variation of $A_{H,\rm rc}$.

9.4. Dependence on Galactic Model

To calculate the joint prior PDF of M_L, D_L, D_S and v_t, $f'_{\rm pri}(M_L, D_L, D_S, v_{\rm t})$, we have used the S11 model in Koshimoto & Bennett (2019), as described in Section 4.2.1. As seen in Figure 8, the LF calculated with the S11 model shows a good agreement with the observed LF by Zoccali et al. (2003). Although it does not indicate a good agreement with the velocity distribution that is not related to brightness, Sumi et al. (2011) showed consistency between the Galactic model and the observation using the $t_{\rm E}$ distribution, which does depend on the velocity distribution. They showed that a simulated $t_{\rm E}$ distribution using nearly the same Galactic model as the S11 model is in good agreement with the observed $t_{\rm E}$ distribution from their two-year survey in the range of $t_{\rm E} \gtrsim 2$ days that covers all events' $t_{\rm E}$ values in this paper. This is why we chose the model as our fiducial model.

Nevertheless, we calculate the lens properties with the other two models used in Koshimoto & Bennett (2019), i.e., the B14 model and the Z17 model, which are slightly modified versions of the Bennett et al. (2014) and Zhu et al. (2017) models, respectively. The B14 model uses similar distributions to the S11 model for the mass function and bulge density. They used a disk density model, used by Robin et al. (2003), with a hole of scale length 1320 pc in the galactic center. They include a solid bar rotation of 50 km s^{-1} kpc^{-1} in their velocity distribution for the bulge stars, rather than the streaming motion used by the S11 model. The Z17 model uses the Kroupa (2001) MF with $1.3\,M_\odot$ cutoff. They adopt the same bulge density

profile as Equation (12), but with a 1.46 times smaller y_0 value of 424 pc and 1.82 times larger $\rho_{0,B}$ value of 3.76 $M_\odot$ pc^{-3}, i.e., a more centralized and in total 1.27 times more massive bulge model. For bulge kinematics, they assume the mean velocity of 0 and a faster velocity dispersion along all axes, 120 km s^{-1}, than the other two models. These are the main differences of these two models from the S11 model. More details of these models are given in Koshimoto & Bennett (2019) or each original paper.

The two lines denoted "B14 Galactic model" and "Z17 Galactic model" in Table 6 show the lens mass estimates with the two models. The result with the B14 model is almost same as the fiducial one while the result with the Z17 model shows larger median values for M16227, M08310, and M11293. This is because the bulge in the Z17 model has 1.27 times more massive and centralized mass distribution than the other two models, which makes the lens distance probability distribution shift toward the galactic center for these three events. Because of the upward trend of the mass–distance relation with a given θ_E on the mass–distance planes in Figures 2–4, the shift of the distance corresponds to the shift of the lens mass toward the more massive side. However, the shift level with the Z17 model is still small compared to their 1σ range, and totally consistent with our fiducial values with the S11 model. We note that Koshimoto & Bennett (2019) showed that the Z17 model's bulge mass must be multiplied by 0.75 ± 0.05 to be consistent with a dynamic model of the bulge by Portail et al. (2017).

9.5. Dependence on Binary Distribution

We have applied the undetected binary distribution constructed in Section 4.4, which combines the detection efficiencies and full binary distribution $f_{\rm arb}(q, a|M)$ of Equation (25) based on studies of nearby stellar binary systems (Duchêne & Kraus 2013) and the stellar present-day mass function, to the source system and lens system, which are likely to be in the bulge or disk. We chose to use the nearby binary distribution because no study thus far had explored the binary distribution for each spectral-type star with a wide coverage of semimajor axes in the galactic bulge. With these assumptions, a source companion is the main origin of contamination possibility as described in Sections 6.1 and 6.4 in contrast, a lens companion does not affect our lens mass estimates as described in Section 6.5. We discuss variations of our results due to possible uncertainties in the source companion prior below. Note that the small contributions from lens companions are attributed to the high detection efficiency $\epsilon_{\rm LC}$ for a wide range of companions and negative slopes of the IMF. We show that our assumption on $\phi_{\rm close,LC}$, which dominantly determines $\epsilon_{\rm LC}$, is reasonable in Section 10.3.1, while negative slopes of the IMF have been confirmed in the bulge field (Zoccali et al. 2000; Calamida et al. 2015).

Given the discussions in Sections 6.1 and 6.4, the large contributions of the source companions as contaminants originate from the following features in the undetected binary distribution: (i) a positive slope $\gamma > 0$ in $f_{\rm prim}(q, a|M) \propto q^\gamma$ that makes the probability of a bright companion high, (ii) the detection efficiency $\epsilon_{\rm SC}$ that is insensitive to a few orders of magnitude in the semimajor axis distribution, and (iii) a moderate binary fraction over the insensitive region, typically $0 \lesssim \log[a/{\rm au}] \lesssim 3$.

9.5.1. Slope of the Mass-ratio Function γ

Evidence for $\gamma > 0$ for the bulge stars was discovered by Shvartzvald et al. (2016), who studied a sample of 224 microlensing events including ~20 binary events to derive $\gamma = 0.32 \pm 0.38$.[10] However, the uncertainty is still large, and $\gamma < 0$ is also possible within 1σ. Table 6 shows the lens mass estimates with $\gamma = -0.1$, -0.5, and -0.9, which approximately correspond to the 1σ, 2σ, and 3σ lower limits on γ from Shvartzvald et al. (2016), respectively. In the calculations, we use γ values for the binary distribution of a non-secondary star $f_{\rm prim}(q, a|M) \propto q^\gamma$ regardless of the mass M. The median values are all similar to the fiducial values except for M11293. This is because the result of M11293 is sensitive to the source companion prior because ambient stars as the origin of the excess is almost completely ruled out. Nevertheless, their 1σ ranges are almost same as the fiducial one.

9.5.2. Detection Efficiency ϵ_{SC}

The detection efficiency is given by $\epsilon_{\rm SC} = \Theta[(\phi - \phi_{\rm wide})(\phi - \phi_{\rm close,SC})]$. In Sections 6.1 and 6.4, we discussed the difficulty of reducing the source companion probability by any reasonable $\phi_{\rm wide}$ value, but not for $\phi_{\rm close,SC}$. Our assumption of $\phi_{\rm close,SC} = \theta_E/4$ was originally set by Batista et al. (2014).

Skowron et al. (2009) found projected separations of two to seven times θ_E in the binary source fittings on their 19 repeating event candidates, but the average detection efficiency is 0.0105, which is very small. We can also detect a source companion through the xallarap effect, but the sensitivity is up to ~1000 day period, i.e., $\lesssim \theta_E$ (Poindexter et al. 2005), and the detection efficiency for them is close to 0 unless the event timescale is comparable to the period. Thus, the assumption of $\epsilon_{\rm SC} = 1$ for companions closer than $\theta_E/4$ is not likely to overestimate the source companion probability significantly. To show the robustness of our results to this assumption, we conduct our analysis with $\phi_{\rm close,SC} = 5\,\theta_E$, i.e., a $\phi_{\rm close,SC}$ 20 times larger than the fiducial one, and show a result consistent with the fiducial one in Table 6.

9.5.3. Binary Fraction in the Insensitive Region $0 \lesssim \log[a/{\rm au}] \lesssim 3$

A moderate binary fraction in $0 \lesssim \log[a/{\rm au}] \lesssim 3$ is also probably the case in the bulge because star-forming processes in the bulge and disk are not likely to be different from each other significantly, given their similar IMFs. Kroupa (1995) proposed a star formation process where all stars are born as a binary member and then some of them become single stars due to dynamic interactions within a star cluster. Marks & Kroupa (2011) applied the model to star clusters under various environments including different types of galaxies and show that a moderate fraction of companions always exists in $0 \lesssim \log[a/{\rm au}] \lesssim 3$ after dynamic evolution, which indicates a high dynamic stability. Their high stability is also supported by the fact that nearby stars in all mass ranges take the highest binary frequencies in $0 \lesssim \log[a/{\rm au}] \lesssim 3$ (see Figure 10).

[10] Although their binary sample was contaminated by disk lenses, it is likely to be dominated by bulge lenses as ordinary microlensing events because they found a frequency consistent with the study of nearby stars assuming that the binary frequency is identical in the disk and bulge. If the binary events were dominated by disk lenses, the consistency would indicate a several times larger binary fraction for disk stars than that for the nearby stars, which is not very likely because the nearby stars also belong to the disk.

From the observation side, Skowron et al. (2009) analyzed 19 candidates of repeating microlensing events. From 12 promising candidates, they found 28% binary frequency in $1 < s < 36$, roughly corresponding to $0 \lesssim \log[a/\mathrm{au}] \lesssim 2$, assuming a uniform distribution in $\log q$ and $\log a$. Although their distribution assumption is different from ours, their result indicates a frequency even higher than ours in the region because the corresponding frequency is 18% in Figure 13. Furthermore, our result with $\phi_{\mathrm{close,SC}} = 5\ \theta_{\mathrm{E}}$ in Table 6 shows the robustness of our result on a smaller binary fraction because a 20 times larger $\phi_{\mathrm{close,SC}}$ corresponds to a 1.3 orders of magnitude narrower range of the insensitive region ($1.3 \lesssim \log[a/\mathrm{au}] \lesssim 3$) in a_{SC} compared to the fiducial model.

9.6. Remnant or Close Binary Lens

We have not considered the cases of a remnant lens in our calculations. This corresponds to an assumption of $P_{\mathrm{host}} = 0$ for such remnants. The assumption is probably true for neutron stars given the null result of the 11 yr study on 45 pulsars by Behrens et al. (2020). If this rareness of planets around neutron stars is attributed to their past explosion (i.e., supernova) and/or their very massive initial mass, this could be also true for black holes. Although no planet detection has been reported around white dwarfs so far, evidence of disintegrated rocky objects has been reported around them or on their surface (Zuckerman et al. 2003; Koester et al. 2014).

If their planet-hosting probability is comparable to that of late-type stars, including the remnant possibility affects our lens mass estimates little for M16227, M08310, and M11293, i.e., the three with small θ_{E}, but more largely for O120563 and O120950. It is beyond the scope of this paper because this work is focusing on how to deduce the lens flux posterior PDF from excess flux measurements considering the contamination probabilities, whereas the PDF for a remnant lens is independent of such measurements. We note that it is not straightforward to include the remnant possibility in the PDF for planetary events because their planet-hosting probability is even more uncertain than that for late-type stars. Thus, one should consider the possibility only when they have strong evidence for the lens being a remnant, e.g., a too faint lens flux or excess flux compared to expectations from its microlensing parameters assuming a stellar lens.

We have also assumed $P_{\mathrm{host}} = 0$ for tight close binary systems, which have the gravitational lensing effect that closely resembles that of a single star (assumption (ii) in the top of Section 4.4). This is not true because such a circumbinary planet has been detected by microlensing (Bennett et al. 2016). The corresponding region is approximately given by Equation (32), which is $\lesssim$0.1 mas in angular separation for the relatively low-magnification event M16227 and less for high-magnification events. The top panel of Figure 13 shows that $\lesssim$10% of the source star has a companion at $\lesssim$0.1 mas. Because we are considering the lens system, which is closer and usually less massive than the source star, this percentage gets even smaller because a less massive star is less likely to host a secondary star (see $P_{\mathrm{prim}}(M)$ in Figure 11) and also the physical distance corresponding to $\lesssim$0.1 mas gets shorter with closer distance. Therefore, considering the close binary systems only adds a population of several percent to the posterior PDF, which negligibly changes our lens mass estimates.

Table 7
Removed Fractions of Binary Companions Considered as Detectable when Considering the Prior Probability Distribution

Event	M16227	M08310	M11293	O120563	O120950
ϕ_{wide} (mas)	148	132	60	160	90
u_0	0.08	0.003	0.0035	0.001	0.10
θ_{E} (mas)	0.23	0.16	0.26	1.4	∼0.5
$P_{\mathrm{det,SC}}$	0.135	0.135	0.160	0.203	0.193
$-P_{\mathrm{det,SC_{close}}}$	0.066	0.058	0.077	0.141	0.106
$-P_{\mathrm{det,SC_{wide}}}$	0.069	0.077	0.083	0.062	0.087
$P_{\mathrm{det,LC}}$	0.273	0.357	0.372	0.442	0.334
$-P_{\mathrm{det,LC_{close}}}$	0.254	0.348	0.336	0.342	0.261
$-w/$(i)–(iv)[a]	0.085	0.169	0.163	0.199	0.085
$-w/$(i)–(iii)[a]	0.257[b]	0.336	0.330	0.309	0.269[b]
$-P_{\mathrm{det,LC_{wide}}}$	0.019	0.009	0.036	0.100	0.073

Notes. Fractions are given with respect to all the scenarios including both rejected and accepted scenarios in the Monte Carlo simulation for each event.
[a] Factors (i)–(iv) are explained in Section 10.3.1.
[b] These are larger than the original $P_{\mathrm{det,LC_{close}}}$ values because of the simulated detection efficiencies in Figure 16 that have a wider sensitivity than the approximate formula.

10. Comparison of Predicted and Detected Fractions of Binary Companions

In Section 9.5, we showed the robustness of our lens mass estimates to the various priors for the undetected binary distribution. In this section, we test our fiducial distribution by comparing the number of detectable companions predicted by the distribution with the actual detected number of companions.

The detectable fraction of companions in our model is given by solving Equation (36) in Section 4.4.4 for $P_{\mathrm{det},i}$ (i = SC, LC),

$$P_{\mathrm{det},i} = \frac{P_{\mathrm{exist,full},i} - P_{\mathrm{exist,undet},i}}{1 - P_{\mathrm{exist,undet},i}}, \tag{40}$$

where $P_{\mathrm{exist,undet},i}$ and $P_{\mathrm{exist,full},i}$ are the P_{exist} values for object i in the undetected and full binary distributions (Figure 12), respectively. The flowchart in Figure 1 shows a practical way to calculate $P_{\mathrm{det},i}$ in our Monte Carlo simulation. $P_{\mathrm{det},i}$ includes both fractions of the companions located at $\phi_i < \phi_{\mathrm{close},i}$ and $\phi_i > \phi_{\mathrm{wide}}$ ($\phi_{\mathrm{SC}} = a_{\mathrm{SC},\perp}/D_S$, $\phi_{\mathrm{LC}} = a_{\mathrm{LC},\perp}/D_L$), where the former region is assumed to be detectable through the light curve while the latter region is assumed to be detectable through AO imaging. To distinguish them, we divide $P_{\mathrm{det},i}$ into $P_{\mathrm{det},i_{\mathrm{close}}}$ and $P_{\mathrm{det},i_{\mathrm{wide}}}$ such that the two fractions include companions only in the former region and only in the latter region, respectively. These fractions are shown in Table 7 for each event, in addition to the parameters related to the detection efficiency ϵ_i.

Below, we compare the $P_{\mathrm{det},i_{\mathrm{close}}}$ with the actual detected fraction of binary companions from light curves and find that there is a possible discrepancy between them for lens companions, which might indicate a lower stellar companion frequency in the planetary systems in the microlensing field than that for nearby random stars and/or the existence of several missed binary and planet events thus far.

10.1. Sample for Comparison

Because this comparison does not aim to have a statistically strong claim, we simply use a sample of published events, which allows the possibility of sample incompleteness in our test. However, we try to avoid the effect of publication bias at a certain level with the following requirement. First, we focus on planetary events, because planetary events are always attempted to be published regardless of the characteristics of the events, such as a binary source or stellar binary-lens feature in the light curve. Nevertheless, there is a publication delay due to the difficulty in modeling, impact of the discovery, etc. To avoid the effect of such delays as much as possible, we use a sample consisting of planetary events that have been identified by 2014, where we assume that the most recognizable planetary events have been published to date.

These two requirements yield a sample of 49 planetary events ($q < 0.03$) that were identified by 2014 and published as of 2019 April. We note that recognition as a planetary event might be affected by whether the event light curve has a binary source or binary-lens feature. This indicates that the effect of publication bias is inevitable even if our requirement works very well as intended. Therefore, we cannot exclude the possibility of missed binary and planet events from the interpretations of the possible discrepancy found in Section 10.3 below. Nevertheless, we believe that it is worthwhile to conduct this test to determine whether there is clear evidence of discrepancy between the model expectation and the number of published events.

10.2. Comparison for Source Companion

Table 7 shows that the fraction of source companions detectable from the light curve is $P_{\mathrm{det,SC_{close}}} = 6\%$–$14\%$. We compare this fraction to the fraction of actually detected binary source events. In our sample of 49 planetary events, there are two events (Sumi et al. 2010; Bennett et al. 2018b) where the source star is in a binary system and one possible event (Furusawa et al. 2013) where the source star might be in a binary system. As a result, the fraction of actually detected binary source events in planetary events is 4%–6%, which is slightly less than but consistent with the fraction of $P_{\mathrm{det,SC_{close}}} = 6\%$–$14\%$ in Table 7. Thus, no clear evidence of contradiction between our model and observations is found thus far.

10.3. Comparison for Lens Companion

We find that the fraction of lens companions detectable through the light curve is $P_{\mathrm{det,LC_{close}}} = 25\%$–$36\%$. In this case, where only planetary events are in the sample, an average fraction of $P_{\mathrm{det,LC_{close}}}$ should correspond to the fraction of binary and planet (i.e., a planet in a binary system) events with respect to all planetary events detected via microlensing thus far. However, there are only three planetary systems where a stellar companion is detected through microlens light curves (Gould et al. 2014; Poleski et al. 2014; Bennett et al. 2016) in our sample of 49 published planetary events identified by 2014. Out of the three events, the stellar companion in OGLE-2008-BLG-092 (Poleski et al. 2014) was discovered through a very separated caustic, which is different from the central caustic, owing to fortuitous geometry in the sky. Therefore, only two binary and planet events have been discovered in the situation we have considered in this work, where the companion is detected through its central caustic. This indicates that their observational fraction is only $2/49 \sim 4\%$ and is much smaller than the $P_{\mathrm{det,LC_{close}}} = 25\%$–$36\%$ shown in Table 7.

In fact, we have used some crude assumptions in our model for simplicity, which could lead to the overestimation of the fraction $P_{\mathrm{det,LC_{close}}}$. Below we discuss these assumptions and reassess the $P_{\mathrm{det,LC_{close}}}$ estimate.

10.3.1. Reassessment of the Lens Companion Fraction Detectable via the Central Caustic

There are some factors in our calculation shown in Figure 1 that clearly or potentially cause an overestimation of $P_{\mathrm{det,LC_{close}}}$ for planetary events: (i) an inner undetectable region regarded as detectable, (ii) companions always generated from $f_{\mathrm{arb}}(q_{\mathrm{LC}}, a_{\mathrm{LC}}|M_L)$, (iii) the approximate formula for the central caustic size that is used to determine the close limit of the undetectable region $\phi_{\mathrm{close,LC}}$, and (iv) the existence of the detected planet. Factors (i), (iii), and (iv) might cause an overestimation of the "detectable" region while factor (ii) might cause an overestimation of the binary fraction in the lens systems. Here, we review these factors and reassess $P_{\mathrm{det,LC_{close}}}$ by dealing with those possible overestimations.

(i) *Inner undetectable region regarded as detectable*—We have regarded a very close stellar companion in the inner undetectable region approximately given by Equation (32) in Section 4.4.4 as detectable (i.e., counted in $P_{\mathrm{det,LC_{close}}}$) although they are in fact too close to be detected by light-curve modeling. This is because a correct treatment for this region, where M_L refers to the total mass of a binary system rather than an arbitrary star mass, requires a significant modification to our algorithm shown in Figure 1, whereas this region has little effect on the lens mass estimates as discussed in Section 9.6. Now that we are focusing on $P_{\mathrm{det,LC_{close}}}$ located beyond the arrow of "No ($\epsilon_{\mathrm{LC}} = 1$)" in Figure 1, the overestimation due to this region can be simply corrected by regarding them as undetectable or putting them beyond the arrow of "Yes ($\epsilon_{\mathrm{LC}} = 0$)."

(ii) *Companions always generated from* $f_{\mathrm{arb}}(q_{\mathrm{LC}}, a_{\mathrm{LC}}|M_L)$–Because the lens companions have been always generated from $f_{\mathrm{arb}}(q_{\mathrm{LC}}, a_{\mathrm{LC}}|M_L)$, $P_{\mathrm{det,LC_{close}}}$ refers to the integral of $f_{\mathrm{arb}}(q_{\mathrm{LC}}, a_{\mathrm{LC}}|M_L)$ with $0 < q_{\mathrm{LC}} < \infty$ over the detectable parameter spaces. However, it should be generated from $f_{\mathrm{arb}}\left(q_{\mathrm{LC}}, a_{\mathrm{LC}}|\frac{M_L}{1+q_{\mathrm{LC}}}\right)$, at least in the case where a counted companion is located close to the inner undetectable region but is still marginally detectable. This causes an overestimation of $P_{\mathrm{det,LC_{close}}}$ first because the integral of $f_{\mathrm{arb}}\left(q_{\mathrm{LC}}, a_{\mathrm{LC}}|\frac{M_L}{1+q_{\mathrm{LC}}}\right)$ should be conducted with $0 < q_{\mathrm{LC}} < 1$ to avoid double counting, and second because $M_L/(1+q_{\mathrm{LC}})$ is always smaller than M_L. Comparing $P_{\mathrm{prim}}(M/2)$ and $P_{\mathrm{prim}}(M) + P_{\mathrm{second}}(M)$ in Figure 11 might help in understanding this. Whether we should use $M = M_L$ or $M = M_L/(1+q_{\mathrm{LC}})$ probably depends on the s_{LC} value and the source trajectory; however, it is beyond the scope of this study to examine an accurate way to deal with it. Here, we decide to always use $f_{\mathrm{arb}}(q_{\mathrm{LC}}, a_{\mathrm{LC}}|M_L/2)$ to generate lens companions, and limit $q_{\mathrm{LC}} < 1$ when $s_{\mathrm{LC}} < 1$ but keep $q_{\mathrm{LC}} < \infty$ when $s_{\mathrm{LC}} > 1$ to conservatively estimate $P_{\mathrm{det,LC_{close}}}$.

(iii) *Use of approximate formula for the central caustic size*—We have used an approximate formula of the central

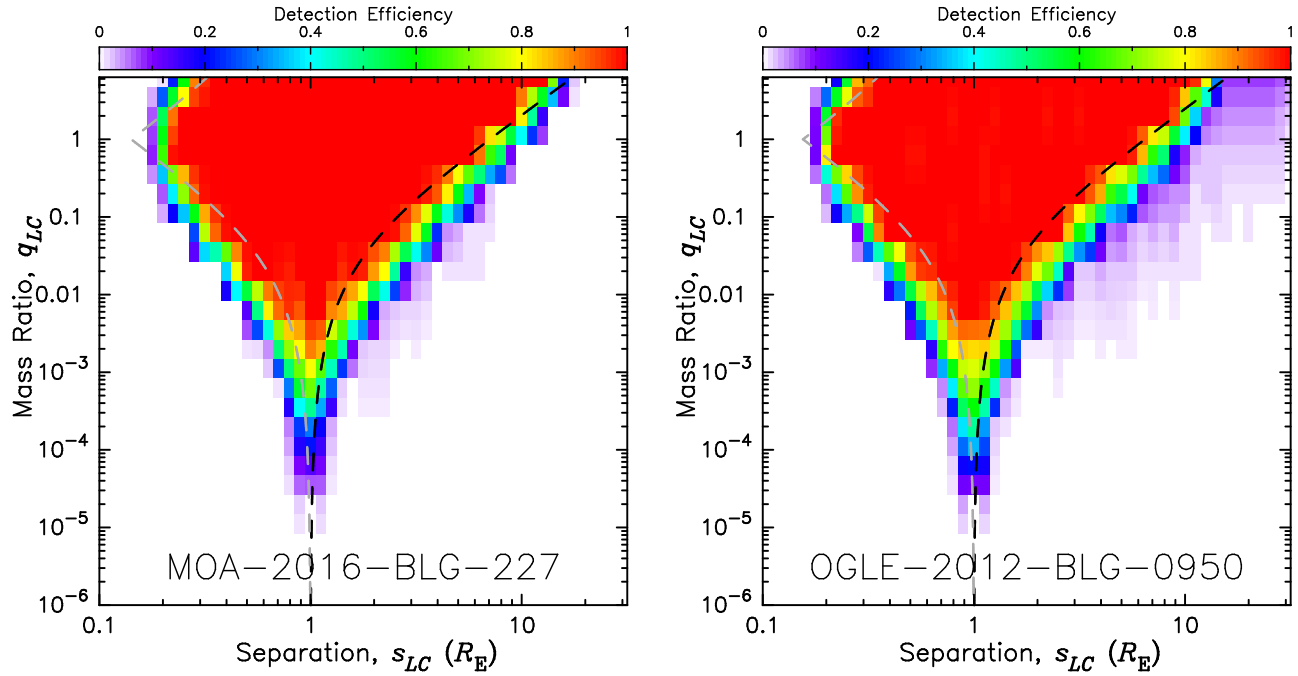

Figure 16. Detection efficiencies for additional lens companions assuming a binary-lens model for M16227 (left) and O120950 (right). See the Appendix for how they are calculated. The black and gray dashed lines represent two solutions of $w_{\rm LC} = u_{0,\rm obs}$, where an approximate formula of the central caustic size for $q_{\rm LC} \ll 1$, $w_{\rm LC} = 4q_{\rm LC}/(s_{\rm LC} - s_{\rm LC}^{-1})^2$, is used. The black line has been used as the border between the detection efficiencies $\epsilon_{\rm LC} = 1$ and $\epsilon_{\rm LC} = 0$ in our calculation of the prior and posterior PDFs.

caustic size, $w_{\rm LC} = 4q_{\rm LC}/(s_{\rm LC} - s_{\rm LC}^{-1})^2$, which is true only when $q_{\rm LC} \ll 1$, to calculate the inner and outer undetectable regions given by Equations (32) and (33), respectively. In fact, we find that this formula overestimates the caustic size in units of the angular Einstein radius by a maximum factor of $\sim$3 when $q_{\rm LC} \sim 1$. This seems to lead to an overestimation of the $\phi_{\rm close,LC}$ of Equation (35) by a factor of $\sim\sqrt{3}$. However, we also find that this factor is roughly canceled by the factor $\sim(1 + q_{\rm LC})^{3/4}$ ($\sim$1.68 when $q_{\rm LC} = 1$) for a wide ($s_{\rm LC} > 1$) stellar companion that originates in an unconsidered expansion of the angular Einstein radius by $\sqrt{1 + q_{\rm LC}}$ owing to the additional wide stellar companion.

We confirm this by calculating the detection efficiencies for M16227 and O120950 as shown in Figure 16. To calculate the detection efficiency, we follow Suzuki et al. (2016) but apply some modifications to deal with the expansion of the angular Einstein radius. The Appendix describes the details of the modifications. The region to the right of the black dashed line in the figure corresponds to the analytical outer undetectable region given by Equation (33), while the region to the left of the gray dashed line corresponds to the analytical inner undetectable region given by Equation (32). Both panels show that the black line lies nearly along the right edge of the red region of detection efficiency $\epsilon_{\rm LC} = 1$, while the gray line is located slightly to the left of the left edge of $\epsilon_{\rm LC} = 1$ when $q_{\rm LC} \sim 1$. This indicates that using Equation (33) as the outer undetectable region slightly underestimates the detectability of a stellar companion because both panels show moderate detection efficiencies even in the region to the right of the black dashed line. Meanwhile, using Equation (32) as the inner undetectable region slightly overestimates the detectability of a stellar companion with $q_{\rm LC} \sim 1$. This is because the expansion of the angular Einstein radius does not work at $s_{\rm LC} \ll 1$; thus, the factor of the overestimated caustic size is not canceled. Because Equations (33) and (32) misestimate the detectability in opposite directions, the misestimation is mitigated by using both of them. Nevertheless, using the simulated detection efficiency is clearly better than just using Equations (32)–(33) as the undetectable regions. Thus, we use the detection efficiencies shown in Figure 16 to calculate the $P_{\rm det,LC_{close}}$ values for M16227 and O120950.

(iv) *Existence of the detected planet*—We have assumed that the existence of the detected planet makes no difference in the detection efficiency of a stellar companion $\epsilon_{\rm LC}$ and also that the detection of the planet is robust independent of the existence of a hypothetical stellar companion. This is probably true if the binary signal is small when $s_{\rm LC} \gg 1$ or $s_{\rm LC} \ll 1$, because it is known that the triple-lens signal is well assumed by the superposition of two binary-lens signals when each signal is a small perturbation, like the one due to a planet (Han 2005). However, when $s_{\rm LC}$ is close to 1, the very large binary signal might make the planetary signal undetectable, which is inconsistent with that fact.

We decided to go with the following two options for this. One is to remove all stellar companions in $\theta_{\rm E}/3 < \phi_{\rm LC} < 3\,\theta_{\rm E}\sqrt{1 + q_{\rm LC}}$ from the full binary distribution assuming these companions make the planetary signal undetectable, where $\sqrt{1 + q_{\rm LC}}$ is to deal with the expansion of the angular Einstein radius. The other is to keep the original full binary distribution assuming that the detection of the planet is robust anyway. Note that the two binary and planet events actually detected have their stellar companions out of the range removed in the former option.

The recalculated $P_{\mathrm{det,LC_{close}}}$ values are shown in Table 7, where"–w/ (i)–(iv)" is the result of the option in factor (iv) that removes $\theta_{\mathrm{E}}/3 < \phi_{\mathrm{LC}} < 3\ \theta_{\mathrm{E}}\ \sqrt{1+q_{\mathrm{LC}}}$, while "–$w$/ (i)–(iii)" is the result of the other option that retains the full binary distribution. The $P_{\mathrm{det,LC_{close}}}$ values of "–w/ (i)–(iii)" are very similar to the previous estimates, while those of "–w/ (i)–(iv)" are very different; hence, the choice given in factor (iv) dominantly determines the detectable fractions of lens companion.

In each option, the two relatively low-magnification events (M16227 and O120950) and the other three high-magnification events (M08310, M11293, and O120563) show similar values in each of the groups, which indicate that $P_{\mathrm{det,LC_{close}}}$ highly depends on u_0, but less on other event parameters, such as θ_{E}. Thus, we apply these values to all the planetary events in our sample. Because around 40% of our sample of 49 planetary events are high-magnification events with $u_0 < 0.01$, we roughly calculate the mean value of $P_{\mathrm{det,LC_{close}}}$ in the sample as $(0.085 \times 0.6 + 0.16 \times 0.4) = 0.115$ for the case of (i)–(iv) and $(0.25 \times 0.6 + 0.30 \times 0.4) = 0.27$ for the case of (i)–(iii). The binomial distribution with trial number 49 and the success probabilities 0.115 and 0.27 yield the probability of success (i.e., the detection of binary and planet events) of less than 2 as 0.068 and 3.6×10^{-5}, respectively.

This might imply a discrepancy between the predicted and detected numbers of binary and planet events, but is not conclusive because of the variation of the p-values, which depends on the assumption of the effect of a stellar companion on the planet detectability. We discuss this result and possible implications in Section 11.4.

11. Discussion

11.1. Need to Resolve the Lens Star

We found that it is difficult to conclude whether the excess flux comes from the lens for events with small θ_{E} ($\lesssim$0.3 mas). This difficulty with inconclusive results for events with a small θ_{E} originates from the method itself, where excess flux is required to be detected at the source position that is unresolved. To be detected at the position of a source star, the excess flux has to be significantly brighter than the uncertainty of the source flux, e.g., $F_{\mathrm{ex,obs}} > 3\sigma_{F_S}$ for 3σ detection, as discussed in Section 7. This requirement imposes a lower limit on the brightness of the detectable excess flux regardless of the imaging quality, which depends only on the source flux error and is typically $\sim$20 mag in the H band for the current ground-based optical survey. For events with small $\theta_{\mathrm{E}} \lesssim 0.3$mas, the probability of the lens brightness being $H_L \sim 20$ or brighter is smaller than or comparable to the probability of a source companion being $H_{\mathrm{SC}} \sim 20$ or brighter, as shown in the bottom-right panels of the (a) components in Figures 2–4. This always leads to inconclusive interpretations for the origin of the excess fluxes detected at the position of events with small θ_{E}, even with a perfect AO correction.

One might think that color measurements of the excess flux would be useful; however, in fact, they are not useful in the case of small θ_{E} because a lens with the brightness of such a detectable excess flux ($H_L \lesssim 20$) corresponds to a star located very close to the source star. This can be seen in the shape of the mass–distance relation of small θ_{E}, i.e., the blue lines in the left panels in Figures 2–4. Thus, we cannot distinguish a case where the excess originates in the lens from a case where the excess originates in a source companion even with color measurements, because in both cases, the excess origins are located at similar distances and thus have similar colors. Meanwhile, in the case of large θ_{E}, color measurements would help distinguish between the two cases because the color of the excess should be different depending on which is true. For example, if we had a color measurement of the excess for O120950, we might have completely excluded the low possibility of a source companion although it was already proven by Bhattacharya et al. (2018) that the detected excess was certainly from the lens.

To overcome the difficulty associated with events with small θ_{E}, we need to wait several years after the event until the lens becomes resolvable from the source, where the detectable lens brightness is limited by the limiting magnitude of each imaging rather than the error of the source flux, and the probability of contamination from the source companion becomes much lower. Even when a candidate is found at a position expected from the lens–source relative proper motion μ_{rel} measured via light-curve modeling, the resolved candidate can still be a lens companion. However, such a probability is low, especially for a high-magnification event, as discussed in Section 6.5. Furthermore, whether the candidate is the lens or a lens companion is distinguishable if we have a 1D or 2D microlens parallax measurement from the light curve (Bennett et al. 2020).

Part of our results is already confirmed by such observations conducted several years after each event to resolve the lens star. Bhattacharya et al. (2017) observed M08310 using the HST and found that the lens star is not the source of the excess detected by Janczak et al. (2010). They found that the excess was likely due to a nearby unrelated star, if the excess was solely provided by one star. Our calculation also indicates a moderate probability of ambient stars as the origin of the excess, as shown in Figure 3(b). Furthermore, Bhattacharya et al. (2018) found that the origin of the excess flux at the location of O120950 was actually the lens itself. Our calculation also indicates the highest probability of this scenario, as shown in Figure 6(b).

11.2. Studying the Planet-hosting Probability by Excess Flux Measurements

Although resolving the lens star from the source star is required for robust lens detection, especially for events with small θ_{E}, excess flux measurements can still be used to statistically determine the dependence of the planet-hosting probability on the stellar mass or location in our galaxy. Because the prior distribution of the excess flux depends on the planet-hosting probability, we can find which dependence gives the maximum likelihood for the measurements by excess flux observations for many planetary events. Although the same study could be conducted using a sample of resolved lens stars, one obvious advantage of this method is that we do not need to wait for the lens to become resolvable; thus, it is easier to increase the number of samples.

In particular, the discovery rate of planetary events has been increasing since the Korean Microlensing Network (KMTNet, Kim et al. 2016) started their survey using three 1.6 m telescopes in 2015. However, it is not scientifically meaningful to wait for several years to resolve such lens stars in dozens of newly discovered planetary events because such an opportunity will come in the era of the WFIRST survey, where the discovery of $\sim$1400 planetary events and mass measurements

for most of them are expected (Penny et al. 2019). We would rather propose that excess flux measurements be conducted for the newly discovered planetary events soon after their discovery so that a statistical study of these samples can reveal the planet-hosting probability through our method.

In addition, the time needed to resolve the lens depends on the $\mu_{\rm rel}$ value and on the contrast between the source and lens stars flux. Some events with very slow $\mu_{\rm rel}$ and/or a much brighter source are not likely to be resolved even after several years. One such example is MACHO-97-BLG-28, where the lens could not be resolved even by Keck AO imaging conducted 16 yr after the event's peak (Blackman et al. 2020). A campaign of high-angular-resolution follow-up observations for the 30 planetary events in Suzuki et al. (2016), the largest statistical sample of planetary events thus far, is ongoing, and most of them have already been observed (Batista et al. 2015; Bennett et al. 2015, 2020; Bhattacharya et al. 2017, 2018; Vandorou et al. 2019). Although some lens stars can be identified in the images, there are some lens stars that cannot be resolved, to which the method developed in this paper can be applied for analysis. Because excluding such events without lens identifications causes a bias in the sample, they must also be included and correctly treated using our method in a statistical study with the results of the follow-up campaign.

11.3. Fewer Stellar Companions in a Planetary System?

In Section 10.3, we found a possible discrepancy between the fraction of detectable lens companions expected from our model and the fraction of actually detected lens stellar companions in planetary events. If this discrepancy is real, there are two possibilities for interpreting this result.

The first possibility is that the frequency of a stellar companion in a planetary system located in the galactic disk or bulge is smaller than the binary frequency of nearby randomly selected stars. Some studies have investigated the effect of the existence of stellar companions on planet frequency (Wang et al. 2014, 2015; Ngo et al. 2017; Ziegler et al. 2018); however, all of them are for planets close to their host star and not for planets beyond the snow line, such as microlensing planets. In the close region that they explored, they found clues that planet formation is suppressed by the existence of stellar companions, which might support this possibility.

The second possibility is that some detectable binary and planet events have been misclassified. In this case, there should be some detectable binary and planet events that are classified as just a binary or a planetary event owing to the omission of triple-lens model fitting. This idea is supported by Gould et al. (2014), who found the preference of the best-fit binary and planet model over the best-fit binary model to be $\Delta\chi^2 = 216$ over the peak of OGLE-2013-BLG-0341, which appears as just a binary event at first glance.

However, the level of discrepancy depends on our assumption on the region where the existence of a stellar companion makes the planet detected in each event undetectable. That is, $p = 3.6 \times 10^{-5}$ if we assume that there is no such region, and it gets a marginally acceptable p-value of $p = 0.068$ if we assume the region is $\theta_{\rm E}/3 < \phi_{\rm LC} < 3\,\theta_{\rm E}\sqrt{1+q_{\rm LC}}$ and remove it from the full binary distribution. The p-value gets larger if the range of the removal region is larger. Therefore, more careful study of the detection efficiency for an additional stellar component in a binary-lens system is needed to conclude.

11.4. Application to Other Studies

11.4.1. Constraint on the Lens Properties

The method developed in this study should be employed for all analyses that include constraints from excess flux measurements. We have already applied our method to several studies of event analysis (Koshimoto et al. 2017a; Beaulieu et al. 2018; Bennett et al. 2018b; Nagakane et al. 2019; Fukui et al. 2019; Poleski et al. 2020) to determine the lens properties or to calculate the contamination probabilities in the excess flux before this paper was published. Because the estimated lens properties by our method are quite different from previous calculations for events with small $\theta_{\rm E}$, as seen in Table 4 or Figures 2(b)–4(b), future statistical studies that use lens properties of planetary events estimated by Bayesian analysis, like the one by Cassan et al. (2012) or Penny et al. (2016), should use the properties estimated using our method for events with excess flux measurement.

The largest unbiased statistical sample of events with excess flux measurements will be provided by WFIRST, and our method can be applicable to all of them, including single-lens events. Although more than half of the lens stars can be resolved during the WFIRST survey, there is still a moderate fraction of events with slow relative proper motion where our method would give the tightest constraint.

11.4.2. Study of Binary Distribution Undetectable by Microlensing

The binary distribution in the galactic bulge is still unknown. Microlensing can reach companions located in $\log[a/{\rm au}] < 2$ while high-angular-resolution imaging can reach those in $\log[a/{\rm au}] > 3$, as seen in the undetectable binary distributions in Figure 12; hence, companions in $2 < \log[a/{\rm au}] < 3$ cannot be accessed by either of them. An interesting feature of the excess flux is that those undetectable binary companions contribute to it. Thus, we can study binary fraction in the inaccessible region in the galactic bulge by comparing our prediction of the excess flux distribution with the detected excess flux distribution in the WFIRST sample.

Moreover, the binary distributions optimized for the bulge field can be applicable for a binary correction in the study of the stellar IMF. There are many studies that have investigated the IMF in the galactic bulge, such as by the observed LF (e.g., Zoccali et al. 2000; Calamida et al. 2015) or by the observed $t_{\rm E}$ distribution in microlensing survey (Sumi et al. 2011; Mróz et al. 2017; Wegg et al. 2017). An important procedure to convert the observed luminosity or $t_{\rm E}$ distribution into the mass function is the binary correction. Most of the studies just applied a binary distribution for solar-type stars (Duquennoy & Mayor 1991; Raghavan et al. 2010). We have developed the binary distribution for an arbitrary star as a function of its mass, $f_{\rm arb}(q, a|M)$, and also for a non-secondary star, in Section 4.4. These two distributions optimized for the bulge field can be applied to the binary correction for the $t_{\rm E}$ distribution and the LF.

12. Summary

We developed a Bayesian approach for calculating the prior and posterior probability distributions of the flux for four

possible origins of the excess flux. The four possible origins are the lens, unrelated ambient stars, and companions to the source and lens. Although this probability has been considered in some previous studies, they have not always treated the prior and posterior constraints consistently, which has always led to the claim that the lens star is the likely origin of the excess flux, regardless of the extent to which the lens flux is likely to be faint a priori. Such flawed treatment has been performed to avoid the calculation of the prior probability distribution of the lens flux, which requires us to assume an unknown planet-hosting probability in the case of planetary microlensing events. However, calculating the prior probability for the lens flux is inevitable in order to correctly calculate the posterior probability of each possible origin.

Then, we assumed that the planet-hosting probability was the same for all stars in our galaxy, and we applied our method to five planetary events where the excess flux had been detected in previous studies. We found that the probability of the lens being the main origin of the observed excess is smaller than or comparable to the total probability of the other contaminants being the main origin for three events with small $\theta_{\rm E}$ ($\lesssim$0.3 mas), namely M16227, M08310, and M11293. Consequently, our lens mass estimates for M08310 and M11293 were more uncertain than the estimates of previous studies that assumed the excess flux to be the lens flux (Janczak et al. 2010; Batista et al. 2014). Meanwhile, for O120563, which has a large angular Einstein radius of $\theta_{\rm E} = 1.4$ mas, a large part of the excess flux is highly likely to be from the lens itself. This is also the case for O120950, which has a long Einstein-radius-crossing time of $t_{\rm E} = 68$ days, which indicates that $\theta_{\rm E}$ is likely to be large. Thus, our lens mass estimates for these two events are consistent with previous studies that treated a large part of the excess flux as the lens flux (Fukui et al. 2015; Koshimoto et al. 2017b). This qualitative interpretation for the origin of each excess flux does not change even if we apply a different prior for the dependence of the planet-hosting probability on the host mass. We recommend using our estimates of the lens properties for M11293 and O120563, whereas one should use the properties for M08310 and O120950 estimated by Bhattacharya et al. (2017, 2018), respectively.

To robustly detect the lens star, especially for events with small $\theta_{\rm E}$, we need to resolve the lens star from the source star through additional high-angular-resolution imaging conducted when the two systems become resolvable. Our interpretations of the excess fluxes for M08310 and O120950 were already confirmed by such observations (Bhattacharya et al. 2017, 2018). However, such observations typically require a waiting time of several years after the event discovery. Although the KMTNet survey (Kim et al. 2016) has significantly increased the discovery rate of planetary events, this requirement makes it unlikely that lens stars in dozens of newly discovered events will be resolved by the time of the WFIRST survey. The method developed in this study can be used to statistically study the dependence of the planet-hosting probability on the host's properties using only excess flux measurements for planetary events. Because there is no requirement with regard to the observation time for excess flux measurements, all newly discovered events can be added to the sample by conducting high-angular-resolution follow-up imaging. This would provide us with the largest sample of planetary events to study the dependence of the planet-hosting probability on the host's properties before the WFIRST era.

Our method can be applied to estimate the lens property of all the WFIRST events, although more than half of them should be updated after the lens star is resolved. Also, we can study the binary fraction in the galactic bulge located in $2 < \log[a/{\rm au}] < 3$, a region inaccessible by other methods, by comparing the predicted excess flux distributions to the one observed in the WFIRST sample.

We are grateful to J. P. Beaulieu and Y. Shvartzvald, who provided us with the data of the Keck images taken in their observations. We are also grateful to H. Shibai, T. Sumi, and C. Ranc for fruitful discussions. We would like to thank Editage (www.editage.com) for English language editing. The work of N.K. is supported by JSPS KAKENHI grant No. JP18J00897. D.P.B. was supported by NASA through grant NASA-80NSSC18K0274.

Appendix
How to Calculate the Detection Efficiency for a Stellar Companion

In Section 10.3.1, we calculated the detection efficiency $\epsilon_{\rm LC}$ for a planetary companion to a stellar companion around the lens in M16227 and O120950, as shown in Figure 16 (we used only the result for $q_{\rm LC} > 0.1$ in this study). In this section, we focus on the difference between the ways to calculate the detection efficiency for a planetary companion and a stellar companion. This difference mainly arises from the expansion of the angular Einstein radius by considering a stellar companion, which does not matter for a planetary companion. Readers may refer to the work of Suzuki et al. (2016) and the references therein for details on the method to calculate the detection efficiency for a planetary companion.

For simplicity, we ignore the existence of the detected planet and consider a situation where we observed a single-lens event with $t_{\rm E,1L}$, $u_{0,1\rm L}$, $\rho_{1\rm L}$, and $\theta_{\rm E,1L}$, where ρ is the angular source star radius in units of the angular Einstein radius, $\rho \equiv \theta_*/\theta_{\rm E}$. In this situation, we consider the detection efficiency for a lens companion with a mass ratio $q_{\rm LC}$ located at an angular separation of $s_{\rm LC}\,\theta_{\rm E,1L}$ in the lens system. Note that $s_{\rm LC}$ is the separation defined in units of $\theta_{\rm E,1L}$.

When considering the detection efficiency for a stellar companion with mass ratio $q_{\rm LC}$ that is not negligible compared to 1, an expansion of the angular Einstein radius by a factor of $\sqrt{q_{\rm LC}+1}$ has to be considered. This is because most quantities observable by microlensing are defined in units of the angular Einstein radius. In this situation, we consider the parameters that we should use for artificial light curves to simulate hypothetical observations. Although it seems to be complicated to consider this effect when the separation $s_{\rm LC} \sim 1$, easy approximations are applicable for $s_{\rm LC} \gg 1$ and $s_{\rm LC} \ll 1$.

As shown in the left panel of Figure A1, two separated central caustics are created by a wide binary system with the separation $s_{\rm LC} \gg 1$ and a stellar mass ratio $q_{\rm LC} \gtrsim 1$, and the magnification map is separated into two nearly distinct areas. Although the angular Einstein radius for the entire lens system is $\theta_{\rm E}$, each of the separated areas behaves as if it is created by a single lens with the angular Einstein radius $\theta_{\rm E}/\sqrt{q_{\rm LC}+1}$ (the left area) or $\theta_{\rm E}\sqrt{q_{\rm LC}/(q_{\rm LC}+1)}$ (the right area) centered at each of the caustics. In the situation considered where we observed only a magnification caused by the left area in the left panel and identified it as a single lens with $\theta_{\rm E,1L}$ (but actually, $\theta_{\rm E,1L} = \theta_{\rm E}/\sqrt{q_{\rm LC}+1}$), we have to calculate the detection

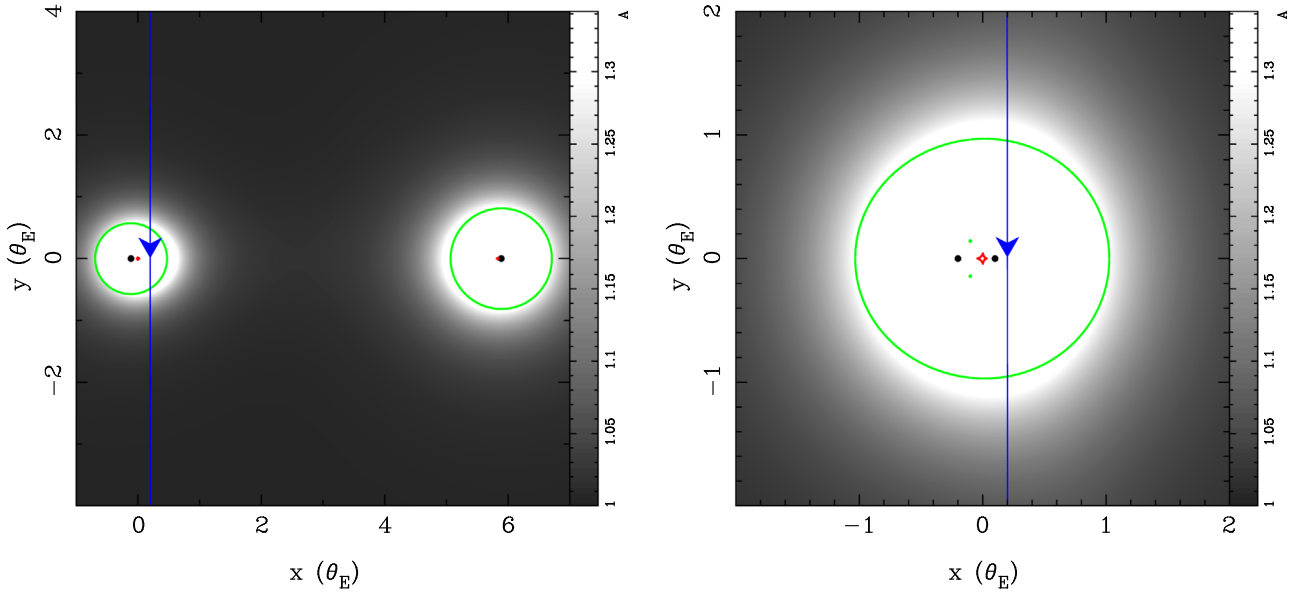

Figure A1. Two examples of the geometry with an undetected companion. Left: magnification map for a binary lens with mass ratio $q = 2$ and separation $s = 6$. The two black dots indicate the lens objects, the small red structures indicate caustics, and the green closed curves indicate critical curves. The regions in pure white indicate the area with magnification $A > 1.34$, which corresponds to the region of $u < 1$ in a single-lens event. An observer who observes the magnification curve of the source star passing the blue arrow misestimates the microlens parameters as $\theta_{\rm E,1L} = \theta_{\rm E}/\sqrt{1+q} = \theta_{\rm E}/\sqrt{3}$, $t_{\rm E,1L} = t_{\rm E}/\sqrt{3}$, $u_{0,0} = \sqrt{3}\,u_0$, and $\rho_0 = \sqrt{3}\,\rho$. Furthermore, in the lens plane with the unit of the observed $\theta_{\rm E,1L}$, the separation of this undetected companion becomes $s_{\rm LC} = \sqrt{3}\,s = 6\sqrt{3}$. Right: magnification map for a binary lens with mass ratio $q = 0.5$ and separation $s = 0.3$. An observer who observes the magnification curve of the source star passing the blue arrow correctly estimates $\theta_{\rm E,1L} = \theta_{\rm E}$, $t_{\rm E,1L} = t_{\rm E}$, $u_{0,0} = u_0$, and $\rho_0 = \rho$, but does not notice that the lens actually consists of two stars. In this case, the separation in units of $\theta_{\rm E,1L}$ is $s_{\rm LC} = s$.

efficiency of a stellar companion by making artificial light curves with $t_{\rm E} = \sqrt{q_{\rm LC}+1}\,t_{\rm E,1L}$, $u_0 = u_{0,1L}/\sqrt{q_{\rm LC}+1}$, $\rho = \rho_{1L}/\sqrt{q_{\rm LC}+1}$, $q = q_{\rm LC}$, and $s = s_{\rm LC}/\sqrt{q_{\rm LC}+1}$ to reproduce the observed apparent single-lens event. Thus, the detection efficiency $\epsilon_{\rm LC}$ at a grid ($q_{\rm LC}$, $s_{\rm LC}$) with $s_{\rm LC} \gg 1$ in Figure 16 is actually calculated by putting in a stellar companion with $q = q_{\rm LC}$ and $s = s_{\rm LC}/\sqrt{q_{\rm LC}+1}$ to deal with the expansion of the angular Einstein radius.

Meanwhile, as shown in the right panel of Figure A1, the magnification map around the central caustic that is created by a close binary system with the separation $s_{\rm LC} \ll 1$ and mass ratio $q_{\rm LC} \gtrsim 1$ behaves like a single-lens event centered at the central caustic except for the region close to the caustic. In this case, the components of the binary system contributed to the observed magnification that appears as a single-lens light curve with $\theta_{\rm E,1L}$. Therefore, in contrast to the case for $s_{\rm LC} \gg 1$, the angular Einstein radius is not expanded compared to the observed size, i.e., $\theta_{\rm E} = \theta_{\rm E,1L}$. In other words, we should make the artificial light curves with $t_{\rm E} = t_{\rm E,1L}$, $u_0 = u_{0,1L}$, $\rho = \rho_{1L}$, and $s = s_{\rm LC}$ to calculate detection efficiencies. For the mass ratio q, we should use $q = q_{\rm LC}$ for $q_{\rm LC} \leqslant 1$ and $q = 1/q_{\rm LC}$ for $q_{\rm LC} > 1$. This is because we cannot distinguish the light curve with $q_{\rm LC}$ from that with $1/q_{\rm LC}$, in contrast to the case of $s_{\rm LC} \gg 1$. Therefore, the gray line in Figure 16 has a turnoff point while the black line does not.

The events analyzed in this study have high sensitivity to a stellar companion because all of them have moderate coverage on their light curves with $u_0 \lesssim 0.1$. Therefore, separation values that correspond to the borders between $\epsilon_{\rm LC} = 1$ and $\epsilon_{\rm LC} < 1$ with a given $q_{\rm LC}$ (>0.1) should be located in a region satisfying the condition of $s_{\rm LC} \gg 1$ or $s_{\rm LC} \ll 1$, where the approximations mentioned above can be applied. If this is true, the detection efficiency is expected to be $\epsilon_{\rm LC} = 1$ in the medium region of $s_{\rm LC} \sim 1$, regardless of how the detection efficiency for $s_{\rm LC} \sim 1$ and $q_{\rm LC} \gtrsim 1$ is calculated. We use the parameters of $s_{\rm LC} \gg 1$ for all companions with $s_{\rm LC} > 1$ while we use the parameters of $s_{\rm LC} \ll 1$ for all companions with $s_{\rm LC} \leqslant 1$ to create artificial light curves in the detection efficiency calculation. Figure 16 shows the calculation results. In both events, we find that the separation values that correspond to borders between $\epsilon_{\rm LC} = 1$ and $\epsilon_{\rm LC} < 1$ with $q_{\rm LC} > 0.1$ are sufficiently large or small to be applied to the approximation of $s_{\rm LC} \gg 1$ or $s_{\rm LC} \ll 1$, respectively. Thus, the color maps shown in Figure 16 are correct if the detection efficiency $\epsilon_{\rm LC}$ always increases when s approaches 1.

ORCID iDs

Naoki Koshimoto https://orcid.org/0000-0003-2302-9562
David P. Bennett https://orcid.org/0000-0001-8043-8413
Daisuke Suzuki https://orcid.org/0000-0002-5843-9433

References

Adams, A. D., Boyajian, T. S., & von Braun, K. 2018, MNRAS, 473, 3608
Alcock, C., Allsman, R. A., Alves, D., et al. 1995, ApJL, 454, L125
Alcock, C., Allsman, R. A., Alves, D., et al. 1997, ApJ, 479, 119
Allen, P. R. 2007, ApJ, 668, 492
An, J. H., Albrow, M. D., Beaulieu, J.-P., et al. 2002, ApJ, 572, 521
Bahcall, J. N. 1986, ARA&A, 24, 577
Baraffe, I., Chabrier, G., Barman, T. S., Allard, F., & Hauschildt, P. H. 2003, A&A, 402, 701
Batista, V., Beaulieu, J.-P., Bennett, D. P., et al. 2015, ApJ, 808, 170
Batista, V., Beaulieu, J.-P., Gould, A., et al. 2014, ApJ, 780, 54
Beaulieu, J.-P., Batista, V., Bennett, D. P., et al. 2018, AJ, 155, 78
Beaulieu, J.-P., Bennett, D. P., Fouqué, P., et al. 2006, Natur, 439, 437
Behrens, E. A., Ransom, S. M., Madison, D. R., et al. 2020, ApJL, 893, L8
Bennett, D. P., Alcock, C. A., Allsman, R. A., et al. 1997, in ASP Conf. Proc. 119, Planets Beyond the Solar System and the Next Generation of Space Missions, ed. D. R. Soderblom (San Francisco, CA: ASP), 95
Bennett, D. P., Anderson, J., Bond, I. A., Udalski, A., & Gould, A. 2006, ApJL, 647, L171

Bennett, D. P., Anderson, J., & Gaudi, B. S. 2007, ApJ, 660, 781
Bennett, D. P., Batista, V., Bond, I. A., et al. 2014, ApJ, 785, 155
Bennett, D. P., Bhattacharya, A., Anderson, J., et al. 2015, ApJ, 808, 169
Bennett, D. P., Bhattacharya, A., Beaulieu, J.-P., et al. 2020, AJ, 159, 68
Bennett, D. P., & Rhie, S. H. 1996, ApJ, 472, 660
Bennett, D. P., & Rhie, S. H. 2002, ApJ, 574, 985
Bennett, D. P., Rhie, S. H., Udalski, A., et al. 2016, AJ, 152, 125
Bennett, D. P., Udalski, A., Bond, I. A., et al. 2018a, AJ, 156, 113
Bennett, D. P., Udalski, A., Han, C., et al. 2018b, AJ, 155, 141
Bhattacharya, A., Beaulieu, J.-P., Bennett, D. P., et al. 2018, AJ, 156, 289
Bhattacharya, A., Bennett, D. P., Anderson, J., et al. 2017, AJ, 154, 59
Blackman, J. W., Beaulieu, J.-P., Cole, A. A., et al. 2020, ApJ, 890, 87
Boyajian, T. S., van Belle, G., & von Braun, K. 2014, AJ, 147, 47
Bressan, A., Marigo, P., Girardi, L., et al. 2012, MNRAS, 427, 127
Calamida, A., Sahu, K. C., Casertano, S., et al. 2015, ApJ, 810, 8
Cardelli, J. A., Clayton, G. C., & Mathis, J. S. 1989, ApJ, 345, 245
Cassan, A., Kubas, D., Beaulieu, J.-P., et al. 2012, Natur, 481, 167
Chen, Y., Bressan, A., Girardi, L., et al. 2015, MNRAS, 452, 1068
Chen, Y., Girardi, L., Bressan, A., et al. 2014, MNRAS, 444, 2525
Chung, S.-J., Han, C., Park, B.-G., et al. 2005, ApJ, 630, 535
Delfosse, X., Forveille, T., Ségransan, D., et al. 2000, A&A, 364, 217
Duchêne, G., & Kraus, A. 2013, ARA&A, 51, 269
Duquennoy, A., & Mayor, M. 1991, A&A, 248, 485
Dwek, E., Arendt, R. G., Hauser, M. G., et al. 1995, ApJ, 445, 716
Fukui, A., Gould, A., Sumi, T., et al. 2015, ApJ, 809, 74
Fukui, A., Suzuki, D., Koshimoto, N., et al. 2019, AJ, 158, 206
Furusawa, K., Udalski, A., Sumi, T., et al. 2013, ApJ, 779, 91
Gaudi, B. S. 2012, ARA&A, 50, 411
Ghezzi, L., Montet, B. T., & Johnson, J. A. 2018, ApJ, 860, 109
Gould, A. 1992, ApJ, 392, 442
Gould, A., Bennett, D. P., & Alves, D. R. 2004, ApJ, 614, 404
Gould, A., & Loeb, A. 1992, ApJ, 396, 104
Gould, A., Udalski, A., Shin, I.-G., et al. 2014, Sci, 345, 46
Han, C. 2005, ApJ, 629, 1102
Han, C., & Gould, A. 1995, ApJ, 447, 53
Henry, T. J., & McCarthy, D. W., Jr. 1993, AJ, 106, 773
Janczak, J., Fukui, A., Dong, S., et al. 2010, ApJ, 711, 731
Johnson, J. A., Aller, K. M., Howard, A. W., & Crepp, J. R. 2010, PASP, 122, 905
Kervella, P., Thévenin, F., di Folco, E., & Ségransan, D. 2004, A&A, 426, 297
Kim, S.-L., Lee, C.-U., Park, B.-G., et al. 2016, JKAS, 49, 37
Koester, D., Gänsicke, B. T., & Farihi, J. 2014, A&A, 566, A34
Koshimoto, N., & Bennett, D. 2019, arXiv:1905.05794
Koshimoto, N., Shvartzvald, Y., Bennett, D. P., et al. 2017a, AJ, 154, 3
Koshimoto, N., Udalski, A., Beaulieu, J. P., et al. 2017b, AJ, 153, 1
Koshimoto, N., Udalski, A., Sumi, T., et al. 2014, ApJ, 788, 128
Kroupa, P. 1995, MNRAS, 277, 1491
Kroupa, P. 2001, MNRAS, 322, 231
Kubas, D., Beaulieu, J. P., Bennett, D. P., et al. 2012, A&A, 540, A78
Marks, M., & Kroupa, P. 2011, MNRAS, 417, 1702
Montet, B. T., Crepp, J. R., Johnson, J. A., Howard, A. W., & Marcy, G. W. 2014, ApJ, 781, 28
Mróz, P., Udalski, A., Skowron, J., et al. 2017, Natur, 548, 183
Mulders, G. D., Pascucci, I., & Apai, D. 2015, ApJ, 798, 112
Muraki, Y., Han, C., Bennett, D. P., et al. 2011, ApJ, 741, 22
Nagakane, M., Lee, C.-H., Koshimoto, N., et al. 2019, AJ, 158, 212
Nataf, D. M., Gonzalez, O. A., Casagrande, L., et al. 2016, MNRAS, 456, 2692
Nataf, D. M., Gould, A., Fouqué, P., et al. 2013, ApJ, 769, 88
Ngo, H., Knutson, H. A., Bryan, M. L., et al. 2017, AJ, 153, 242
Nishiyama, S., Tamura, M., Hatano, H., et al. 2009, ApJ, 696, 1407
Penny, M. T., Gaudi, B. S., Kerins, E., et al. 2019, ApJS, 241, 3
Penny, M. T., Henderson, C. B., & Clanton, C. 2016, ApJ, 830, 150
Poindexter, S., Afonso, C., Bennett, D. P., et al. 2005, ApJ, 633, 914
Poleski, R., Skowron, J., Udalski, A., et al. 2014, ApJ, 795, 42
Poleski, R., Suzuki, D., Udalski, A., et al. 2020, AJ, 159, 261
Portail, M., Gerhard, O., Wegg, C., & Ness, M. 2017, MNRAS, 465, 1621
Raghavan, D., McAlister, H. A., Henry, T. J., et al. 2010, ApJS, 190, 1
Robin, A. C., Reylé, C., Derrière, S., & Picaud, S. 2003, A&A, 409, 523
Shvartzvald, Y., Maoz, D., Udalski, A., et al. 2016, MNRAS, 457, 4089
Skowron, J., Wyrzykowski, Ł., Mao, S., et al. 2009, MNRAS, 393, 999
Spergel, D., Gehrels, N., Baltay, C., et al. 2015, arXiv:1503.03757
Sumi, T., Bennett, D. P., Bond, I. A., et al. 2010, ApJ, 710, 1641
Sumi, T., Kamiya, K., Bennett, D. P., et al. 2011, Natur, 473, 349
Suzuki, D., Bennett, D. P., Sumi, T., et al. 2016, ApJ, 833, 145
Szymański, M. K., Udalski, A., Soszyński, I., et al. 2011, AcA, 61, 83
Tang, J., Bressan, A., Rosenfield, P., et al. 2014, MNRAS, 445, 4287
Vandorou, A., Bennett, D. P., Beaulieu, J.-P., et al. 2019, arXiv:1909.04444
Wang, J., Fischer, D. A., Horch, E. P., & Xie, J.-W. 2015, ApJ, 806, 248
Wang, J., Fischer, D. A., Xie, J.-W., & Ciardi, D. R. 2014, ApJ, 791, 111
Ward-Duong, K., Patience, J., de Rosa, R. J., et al. 2015, MNRAS, 449, 2618
Wegg, C., Gerhard, O., & Portail, M. 2017, ApJL, 843, L5
Yee, J. C., Han, C., Gould, A., et al. 2014, ApJ, 790, 14
Yee, J. C., Shvartzvald, Y., Gal-Yam, A., et al. 2012, ApJ, 755, 102
Zhu, W., Udalski, A., Calchi Novati, S., et al. 2017, AJ, 154, 210
Ziegler, C., Law, N. M., Baranec, C., et al. 2018, AJ, 156, 83
Zoccali, M., Cassisi, S., Frogel, J. A., et al. 2000, ApJ, 530, 418
Zoccali, M., Renzini, A., Ortolani, S., et al. 2003, A&A, 399, 931
Zuckerman, B., Koester, D., Reid, I. N., et al. 2003, ApJ, 596, 477